Electronic Supplementary Material (ESI) for Chemical Science.
This journal is © The Royal Society of Chemistry 2021

Supporting Information

The central role of the metal ion in photocatalysis: Zn- vs. Ni-Mabiq

Raphael Lauenstein,[a] Sophie Mader,[b] Henrieta Derondeau,[c] Oaikhena Z. Esezobor,[a] Matthias Block,[c] Armin Römer,[b] Christian Jandl,[a] Eberhard Riedle,[c] Ville R. I. Kaila,[b,†] Jürgen Hauer,[a,d] Erling Thyrhaug,*[,a] and Corinna R. Hess*[,a]

[a] Department of Chemistry and Catalysis Research Center, Technical University of Munich, Lichtenbergstr. 4, 85747 Garching, Germany
[b] Department of Chemistry, Technical University of Munich, Lichtenbergstr. 4, 85747 Garching, Germany
[c] Lehrstuhl für BioMolekulare Optik, Fakultät für Physik, Ludwig-Maximilians-Universität München, Oettingenstr. 67, 80538 Munich, Germany
[d] Photonics Institute, TU Wien, 1040 Vienna, Austria

Email: erling.thyrhaug@tum.de; corinna.hess@ch.tum.de

Contents

For the convenience of the reader we have supplied a system of topic-ordered bookmarks. Click on the bookmark icon and then readily navigate by the main topic and then by the particular Figure or subject you want to look at.

General considerations

Materials

Chemicals were purchased from Sigma Aldrich and used as received, unless otherwise noted. All sample preparations and measurements were carried out using dry deoxygenated solvents. Photoreduction, transient absorption and fluorescence experiments were carried out under Argon atmosphere. Metal complexes were prepared inside a glove box (MBraun) or using standard Schlenk techniques. Solvents were dried via a Solvent Purification System (MBraun), deoxygenated, and stored over activated molecular sieves (3 Å: acetonitrile (MeCN), n-pentane; 4 Å: dichloromethane (DCM), tetrohydrofuran (THF)). HMabiq was prepared as previously described.[1]

Physical measurements

Solution state NMR spectra were measured using a Bruker Avance Ultrashield (^{1}H, 400 MHz) or Bruker Avance DRX400 (^{19}F, 400 MHz) spectrometer. Electronic absorption spectra (UV-vis) were recorded on an Agilent Cary 60 UV-vis spectrophotometer. Absorption spectra in the near IR (NIR) region were measured with a Shimadzu UV-3600 Plus spectrophotometer. Fluorescence spectra were recorded on a Varian Cary Eclipse Fluorescence Spectrophotometer. For Electrospray ionization mass spectra (ESI-MS) a LCQ fleet spectrometer (MeCN; flow rate 0.35 ml/min; UV-detector at 220 and 280 nm) was used. Gas chromatographical analyses were carried out on an Agilent GC 7890B with a single quadrupole mass detector MS 5977A. The installed column is a VF-200 ms with a length of 30 m, an internal diameter of 0.25 mm and a film of 0.25 µm.

Reaction quantum yields were measured by a largely improved quantum yield determination setup (QYDS) based on Megerle et al.,[2] as described in some detail in Volfova et al.,[3] and on pages S19-22.

Electrochemical measurements were carried out using an EmStat3+ potentiostat. Glassy carbon electrodes were used as working and counter electrodes, Ag/AgNO$_3$ as the reference electrode. Potentials were referenced to an internal standard of Ferrocenium/Ferrocene (Fc$^{+/0}$). Ferrocene was sublimated prior to use, and tetrabutylammonium hexafluorophosphate was recrystallized three times from ethanol.

Synthesis of [Zn^{II}(Mabiq)OTf] (2)

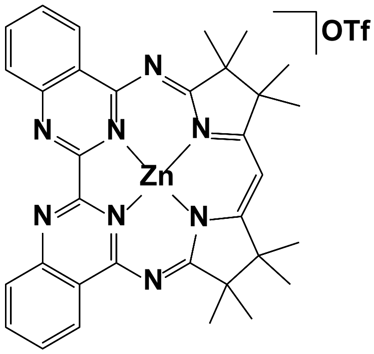

Zn(OTf)$_2$ (67.2 mg, 0.18 mmol) was added to a stirred solution of 100.0 mg (0.18 mmol) HMabiq and 25.5 µL (0.18 mmol) of NEt$_3$ in 10 mL THF, under red light conditions. The reaction vial was covered with aluminum foil to protect the mixture from light. The reaction was stirred for 16 h, upon which the color turned from yellow to pale orange. The resultant yellow precipitate was filtered and washed with THF under red light conditions. The orange filtrate was concentrated under vacuum and a second crop of yellow solid was obtained (total yield of crude product was 121 mg, 80%). Orange crystals of **2** were obtained by slow diffusion of pentane into a solution of the crude solid in DCM. The molecular structure includes one dichloromethane molecule per unit cell.

Anal. Calcd. for $C_{35}H_{35}Cl_2F_3N_8O_3SZn$ (**2**·CH_2Cl_2): C, 49.98; H, 4.19; N, 13.32; S, 3.81. Found: C, 49.88; H, 4.17; N, 13.21; S, 3.71. ESI-MS(+): *m/z* 606 ([M]$^+$).
UV-vis [λ_{max} nm (ε, x 10^3 M^{-1} cm^{-1}), DCM]: 337 (32.0), 366 (37.2), 489 (31.8).
^{1}H NMR (400 MHz, CDCl$_3$): δ 9.09 (d, *J* = 9.1 Hz, 2H), 8.48 (d, *J* = 8.5 Hz, 2H), 8.08 (dd, *J* = 8.1 Hz, 2H), 7.83 (dd, *J* = 7.8 Hz, 2H), 5.94 (s, 1H), 1.44 (s, 12H), 1.38 (s, 12H).

Crystallography, compound 2 (CCDC 1949717)

General crystallographic details

Data were collected on a single crystal x-ray diffractometer equipped with a CMOS detector (Bruker APEX III, κ-CMOS), a TXS rotating anode with MoKα radiation (λ = 0.71073 Å) and a Helios optic using the APEX3 software package.[4] Measurements were performed on single crystals coated with perfluorinated ether. The crystals were fixed on top of a kapton micro sampler and frozen under a stream of cold nitrogen. A matrix scan was used to determine the initial lattice parameters. Reflections were corrected for Lorentz and polarisation effects, scan speed, and background using SAINT.[5] Absorption correction, including odd and even ordered spherical harmonics was performed using SADABS.[6] Space group assignment was based upon systematic absences, E statistics, and successful refinement of the structure. The structures were solved using SHELXT with the aid of successive difference Fourier maps, and were refined against all data using SHELXL in conjunction with SHELXLE.[7-9] Hydrogen atoms were calculated in ideal positions as follows: Methyl hydrogen atoms were refined as part of rigid rotating groups, with a C–H distance of 0.98 Å and $U_{iso}(H) = 1.5 \cdot U_{eq}(C)$. Other H atoms were placed in calculated positions and refined using a riding model, with methylene and aromatic C–H distances of 0.99 Å and 0.95 Å, respectively, and other C–H distances of 1.00 Å, all with $U_{iso}(H) = 1.2 \cdot U_{eq}(C)$. Non-hydrogen atoms were refined with anisotropic displacement parameters. Full-matrix least-squares refinements were carried out by minimizing $\Sigma w(F_o^2 - F_c^2)^2$ with the SHELXL weighting scheme.[7] Neutral atom scattering factors for all atoms and anomalous dispersion corrections for the non-hydrogen atoms were taken from International Tables for Crystallography.[10] A split layer refinement was used for a disordered CF_3 group and additional SIMU, DELU and SAME restraints were employed. Images of the crystal structures were generated with PLATON and Mercury.[11, 12] CCDC 1949717 contains the supplementary crystallographic data for this paper. These data are provided free of charge by The Cambridge Crystallographic Data Centre.

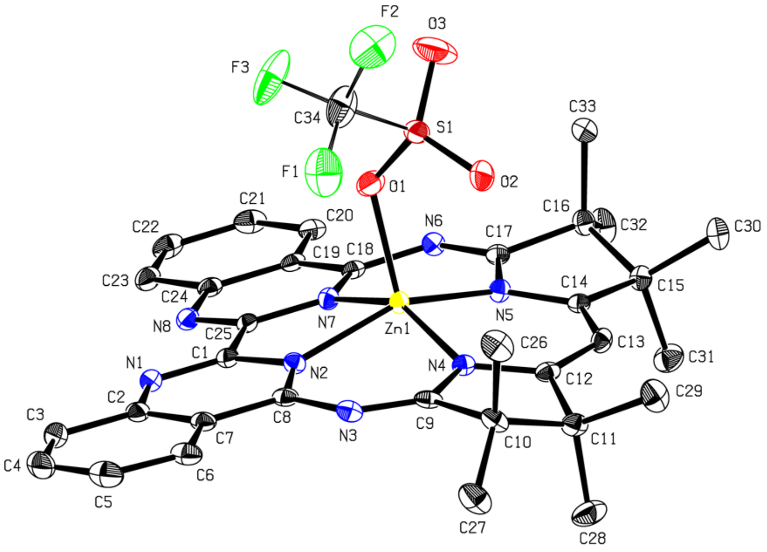

Diffractometer operator C. Jandl
scanspeed 1-2 s per frame
dx 40 mm
1918 frames measured in 10 data sets
phi-scans with delta_phi = 0.5
omega-scans with delta_omega = 0.5
shutterless mode

Crystal data

$C_{34}H_{33}F_3N_8O_3SZn\cdot CH_2Cl_2$	
M_r = 841.06	D_x = 1.536 Mg m^{-3}
Monoclinic, $P2_1/n$	Melting point: ? K
Hall symbol: -P 2yn	Mo $K\alpha$ radiation, λ = 0.71073 Å
a = 13.2525 (9) Å	Cell parameters from 9724 reflections
b = 18.3533 (12) Å	θ = 2.2–26.4°
c = 15.0527 (9) Å	μ = 0.94 mm^{-1}
β = 96.635 (2)°	T = 100 K
V = 3636.7 (4) Å^3	Fragment, orange
Z = 4	0.35 × 0.33 × 0.27 mm
F(000) = 1728	

Data collection

Bruker Photon CMOS diffractometer	7163 independent reflections

Radiation source: TXS rotating anode	6196 reflections with $I > 2\sigma(I)$
Helios optic monochromator	$R_{\text{int}} = 0.056$
Detector resolution: 16 pixels mm^{-1}	$\theta_{\text{max}} = 26.0°$, $\theta_{\text{min}} = 2.2°$
phi– and ω–rotation scans	$h = -16\quad 16$
Absorption correction: multi-scan *SADABS* 2014/5, Bruker	$k = -22\quad 22$
$T_{\text{min}} = 0.680$, $T_{\text{max}} = 0.745$	$l = -18\quad 18$
104552 measured reflections	

Refinement

Refinement on F^2	Secondary atom site location: differenc Fourier map
Least-squares matrix: full	Hydrogen site location: inferred from neighbouring sites
$R[F^2 > 2\sigma(F^2)] = 0.031$	H-atom parameters constrained
$wR(F^2) = 0.074$	$W = 1/[\Sigma^2(FO^2) + (0.0294P)^2 + 4.3229P$ WHERE $P = (FO^2 + 2FC^2)/3$
$S = 1.03$	$(\Delta/\sigma)_{\text{max}} = 0.002$
7163 reflections	$\Delta\rho_{\text{max}} = 0.82$ e Å^{-3}
523 parameters	$\Delta\rho_{\text{min}} = -0.61$ e Å^{-3}
126 restraints	Extinction correction: none
0 constraints	Extinction coefficient: -
Primary atom site location: intrinsic phasing	

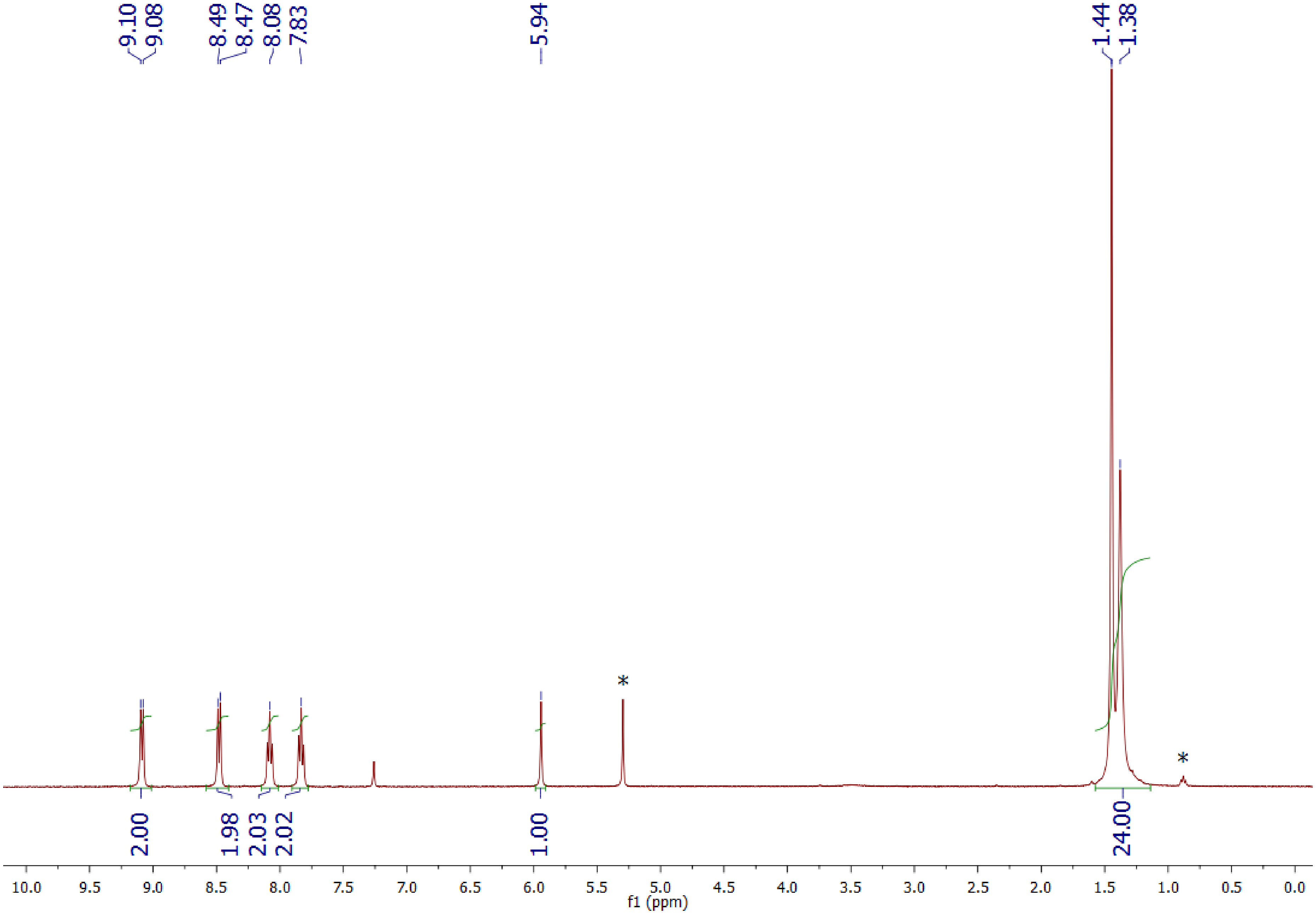

Figure S1. ^{1}H-NMR of **2** in $CDCl_3$. Residual solvent signals (*n*-pentane and DCM) are marked with asterisks.

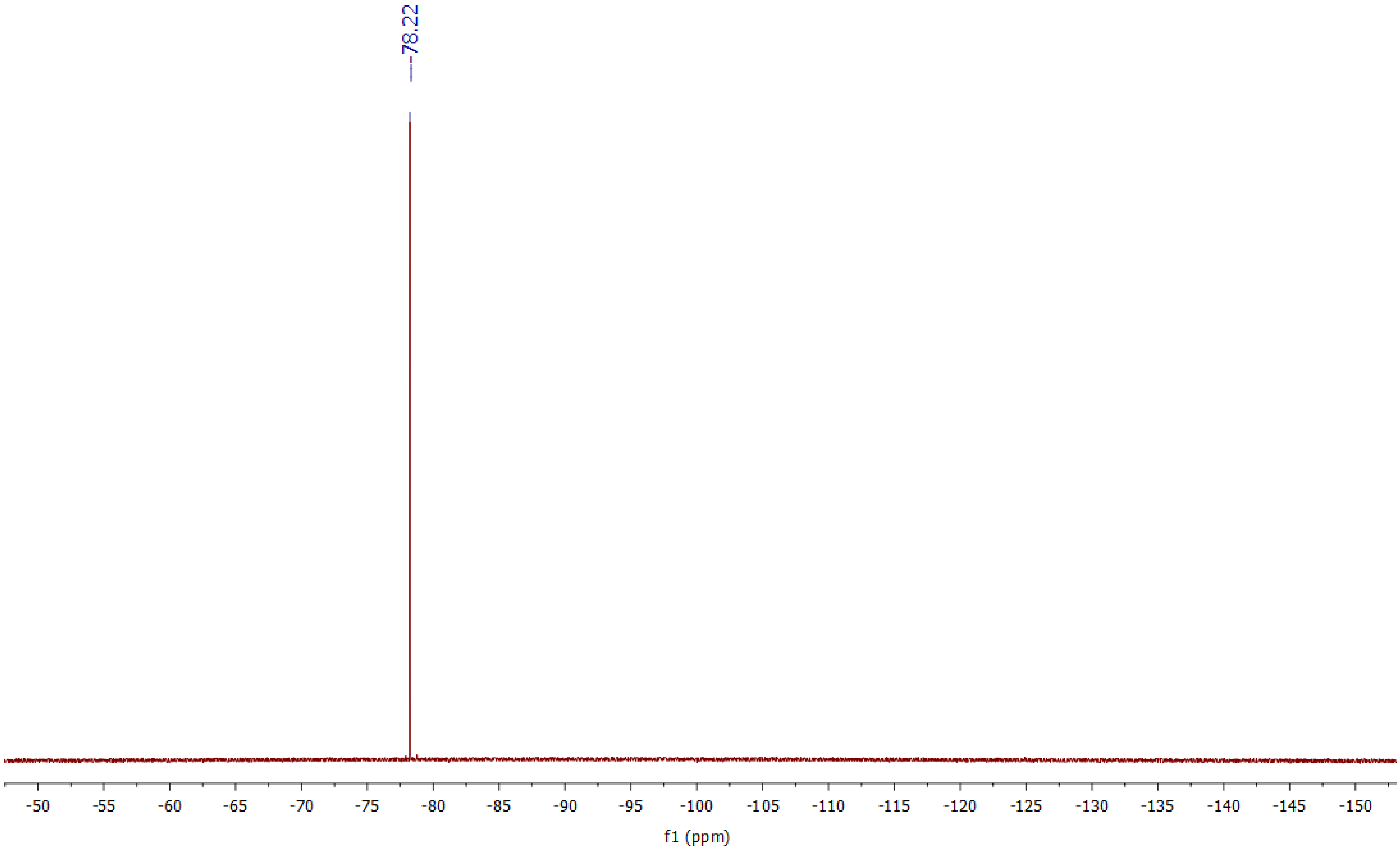

Figure S2. ^{19}F-NMR spectrum of **2** in CDCl$_3$.

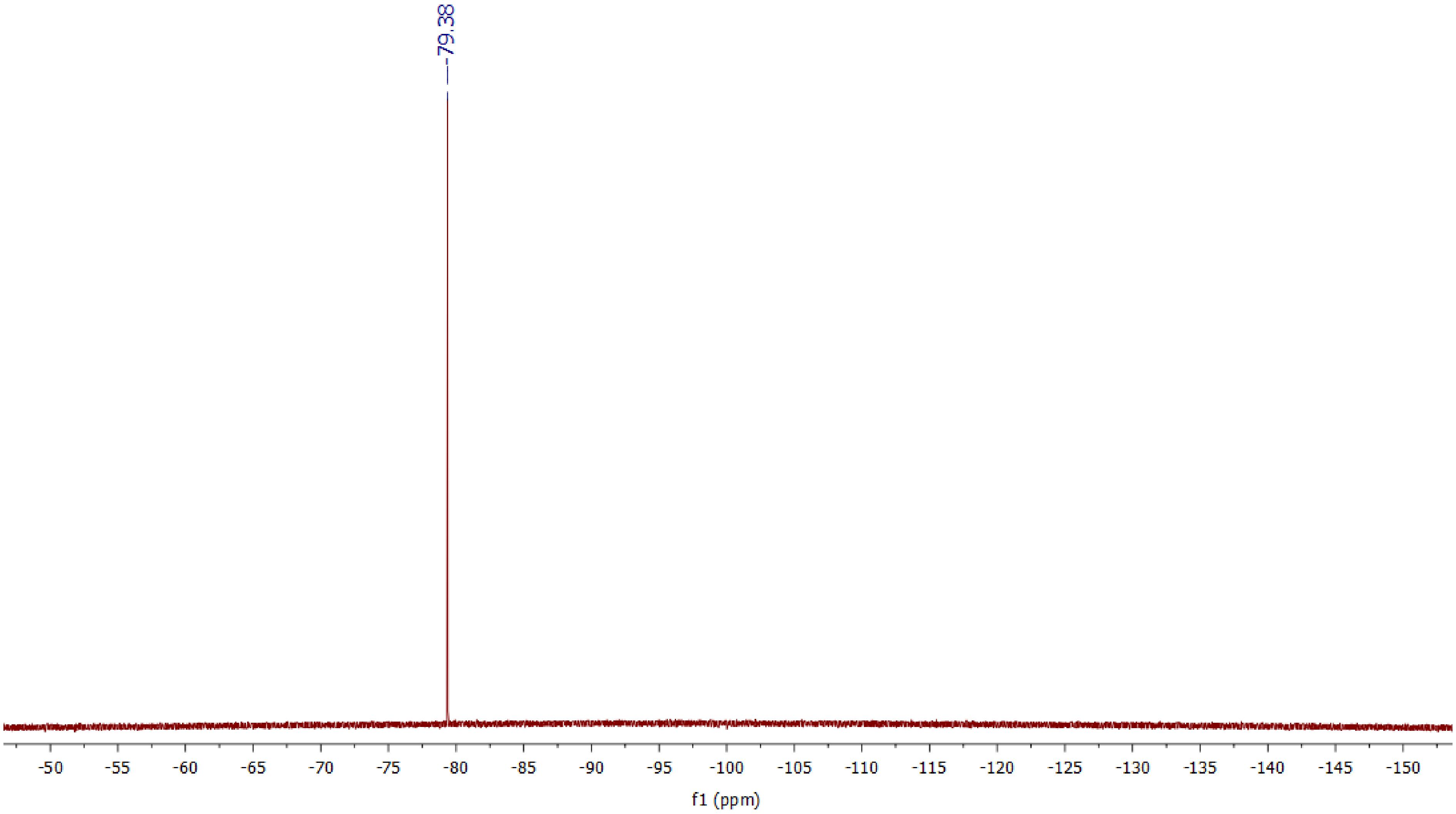

Figure S3. ^{19}F-NMR spectrum of **2** in CD_3CN.

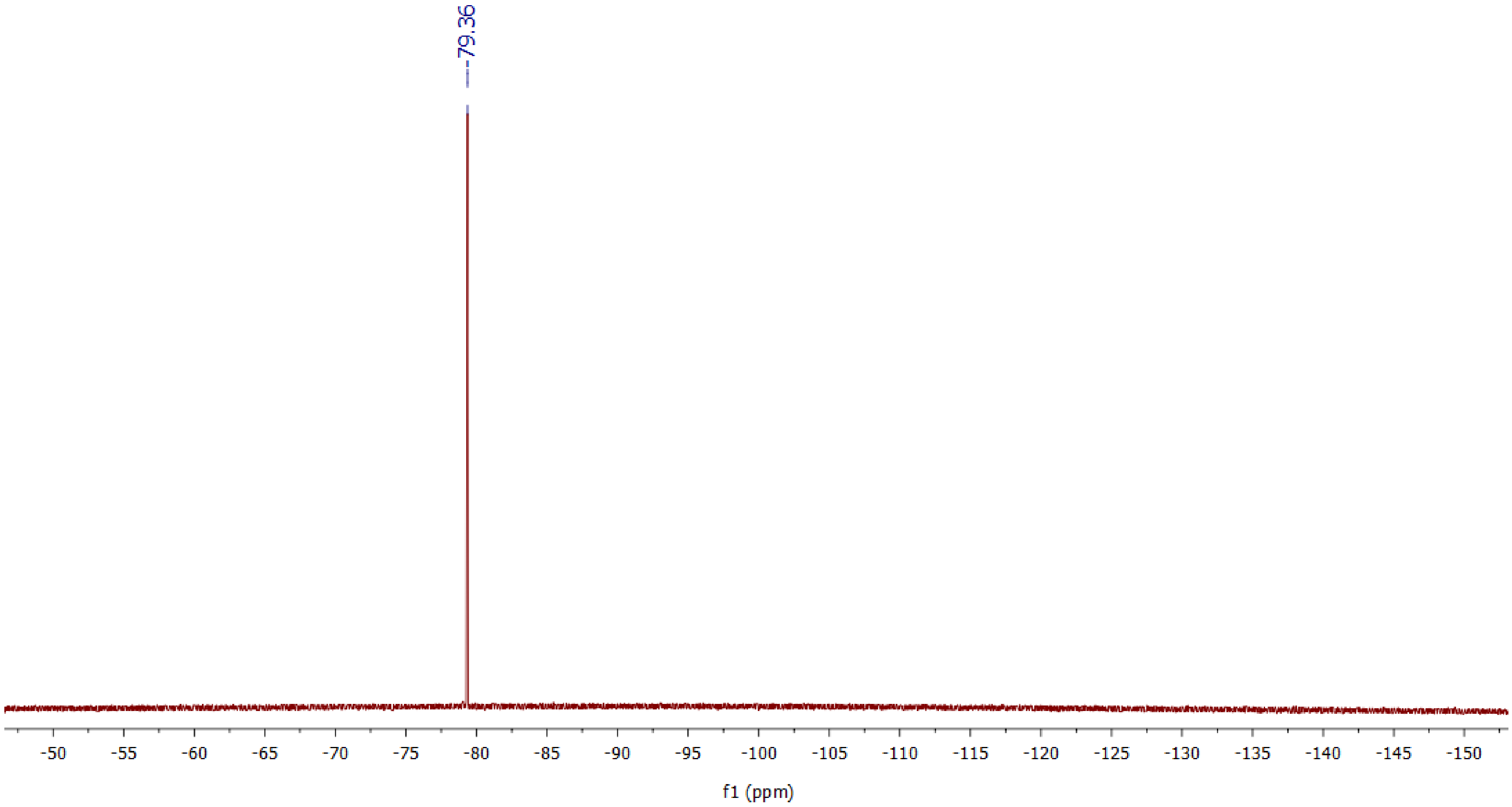

Figure S4. ^{19}F-NMR spectrum of **1** in CD_3CN.

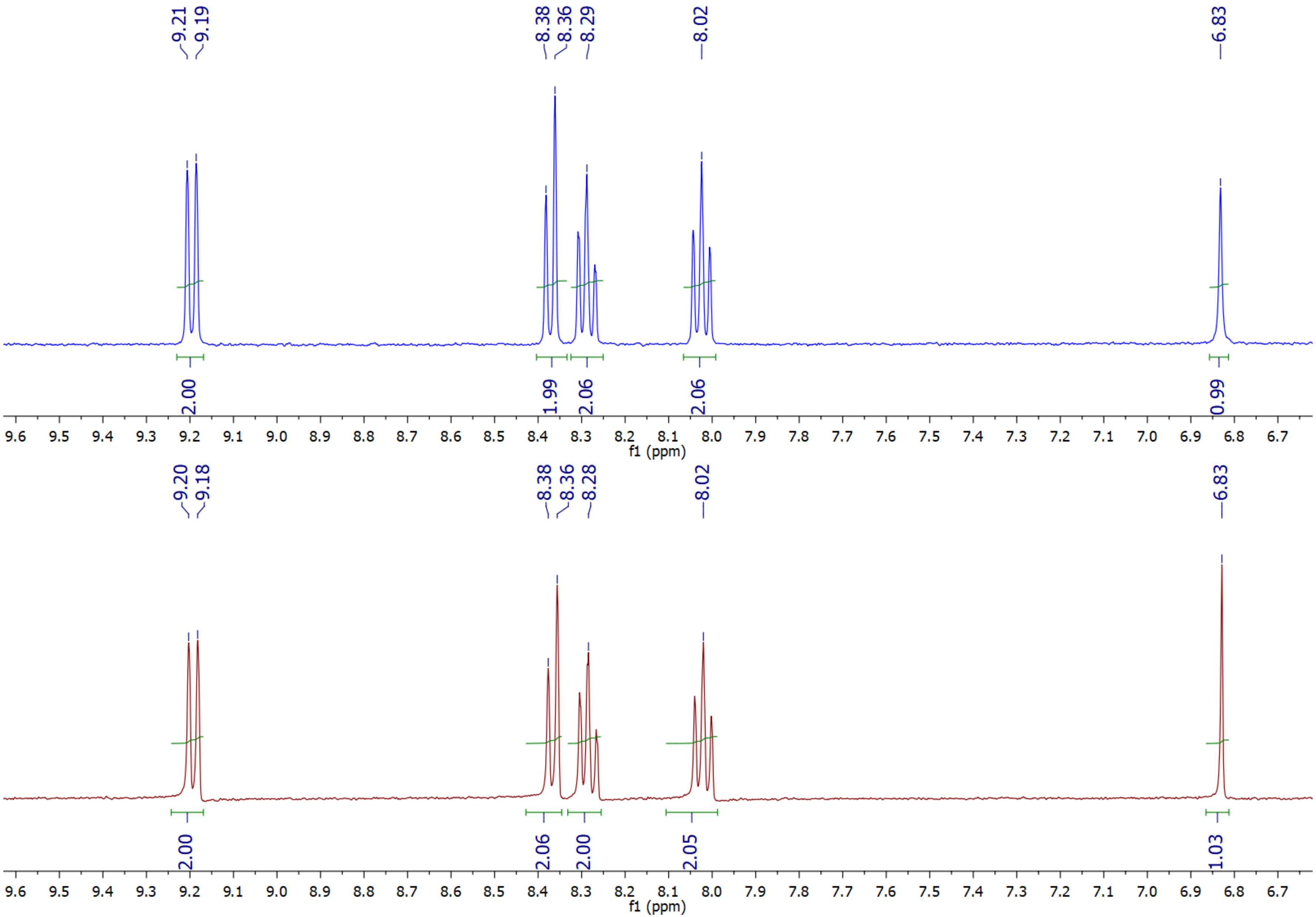

Figure S5a. ^{1}H-NMR spectra (aromatic region) of **1** (1.3 mM; bottom, red), and of **1** with 500 equivalents of NEt_3 added (0.65 M; top, blue), in CD_3CN.

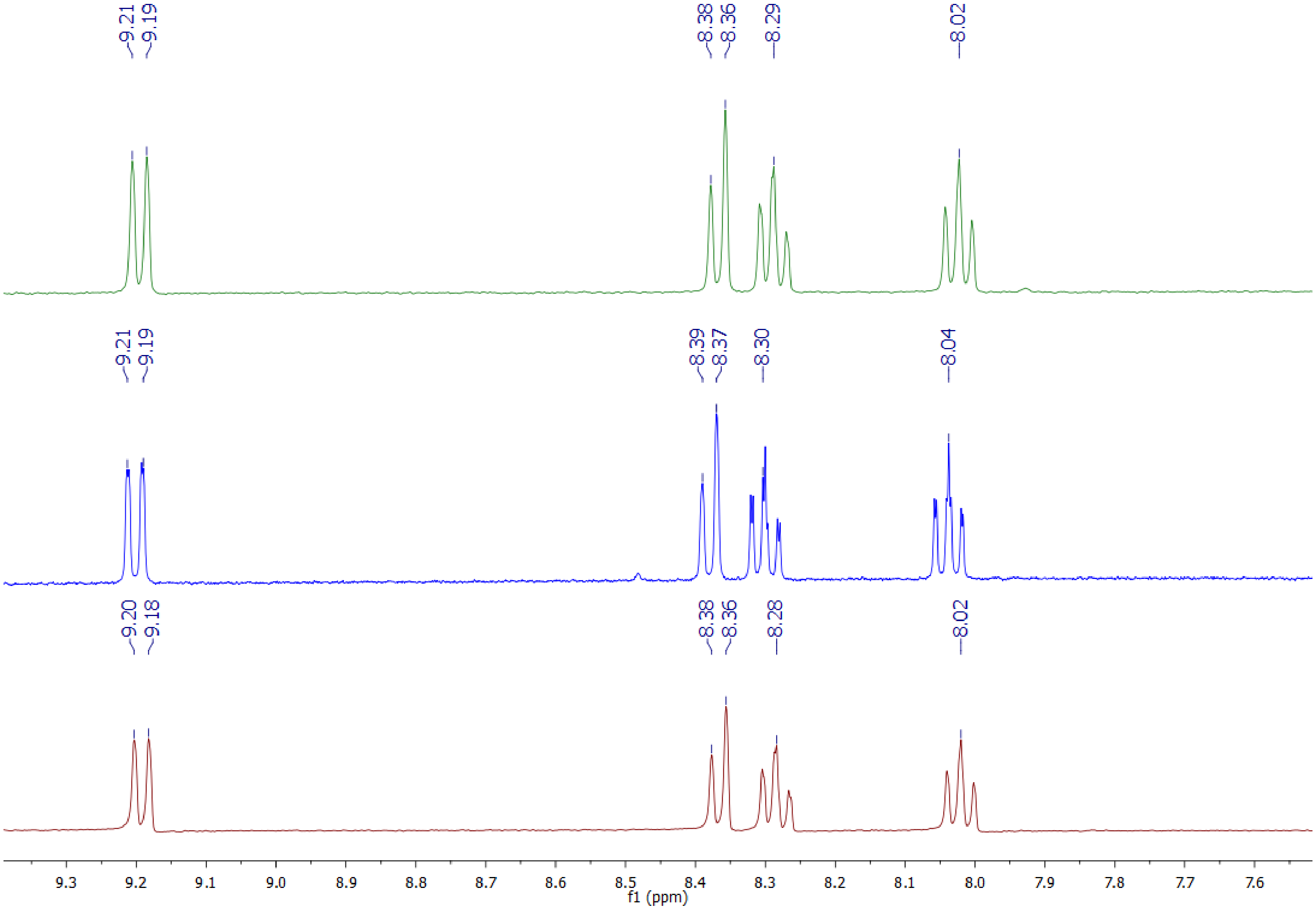

Figure S5b. ^{1}H-NMR spectra (aromatic region) of **1** (1.1 mM; bottom, red), of **1** with 500 equivalents of DMA added (0.55 M, middle, blue), and of **1** with 120 equivalents of [(N(CH$_2$Mes)Cy$_2$)] added (0.13 M, top, green), in CD$_3$CN.

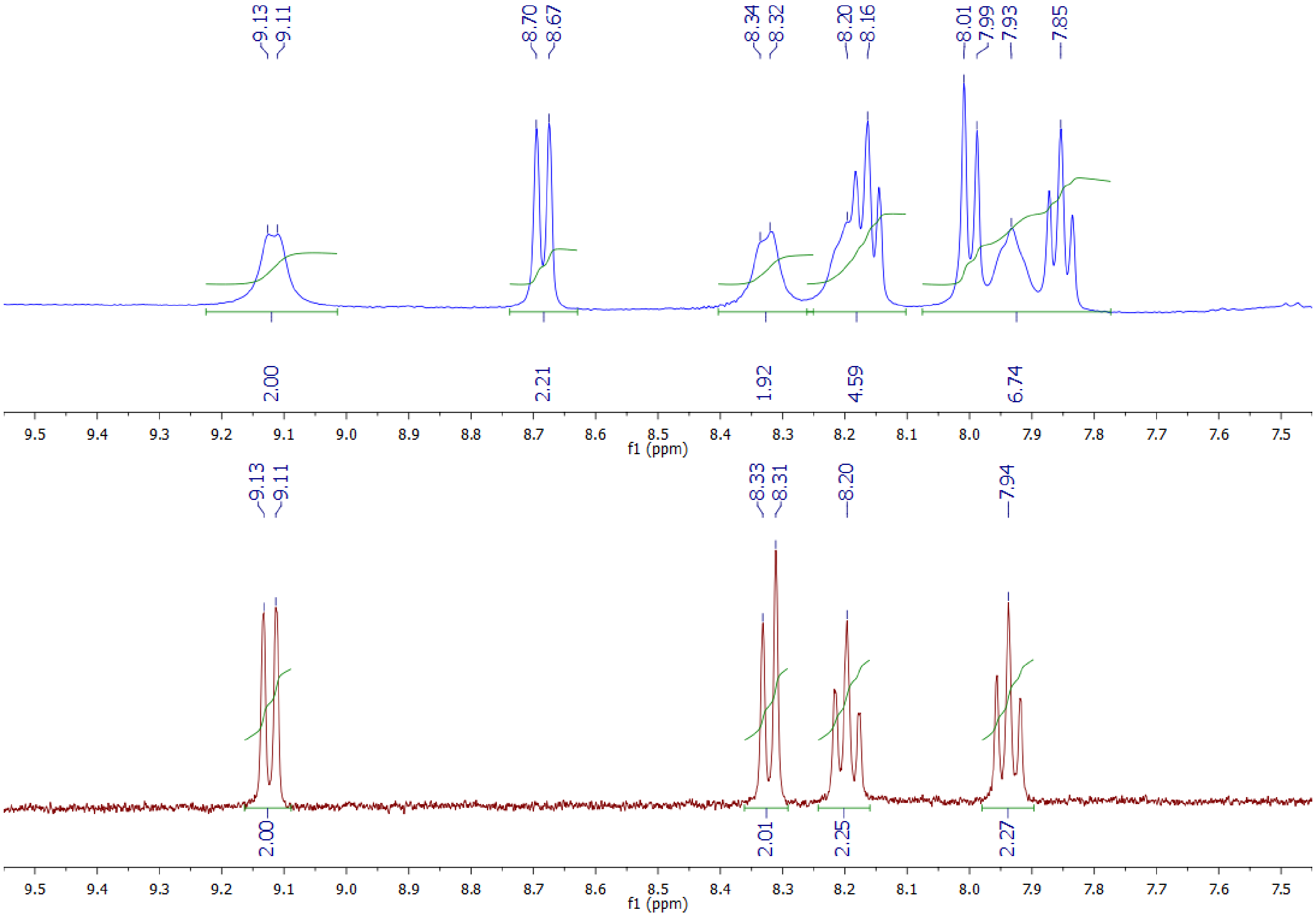

Figure S6. ^{1}H-NMR spectra (aromatic region) of **2** (5.6 mM; bottom, red), and of **2** with 500 equivalents of NEt_3 added (2.8 M; top, blue), in CD_3CN. The additional lines around 8.68, 8.16, 8.00 and 7.85 ppm in the latter spectrum indicate the presence of a second species, which we tentatively assign to the Zn-complex with coordinated Et_3N.

Absorption and Emission Spectra

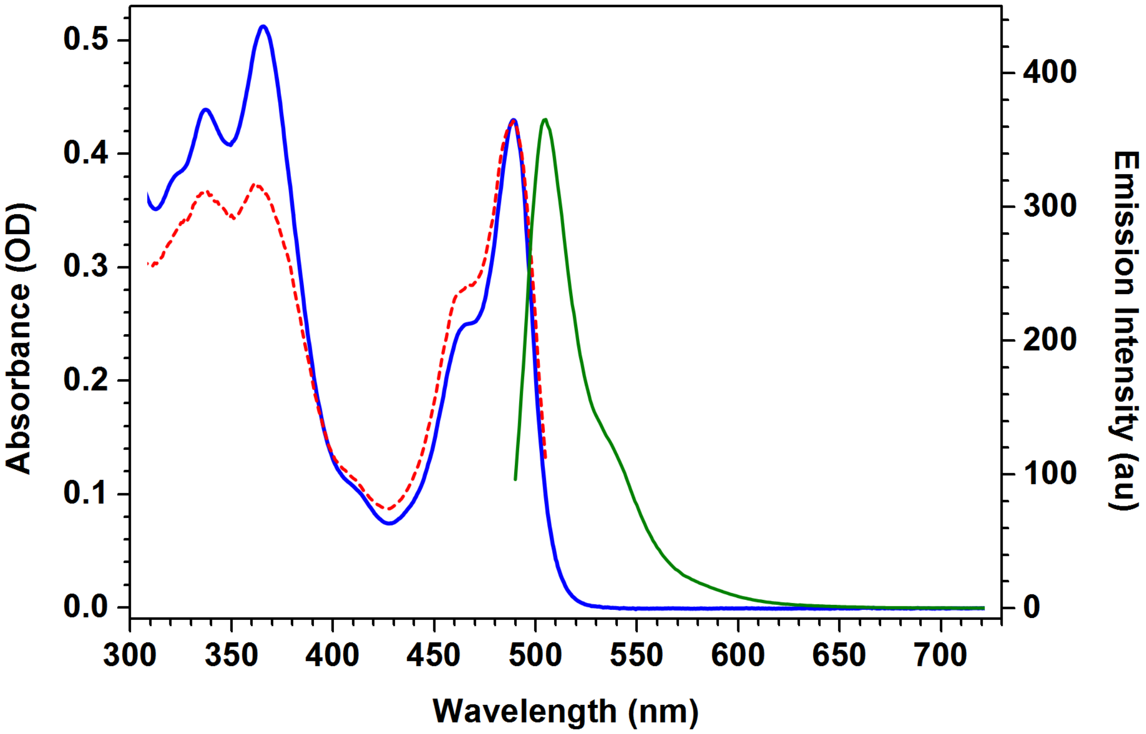

Figure S7a. Absorbance (blue line), emission (λ_{exc} = 489 nm, green line) and excitation spectra (λ_{em} = 505 nm, red dotted line) of **2** in DCM.

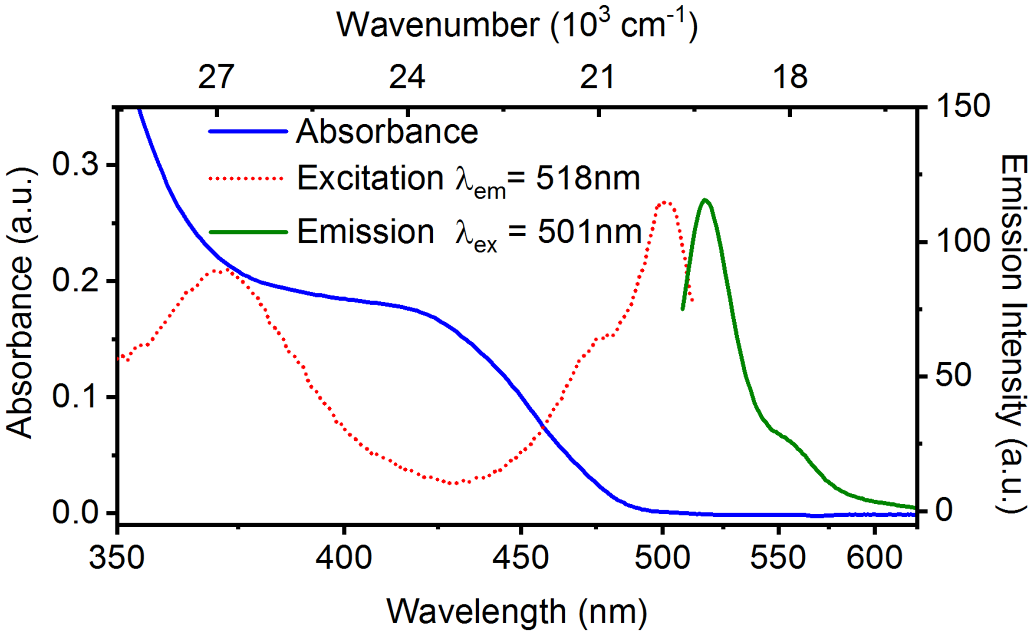

Figure S7b. Absorbance (blue line), emission (green line) and excitation (red dotted line) spectra of HMabiq in DCM.

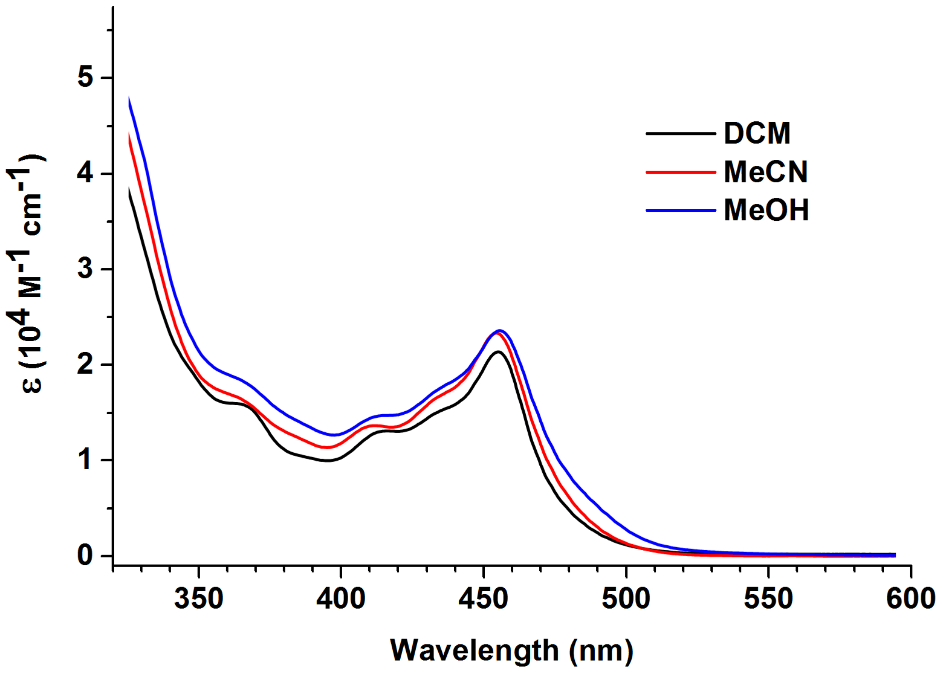

Figure S8. Absorption spectra of **1** in various solvents; DCM (black line), MeCN (red line), MeOH (blue line).

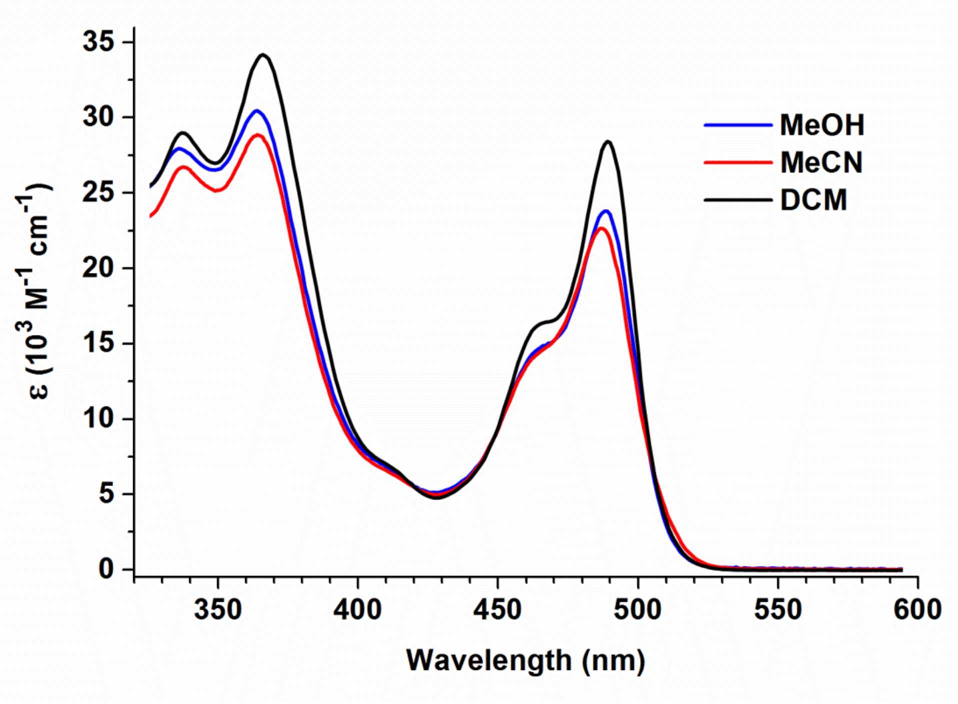

Figure S9. Absorption spectra of **2** in various solvents; DCM (black line), MeCN (red line), MeOH (blue line).

Fluorescence Quantum Yield Determination for 2

The fluorescence quantum yield can be determined using the following equation:

$$\Phi_x = \Phi_{\mathrm{st}} \cdot \frac{grad_x}{grad_{st}} \cdot \frac{n_x^2}{n_{st}^2} \tag{S1}$$

Where:

Φ_{st} = quantum yield of the standard

$grad_x$ = slope of the emission-absorption plot of the sample

$grad_{\mathrm{st}}$ = slope of the emission-absorption plot of the standard

n_x = refractive index of the sample solvent

n_{st} = refractive index of the standard solvent

Fluorescein was chosen as the standard. Solutions of Fluorescein were prepared in 0.1 M NaOH, such that the absorption of the molecule at 491 nm was between 0.02 and 0.1 for each solution. Sample solutions of **2** were prepared in DCM and the concentrations were chosen according to the same criteria. The excitation wavelength for these experiments was λ_{ex} = 480 nm.

The plot of the absorbance vs. emission data are provided below.

The fit of the data yields:

$grad_{\mathrm{st}}$ = 5.7 x 10^8 counts/s

$grad_x$ = 4.5 x 10^8 counts/s

Using the known values[13] for:

n_x = 1.42

n_{st} = 1.33

Φ_{st} = 0.79

a fluorescence quantum yield for **2** of Φ_{x} = 0.71 is obtained.

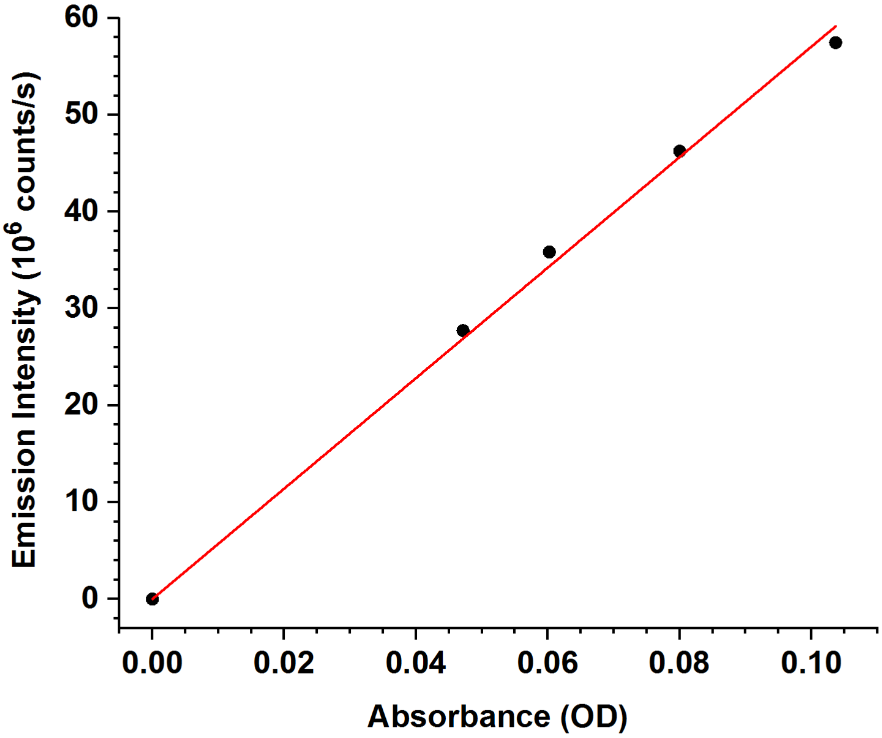

Figure S10. Plot of the emission maximum vs. absorbance for Fluorescein.

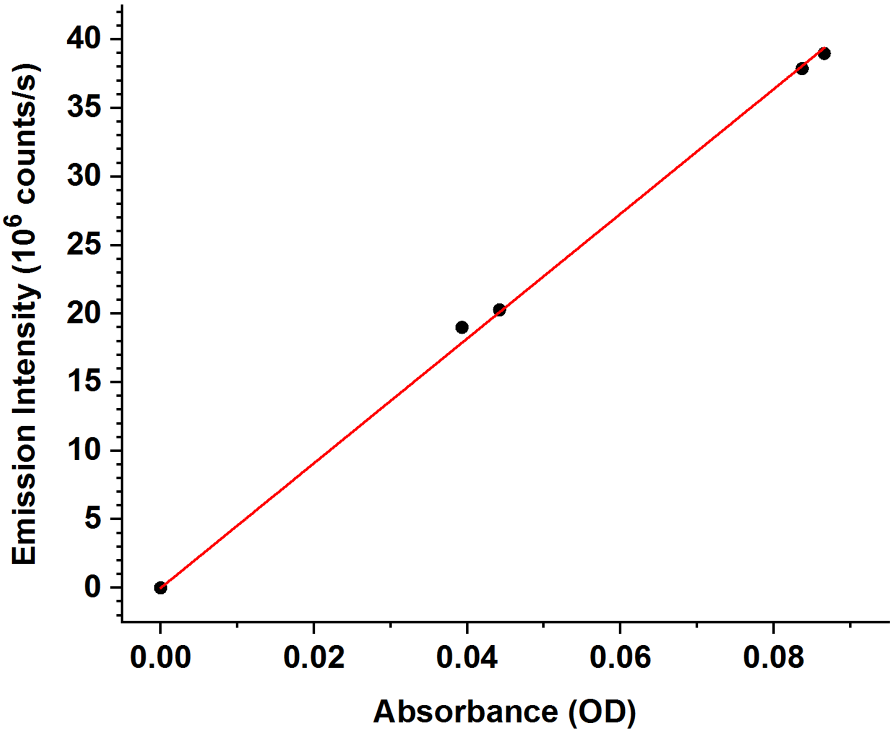

Figure S11. Plot of the emission maximum vs. absorbance for **2**.

Determination of the quantum yields for photoreduction of the M-Mabiq complexes using the Quantum Yield Determination Setup (QYDS)

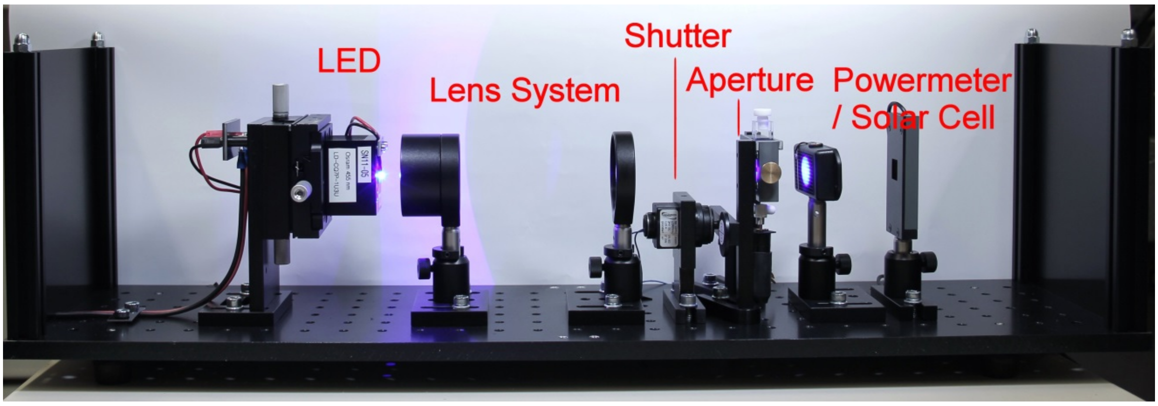

Figure S12. Picture of the quantum yield determination setup.

QYDS Instrumentation

For the photochemical reduction of both **1** and **2**, the quantum yield *Φ* of the reaction was determined using a quantum yield determination setup (QYDS).[2, 3] The components are contained within a black box to protect the sample from any external light sources, and the experimenter from the intense stray light. A high-power LED (λ_{exc} = 455 nm) of type LD-CQ7P-1U3U produced by Osram was used as the excitation light source. The current for the LED was controlled by a power supply of type RND 320-KA3005P from RND lab. The lens system consists of a Thorlabs aspheric condenser lens (f = 32 mm, 50 mm diameter) and a Thorlabs plano-convex lens (f = 100 mm, 50 mm diameter). The light bundle was imaged through an aperture (8 mm x 8 mm square) in front of the cuvette holder and onto the middle of the cuvette. A shutter was placed between the lens system and the aperture to interrupt the incoming light beam during the measurement, as warranted.

The 10 mm x 10 mm fused silica sample cuvette was fitted with a J-Young valve. The volume of the sample solutions was 2 mL. During the irradiation period the solutions were rigorously stirred. The transmitted light power of the sample solution (P_{sample}) was detected using a Thorlabs power meter of type S175C. To determine the reference power (P_{ref}) a cuvette containing 2 mL of solvent was irradiated using the same input power settings as for the sample. The measurements were monitored and data was recorded using a Labview program developed by the Riedle group, which displays the total illumination time. The incoming light beam was interrupted via a shutter control box, at which point the timer also was paused. The cuvette was subsequently transferred to the Cary 60 UV-vis instrument and an absorption spectrum was recorded. The cuvette was placed back into the QYDS and the illumination was continued. For each time period the illumination time (Δt), transmitted power (P_{sample}) and the LED driver voltage (U) and current (I) were recorded in a log file.

Numerical determination of reaction quantum yields, Φ

The reaction quantum yield Φ for the reaction of species A to product B was calculated by numerically integrating the following differential equation using the quantum yield as fit parameter:

$$\frac{dN_B(t)}{dt} = +\Phi \int \frac{c_A(t)\varepsilon_A(\lambda)}{c_A(t)\varepsilon_A(\lambda) + c_B(t)\varepsilon_B(\lambda)} \frac{P_{ref} \cdot f(\lambda) \cdot \lambda}{h \cdot c} \mathrm{Abs}(t,\lambda)\, d\lambda \qquad (\text{S2})$$

and

$$\mathrm{Abs}(t,\lambda) = 1 - 10^{-d \cdot [c_A(t)\varepsilon_A(\lambda) + c_B(t)\varepsilon_B(\lambda)]} \qquad (\text{S3})$$

Where:

$N_X(t)$ = number of molecules of species x at time t

$c_x(t)$ = concentration of species x at time t

$\varepsilon_x(\lambda)$ = extinction coefficient of species x for wavelength λ

$f(\lambda)$ = spectral distribution of the LED light

Abs(t, λ) = absorbance of the sample at time t and wavelength λ

d = thickness of the cuvette (10 mm)

The center excitation wavelength used in the experiments was λ = 455 nm.

The following constants were used:

$$\boldsymbol{h} = 6.626 \cdot 10^{-34}\ \mathrm{J \cdot s}$$

$$\boldsymbol{c} = 299\ 792\ 458\ \mathrm{m/s}$$

The integral in the right hand side of eq. (S2) reflects the fact that the molecules absorb the LED light in a wavelength dependent fashion, which has to be considered for the given spectral width of the LED light. The first term under the integral describes the illumination time dependent absorption of photons by both the substrate and product molecules. The spectral distribution of the LED light and the molar absorption coefficients are treated precisely. By this approach we can utilize the full data set from the beginning of the illumination up to the full conversion to the photostationary equilibrium. We do not have to rely on an estimate up to which time the conversion is linear. In addition, the much higher concentrations and optical densities used lead to a dramatically improved accuracy. The overall precision has been shown to be better than 5 % of the measured quantum yield value.[3]

Reactions with side product

For cases where more than one product was found and for cases of a partially reversible reaction the side product reconstruction was performed according to the TEM method developed by Thulstrup, Eggers, and Michl.[14-16] The method uses a linear combination approach combined with an analysis of a specific vibronic structure that disappears in the spectrum of the side product. The analysis of the second derivative of the difference spectra enables to determine the amount of side product in the PSS.

In this case eqs. (S2) and (S3) have to be generalized. To make them more readable, we first define some auxiliary quantities:

$$\mathrm{Frac}_A = \frac{c_A(t)\cdot\varepsilon_A(\lambda)}{\sum_{i=1}^{n} c_i(t)\cdot\varepsilon_i(\lambda)} \qquad (\text{S4})$$

is the fraction of photon absorbed by species A, with n different species considered. The fraction for the other species is defined analogously. The total absorption of the sample is given as:

$$\mathrm{Abs}(t,\lambda) = 1 - 10^{-d\cdot\left(\sum_{i=1}^{n} c_i(t)\cdot\varepsilon_i(\lambda)\right)} \qquad (\text{S5})$$

and the number of photons per second by:

$$N_{Ph}(\lambda)\left[\frac{1}{s}\right] = \frac{P_{ref}\cdot f(\lambda)\cdot\lambda}{h\cdot c} \qquad (\text{S6})$$

At present we consider the following situation:

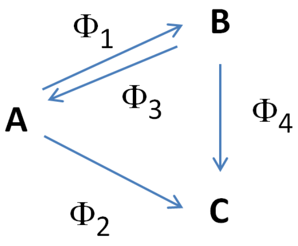

This scheme allows the direct product of **B** and **C** after illumination of **A** with yields Φ_1 and Φ_2. Since the transformation from **A** to **B** is by electron transfer, we also allow the back transfer with yield Φ_3. Finally, we find that **B** can also be photoexcited, according to the overlapping absorption spectra, and produces **C** with yield Φ_4.

This then results in the following system of differential equations:

$$\frac{dN_A(t)}{dt} = \int \left[-(\phi_1 + \phi_2)\,\mathrm{Frac}_A(t,\lambda) + \phi_3 \cdot \mathrm{Frac}_B(t,\lambda) \right] N_{Ph}(\lambda) \cdot \mathrm{Abs}(t,\lambda)\, d\lambda \qquad (\text{S7})$$

$$\frac{dN_B(t)}{dt} = \int \left[\phi_1 \cdot \mathrm{Frac}_A(t,\lambda) - (\phi_3 + \phi_4)\,\mathrm{Frac}_B(t,\lambda) \right] N_{Ph}(\lambda) \cdot \mathrm{Abs}(t,\lambda)\, d\lambda \qquad (\text{S8})$$

$$\frac{dN_C(t)}{dt} = \int \left[\phi_2 \cdot \mathrm{Frac}_A(t,\lambda) + \phi_4 \cdot \mathrm{Frac}_B(t,\lambda) \right] N_{Ph}(\lambda) \cdot \mathrm{Abs}(t,\lambda)\, d\lambda \qquad (\text{S9})$$

We solve them by numerical integration (propagation) in Mathcad Prime 5.0 and use standard least square fitting to find the best values for the yields.

The reaction quantum yield analysis results not only in a number, but it can describe the data qualitatively. By the careful analysis of the data the information about the reaction mechanism can be extracted.

Sample preparation for photoreduction experiments

The samples were prepared under an argon atmosphere inside a glove box and under red light conditions. A cuvette fitted with a J-Young valve and stir bar was used for all measurements. The sealed cuvette was removed from the glove box, ensuring that no light reached the sample, and an absorption spectrum was taken. This measurement gave the reference absorption spectrum prior to LED illumination (t = 0 spectrum). The cuvette was then transferred into the QYDS setup, the sample was irradiated for various time periods and an absorption spectrum was measured after each time period (see Figures S13 – S19 and S21 – S24 for data).

*Photoreduction experiments with **1***: Stock solutions of **1** (330.9 μM) and Et_3N (63 mM) were prepared in THF/MeCN 1:1. 0.4 mL of the stock solution of **1** was mixed with 0.54 mL of the solvent THF/MeCN 1:1 and 1.06 mL of the NEt_3 stock solution, such that the final sample concentrations were: [**1**] = 67 μM, [Et_3N] = 33.5 mM; **1**:Et_3N = 1:500. Samples for the Fe- and Co-Mabiq complexes were prepared in a similar manner, also using ~500 equiv. Et_3N: M-Mabiq complex.

*Photoreduction experiments with **2***: Stock solutions of **2** and Et_3N were prepared in THF/MeCN 1:1. Measurements were carried out on samples containing **2**:Et_3N ratios of either 1:500 (sample *A*) or 1:5 (sample *B*).

Sample *A*: 1 mL of the stock solution of **2** (154 μM) was mixed with 1 mL of the NEt_3 stock solution (77 mM). [**2**] = 77 μM, [Et_3N] = 38.5 mM.

Sample *B*: 120 μL of the stock solution of **2** (1.15 mM) was mixed with 70 μL of the Et_3N stock solution (9.86 mM), followed by 1.81 mL of solvent (THF/MeCN 1:1). [**2**] = 69 μM, [Et_3N] = 345 μM.

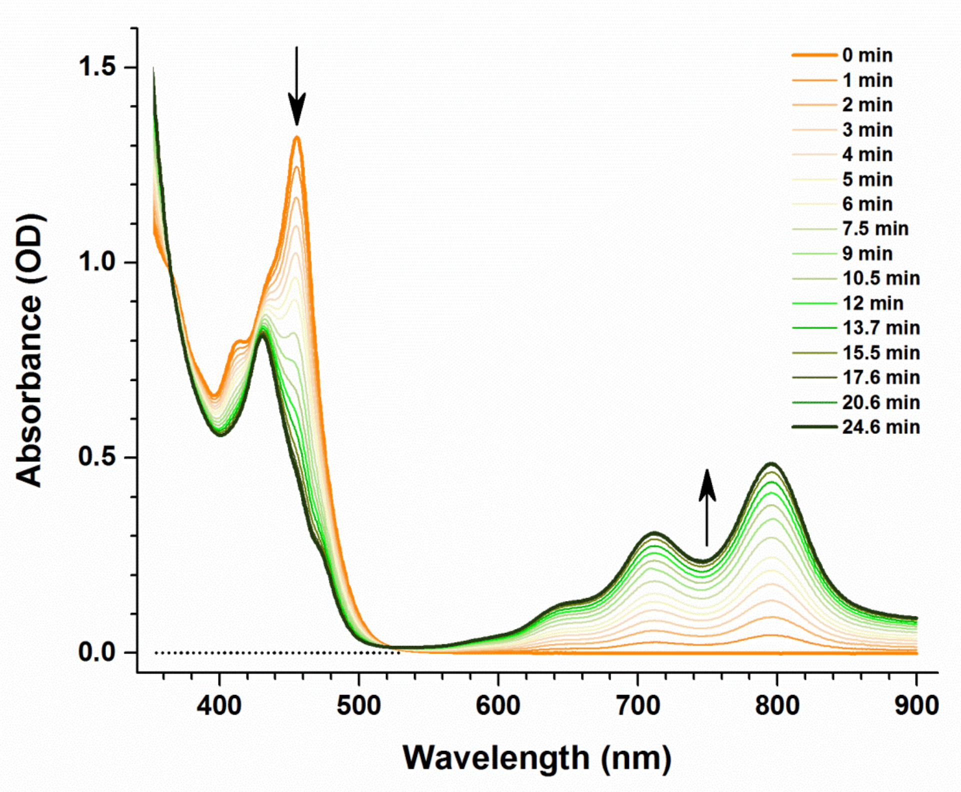

Figure S13. Spectral changes during the photoreduction of **1** starting from *t* = 0 (orange trace) until *t* = 24.6 min (black trace). [**1**] = 67 µM, [Et_3N] = 33.5 mM, THF:MeCN = 1:1; P_{ref} = 245 mW; Φ = $2.9 \cdot 10^{-4}$. $\mathbf{1}^{red}$ exhibits further absorption bands in the NIR (see Figure S20).

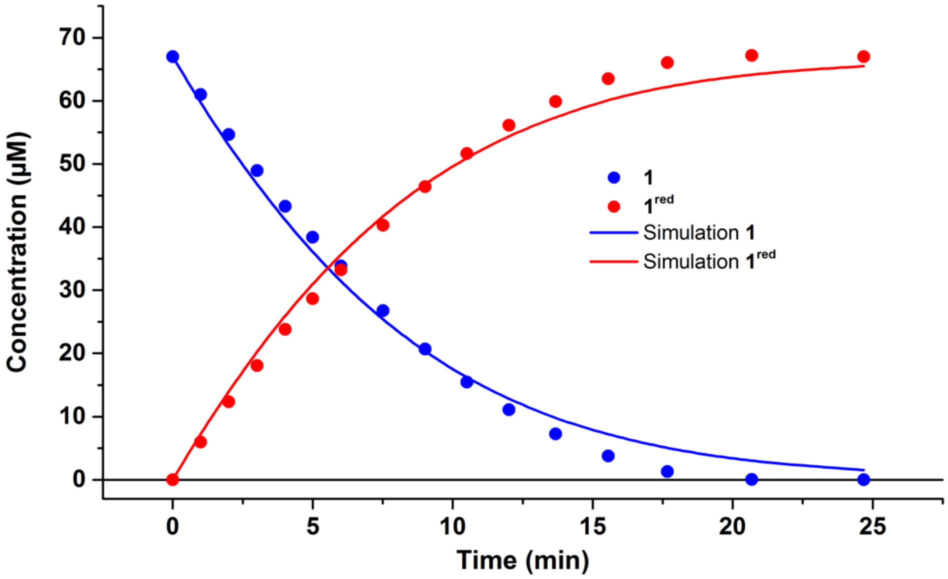

Figure S14. Evaluation of the data from Figure S13: concentration of **1** and $\mathbf{1}^{red}$ vs. irradiation time for the photoreduction of **1**. To fit the quantum yield, the reaction up to the full conversion is simulated with the rate model given by eq. (S2). The resulting value is $\Phi = 2.9 \times 10^{-4}$.

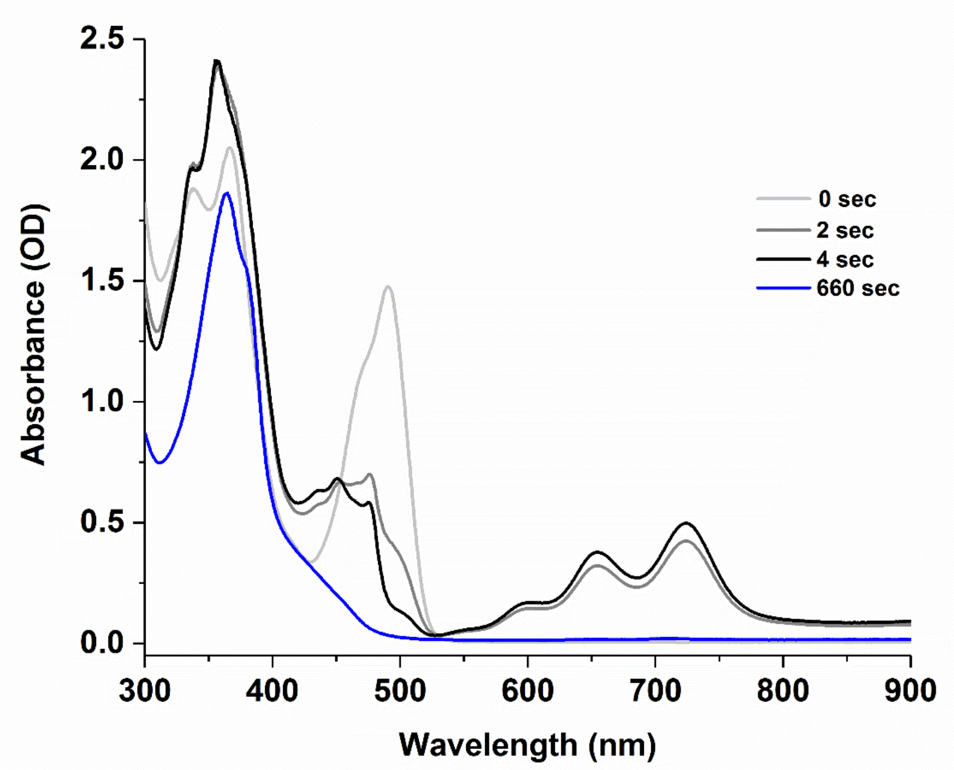

Figure S15. Spectral changes after the photoreduction of **2**. [**2**] = 77 µM, [Et_3N] = 38.5 mM, THF:MeCN = 1:1; P_{ref} = 248 mW. The light gray line depicts the spectrum of **2** prior to photoreduction. The formation of $\mathbf{2}^{\mathbf{red}}$ is complete after just four seconds (black line), after which product degradation is observed. The final spectrum of the decay product (660 s irradiation time) is shown by the blue line.

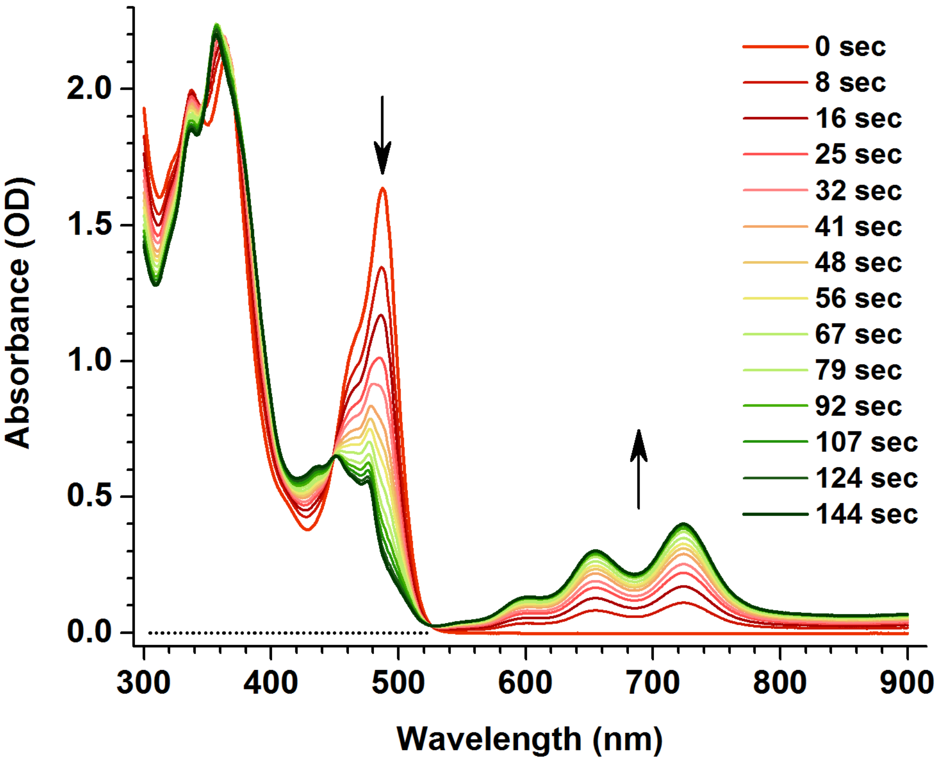

Figure S16. Spectral changes during the photoreduction of **2**, showing the initial changes leading to formation of $\mathbf{2}^{\mathrm{red}}$; [**2**] = 69 μM, [$Et_3N$] = 345 μM, THF:MeCN = 1:1; P_{ref} = 1.405 mW. Φ = 0.79; $\mathbf{2}^{\mathrm{red}}$ exhibits further absorption bands in the NIR (see Figure S20).

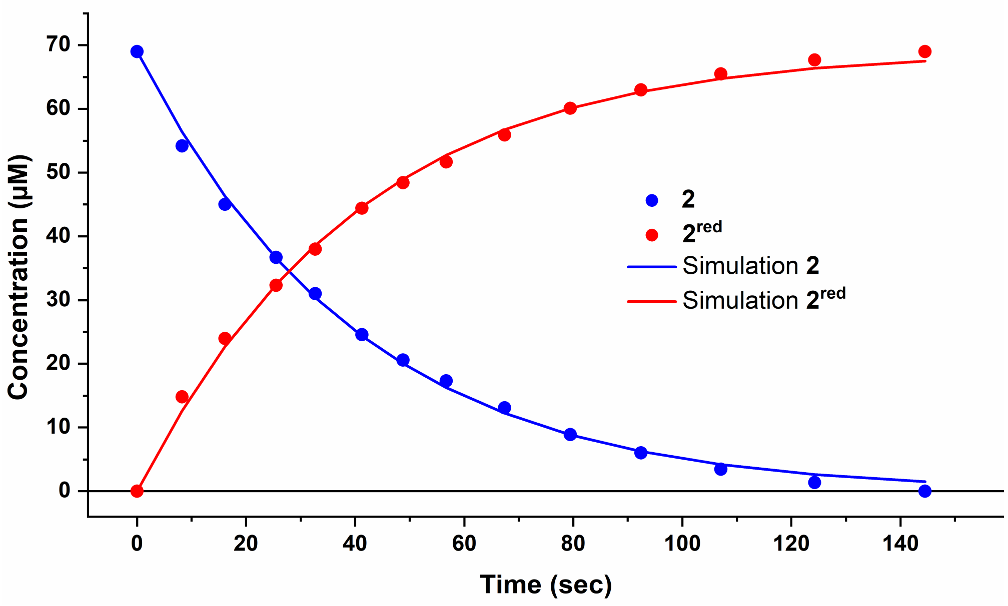

Figure S17. Evaluation of the data from Figure S16: concentration of $\mathbf{2}^{\mathrm{red}}$ vs. irradiation time for the photoreduction of **2**. To fit the quantum yield, the reaction up to the full conversion is simulated with the rate model (eq. (S2)).

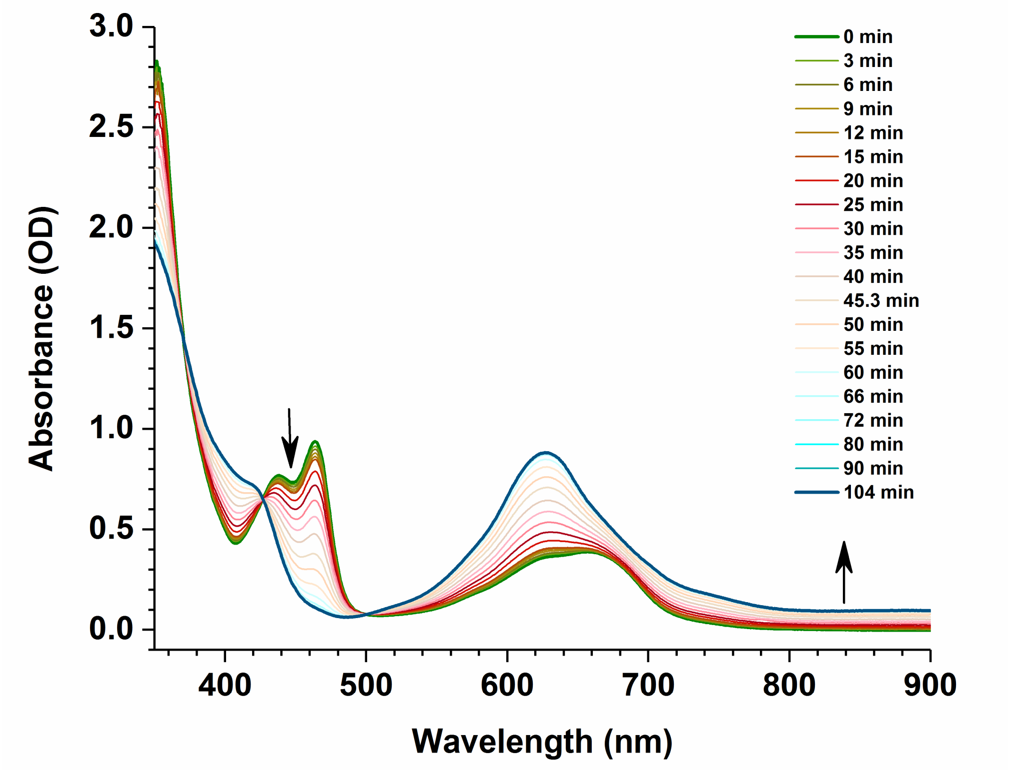

Figure S18. Spectral changes during photoreduction of $[Fe(Mabiq)(MeCN)_2]PF_6$; c = 66 μM, $[Et_3N]$ = 33 mM, THF:MeCN = 1:1; P_{ref} = 245 mW. The reduced Fe-Mabiq species exhibits further absorption bands in the NIR (see Figure S20).

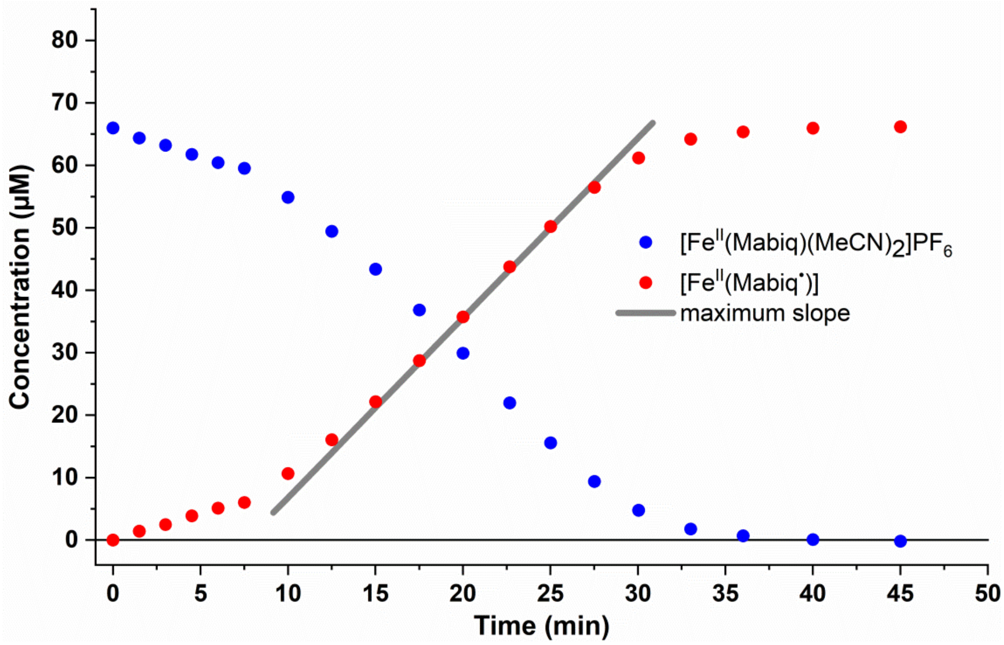

Figure S19. Evaluation of the data from Figure S18: the quantum yield of Φ = 1.8×10^{-4} was determined from the highest slope after the initial induction period.

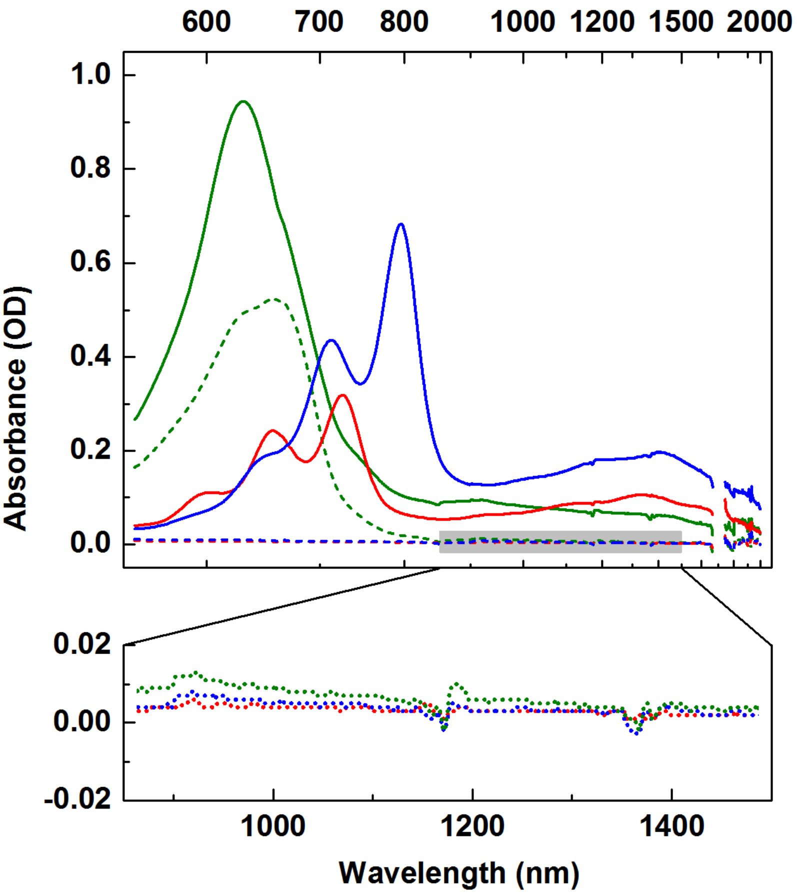

Figure S20. VIS-NIR absorption spectra of $\mathbf{1}^{\mathrm{red}}$ (blue solid line), $\mathbf{2}^{\mathrm{red}}$ (red solid line) and the reduced form of the $[\mathrm{Fe}^{\mathrm{II}}(\mathrm{Mabiq})(\mathrm{MeCN})_2]\mathrm{PF}_6$ complex (green solid line) generated upon photoreduction of the respective divalent complexes; [**1**] = 68 µM, [**2**] = 75 µM, [Fe] = 80 µM, $\mathrm{Et_3N}$ = 10 equiv.; 1:1 THF:MeCN. The spectrum of $\mathbf{2}^{\mathrm{red}}$ was measured when the absorbance of the reduced species at λ = 724 nm reached the maximum. For comparison, the spectra of the complexes in the NIR region are shown prior to photoreduction on an expanded scale; **1** = blue dashed line; **2 =** red dashed line; $[\mathrm{Fe}^{\mathrm{II}}(\mathrm{Mabiq})(\mathrm{MeCN})_2]\mathrm{PF}_6$ = green dashed line.

The small wiggles in the NIR are due to slightly unbalanced signals of MeCN overtone lines in the two-beam spectrophotometer. The very large signal around 1700 nm obscures the molecular spectra and is therefore masked in the figure.

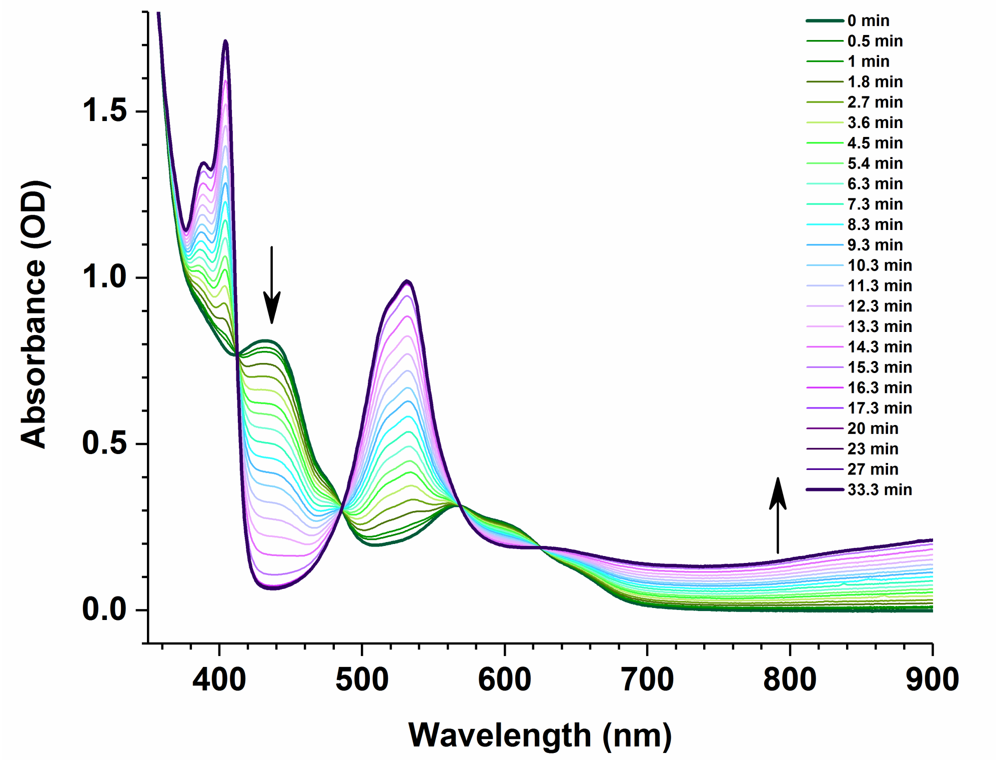

Figure S21. Spectral changes during photoreduction of [Co^{II}(Mabiq)(THF)]PF$_6$. *c* = 77 µM, [Et$_3$N] = 38.5 mM, THF:MeCN = 1:1; P_{ref} = 245 mW. Φ = 3.6 x 10^{-4}.

The reduced 'Co^{I}' species exhibits further absorption bands in the NIR region, at λ_{max} = 913, 1048 and 1210 nm. The spectrum of this compound was previously reported.[17]

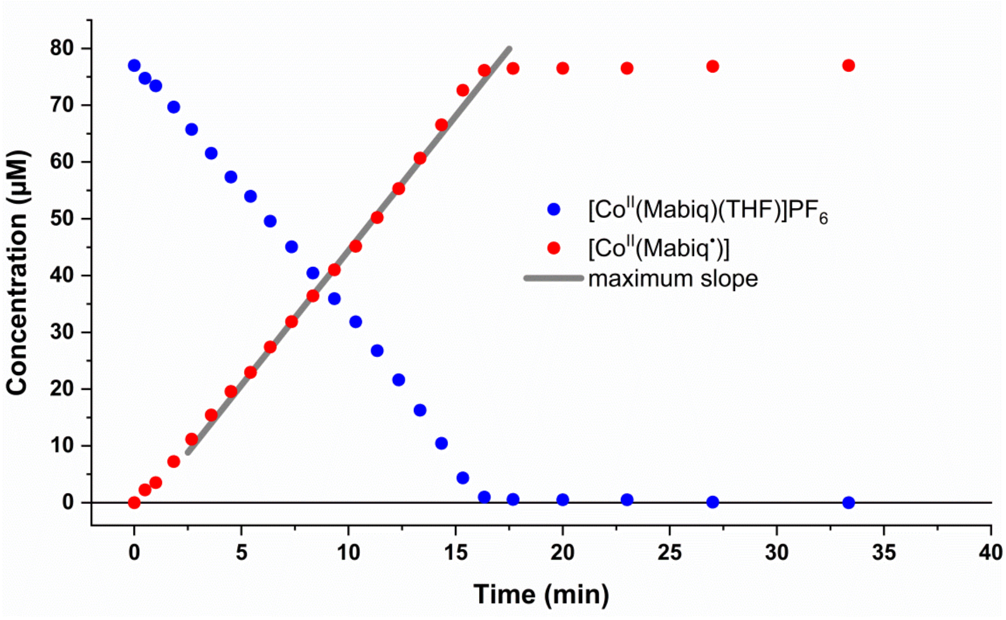

Figure S22. Evaluation of the data from Figure S21: the quantum yield of Φ = 3.6 x 10^{-4} was determined from the highest slope after the initial induction period.

In case of the photoreduction of **1** by a bulky quencher N(CH$_2$Mes)Cy$_2$ (for illumination time dependent spectra see Figure S23 top)) a simple reaction model from **1** to **1^{red}** cannot explain the observed trend in the data. Additionally, a side product is apparently created and increases with time. According to our analysis (for algorithm see above) and experimental observations, the side product has absorption bands between the deep UV and the 500 nm region (see Figure S25) and consequently it can also absorb part of the irradiation light.

The results show, that the quenching reaction from **1** to **1^{red}** is dominant with the quantum yield of 2.1 x 10^{-4}. The main channel for the creation of the side product originates from the repeated excitation of the product **1^{red}** followed from the direct reaction from the reactant. The order of magnitude for the photoinduced backreaction is comparable with the creation of the side product directly from the reactant. The further illumination would result in the increasing concentration of the side product and decreasing concentration of the desired **1^{red}**.

The photoinduced reduction by DMA as a quencher (see Figure S24) revealed a predominant backreaction from **1^{red}** to **1** with a high quantum yield of 2.7 x 10^{-4}. This value is one order of magnitude higher than the classical light promoted reduction from **1** to **1^{red}.** The side product originates only from the further excitation of the product molecules. The creation of the side product directly from the reactant can be regarded as negligible.

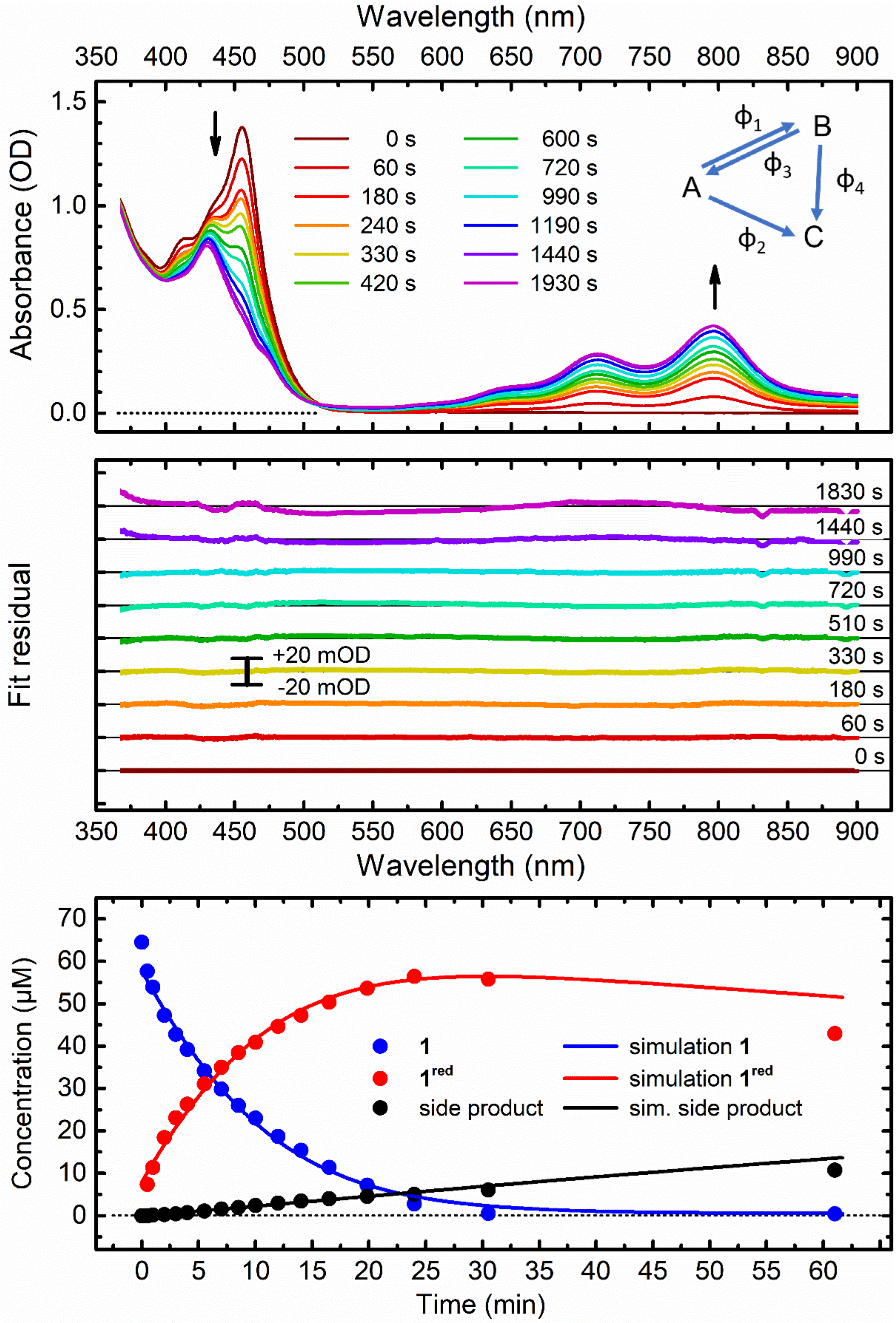

Figure S23. (top) Spectral changes during the photoreduction of **1**. [**1**] = 67 µM, [(N(CH$_2$Mes)Cy$_2$)] = 33.5 mM, THF:MeCN = 1:1; P_{ref} = 245 mW. (middle) Fit residuals resulting from projection of the measured UV/vis data onto basis spectra. (bottom) Time evolution of concentrations with the reaction quantum yields of $\phi_1 = 2.1 \times 10^{-4}$, $\phi_2 = 0.09 \times 10^{-4}$, $\phi_3 = 0.04 \times 10^{-4}$ and $\phi_4 = 0.1 \times 10^{-4}$. The side product amounted 20 % of the reaction mixture upon 61 min of the illumination.

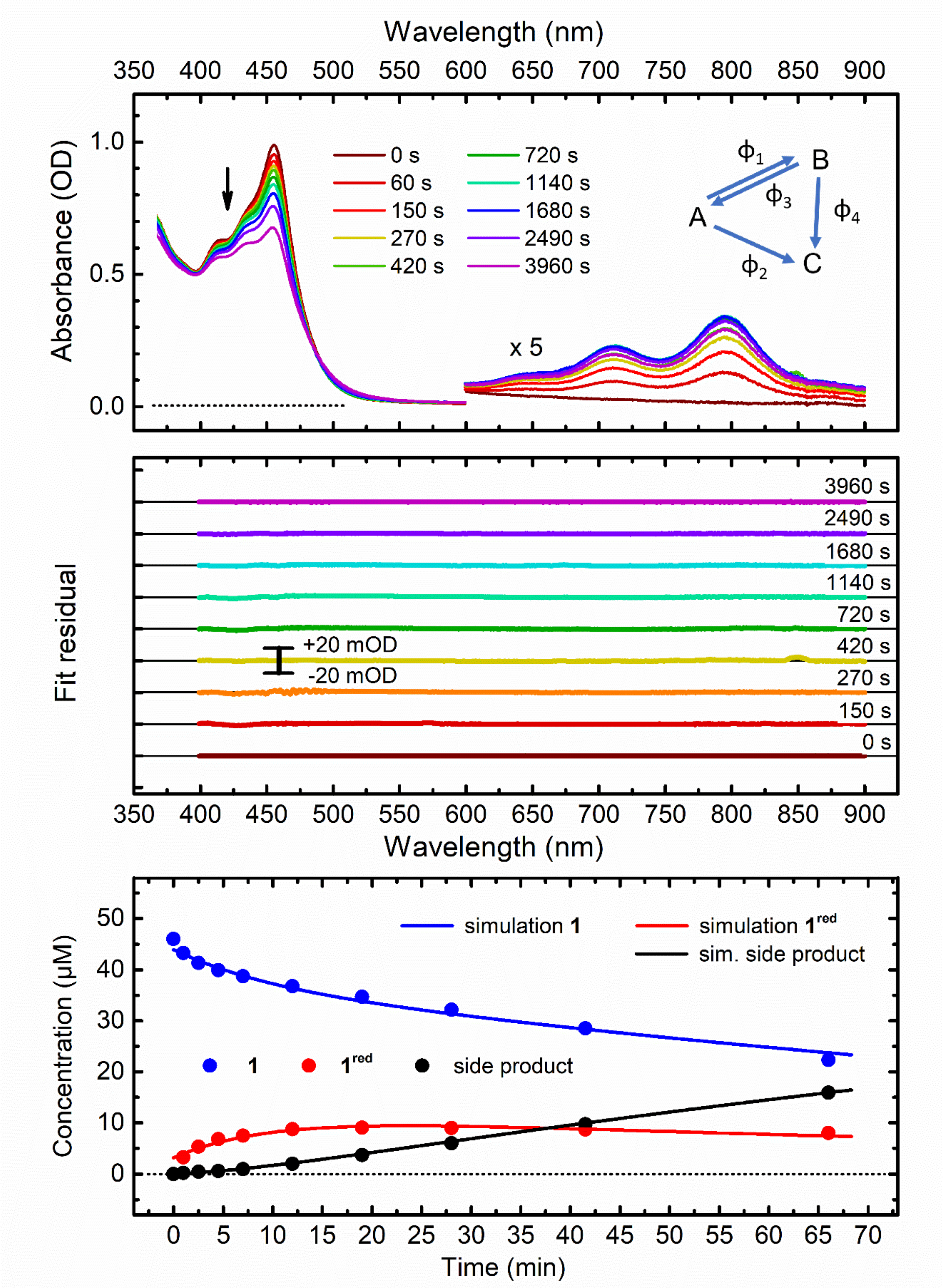

Figure S24. (top) Spectral changes during the photoreduction of 1. [**1**] = 51 µM, [DMA] = 255 mM, THF:MeCN = 1:1; P_{ref} = 245 mW.
(middle) Fit residuals resulting from projection of measured UV/vis data onto basis spectra.
(bottom) Time evolution of concentrations with the reaction quantum yields of $\phi_1 = 0.5 \times 10^{-4}$, $\phi_2 = 0 \times 10^{-4}$, $\phi_3 = 2.7 \times 10^{-4}$ and $\phi_4 = 1.1 \times 10^{-4}$. The side product amounted to 34.5 % and $\mathbf{1}^{\mathbf{red}}$ amounted to 17.4 % of the reaction mixture upon 66 min of illumination.

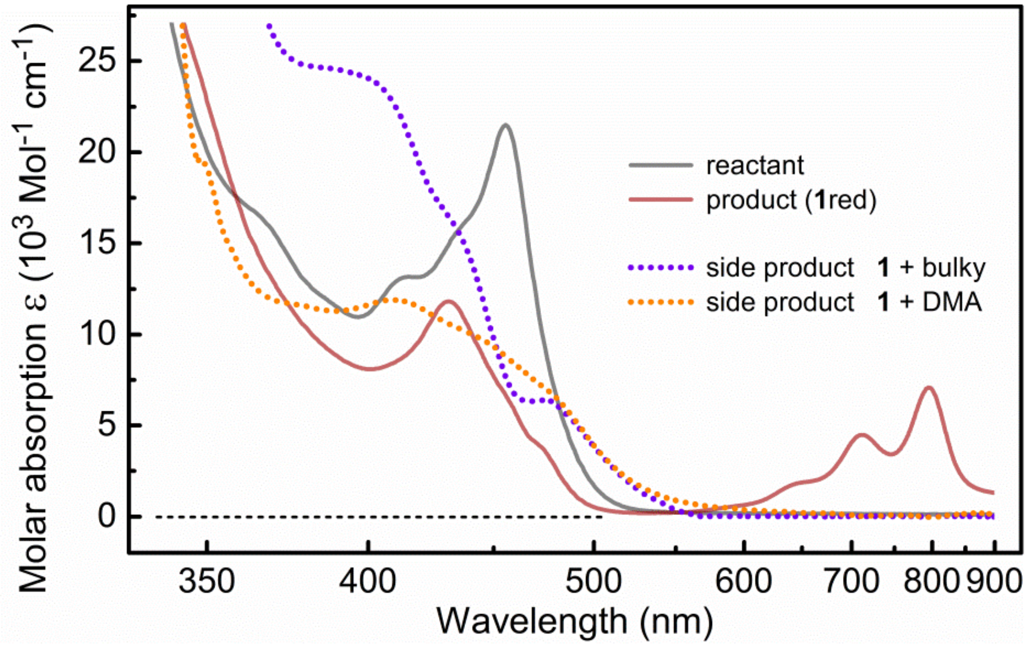

Figure S25. Molar absorption of **1**, **1**^{red} and side products in THF:MeCN = 1:1. The spectrum of the side product was extracted according to the TEM method.[14-16] The violet dotted trace corresponds to the side product resulting from the photoreduction of **1** and the bulky quencher ([(N(CH$_2$Mes)Cy$_2$)]). The orange dotted line shows the side product originating from the photoreduction of **1** with DMA.

Cyclic voltammogram for 2

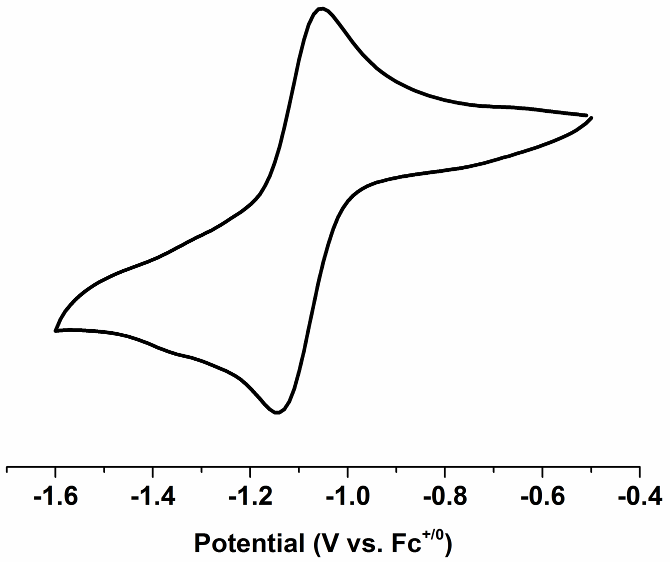

Figure S26. Cyclic voltammogram of **2** (1.1 mM in MeCN; 0.1 V·s^{-1}; 0.1 M [N(n-Bu)$_4$]PF$_6$) depicting the [Zn^{II}(Mabiq)]$^+$/[Zn^{II}(Mabiq$^•$)] couple.

Time-resolved fluorescence lifetime for 2

Experimental setup

In an air-tight fluorescence cuvette (10 mm path length), a solution of **2** in DCM was prepared (c = 30 µM) and the time resolved fluorescence intensity decay of this sample was measured. The light source used was a picosecond laserdiode of type LDH-P-C-405M produced by PicoQuant GmbH. The emission wavelength of this diode is 405 nm. The pulse was shorter than 90 ps with a repetition rate of 2.5 MHz. The laser was controlled by a picosecond pulsed laser driver of type PDL-800D from PicoQuant GmbH. The detector was a single photon counting module of type SPCM-AQR-16 from PerkinElmer Inc.. The timing resolution of this module was 350 ps. The emission decays were recorded by the software Daisy from quTAG.

Fluorescence lifetime determination

The time resolved fluorescence intensity decay of **2** is shown in Figure S31. The data could be fit to a monoexponential decay, yielding a fluorescence lifetime of 1.1 ns.

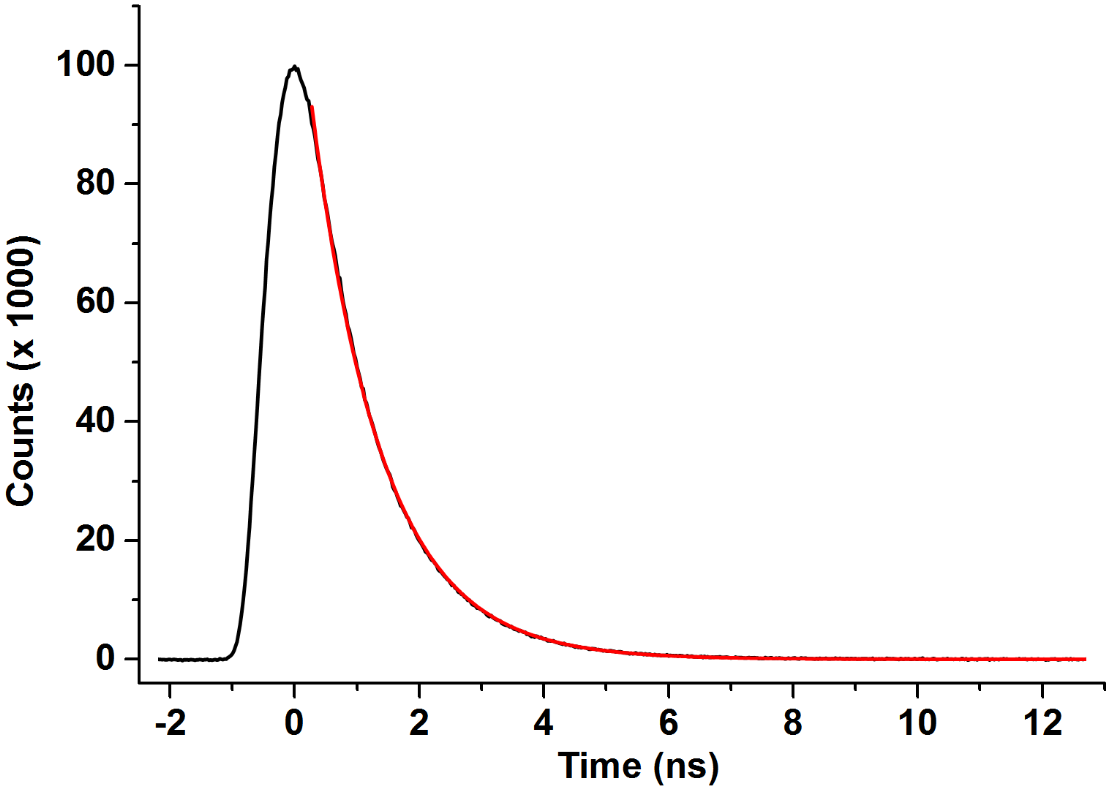

Figure S27. Time-resolved fluorescence intensity decay of **2**. The experimental data is depicted in black; the monoexponential fit of the data is shown in red.

Photooxidation of DHN to Juglone by $^1O_2$, as generated by 2

Detection of juglone

30 mg of 1,5-dihydroxynaphthalene (DHN) and 8 mg of **2** were dissolved in 20 mL of aerated solvent (DCM/MeOH 9:1). The solution was irradiated by LED light (λ_{exc} = 455 nm) for 3h. The solvents were removed under vacuum, and the products separated by column chromatography (ethyl acetate/hexane 2:1). The oxidation product, Juglone, was identified in the first fraction (R_f = 0.8), as determined by ^{1}H-NMR spectroscopy and gas chromatography (Retention time 8.435-8.447 min).

In the ^{1}H-NMR spectrum the product shows the same signals as a reference spectrum of commercially received Juglone: ^{1}H NMR (400 MHz, $CDCl_3$): δ 11.90 (s, 1H), 7.86 – 7.61(m, 2H), 7.29 (dd, ^4J = 2.1 Hz, ^3J = 7.2 Hz, 2H), 6.95 (s, 1H).

Spectral evolution during photooxidation

1 mL of a stock solution of DHN, dissolved in aerated DCM/MeOH 9:1 (330 µM), was mixed in a cuvette with 0.1 of the stock solution of **2** (same solvent, 330 µM), followed by 0.9 mL of pure solvent. The sample was irradiated by LED light (λ_{exc} = 455 nm) and an absorption spectrum was measured every 5 minutes. The spectra are shown in Figure S28. The reaction yield was determined as 10% after 45 minutes irradiation based on the extinction coefficient of juglone at 427 nm (ε = 3811 M^{-1} cm^{-1}).[18] No change in the absorption spectrum is observed in the absence of catalyst. The absorption spectrum of **2** only (no DHN) after 2 h irradiation is shown in Figure S29.

The analogous procedure was carried out for solutions of **1**. However, using the Ni complex, DHN oxidation was not observed (Figure S30).

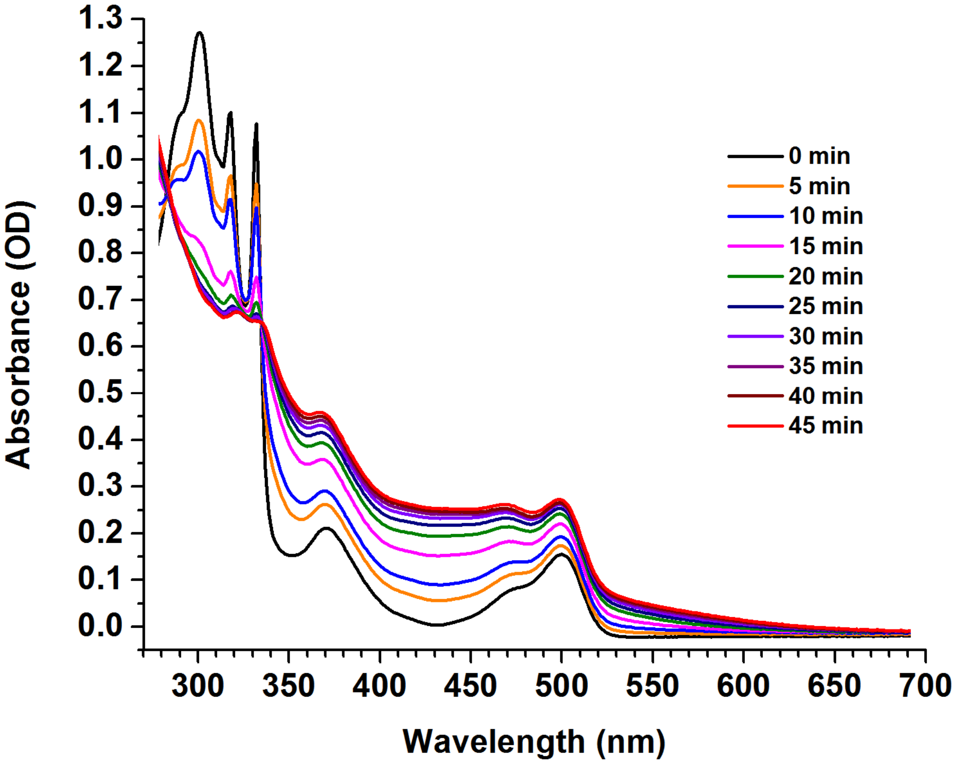

Figure S28. Spectral evolution of the absorption spectra during oxidation of DHN to Juglone in the presence of 10 mol% of **2**, in aerated DCM:MeOH (9:1); (λ_{exc} = 455 nm).

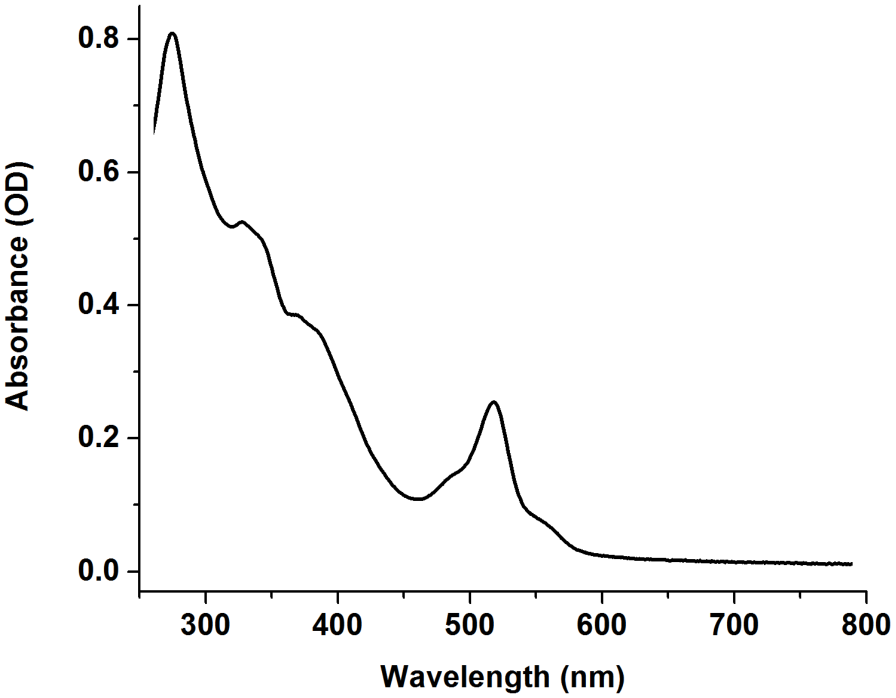

Figure S29. Final spectrum of **2** after 2 h irradiation (λ_{exc} = 455 nm; aerated DCM), in the absence of DHN. The spectrum indicates that a modified form of the complex results from the reaction of **2** with O_2 over longer times, in the absence of substrate.

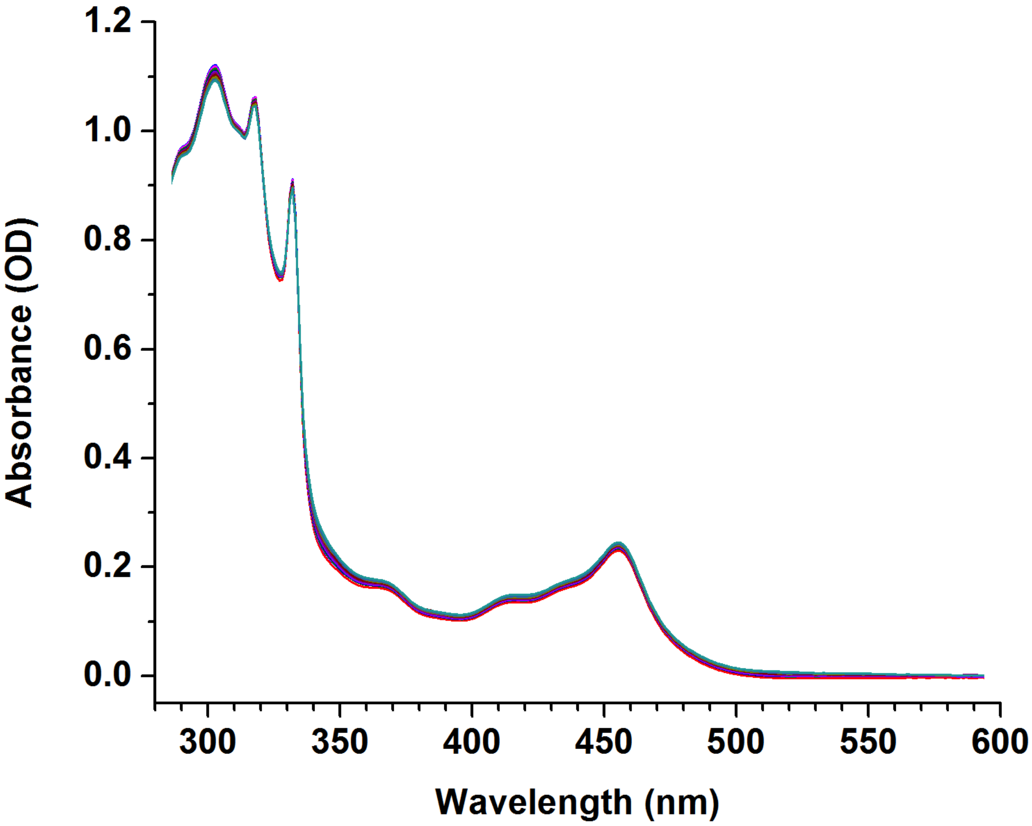

Figure S30. Monitoring of the absorbance spectrum of an aerated solution of 10 mol% **1** and DHN over a period of 50 minutes; DCM:MeOH (9:1); λ_{exc} = 455 nm.

Femtosecond Broadband Transient Absorption Measurements

Data acquisition: The femtosecond broadband transient absorption measurements of **1** and **2** were carried out using a setup that has been described in detail.[19, 20] Therefore, the experiment is only described briefly in the following.

The transient absorption setup is based on a Ti:sapphire amplifier (CPA 2001, Clark MXR) with 1 kHz repetition rate, wherein the output pulses have a center wavelength of about 778 nm. These pulses are frequency converted in a noncollinear optical parametric amplifier (NOPA) to obtain the 460 or 493 nm pump pulses.[21, 22] The pulse duration was 70 fs at the sample. In the measurement of **1** shown in Figure S35 the excitation pulse energy focused into the sample was 200 nJ and the spot had a FWHM of about 150 µm assuming a Gaussian beam profile. For the experiments on **2** the pump pulse wavelength was 493 nm with a pulse energy at the sample of 175 nJ. The pulse duration was 49 fs and the pump focus 105 µm.

For longer delay times than 2 ns the Ti:sapphire system is electronically synchronized with a wavelength tunable ns light source at 1 kHz (NT242 SHG/SFG; EKSPLA uab).[19, 20] Using the ns pulse to pump the sample, delay times up to 700 µs can be achieved with an instrumental response function of 2.5 ns. The timing jitter is less than <200 ps. The ns pulses (450 nm, 300 nJ for experiments on **1** and 493 nm, 232 nJ for experiments on **2**) were focused to a 150 µm FWHM spot.

For the probe beam a supercontinuum ranging from 285 to 720 nm was generated in a CaF_2 crystal. It was focused to a 40 µm FWHM spot and used to probe the temporal evolution of the sample. The relative polarization of pump and probe beam was set to the magic angle.

The sample were 10 mL solutions of **1** or **2** in a 50:50 THF:MeCN mixture (volume) with concentrations as given in the figure captions. For the measurements the sample was pumped through a flow circuit having no-Ox tubing and an integrated degasser (Knauer Online Degasser) for continuously removing oxygen from the solution to reach a reduced stationary oxygen concentration about 20 times smaller than ambient oxygen concentration. The sample was measured in a flow cell with 200 µm fused silica windows with an optical path length through the sample of 250 or 100 µm. The sample optical density was about 0.5 at the excitation wavelengths.

At first, one measurement of **1** with ambient oxygen concentration (degasser was switched off) was recorded prior to continuously degassing the solution for the second measurement. The measurement with ambient oxygen concentration is shown below in Figure S31. After 3 h of degassing the second measurement (shown in Figure S33 and Figure S35) was recorded with the same experimental parameters. For **2**, only measurements with a degassed sample were made.

Data analysis: each time dependent set of TA spectra was analyzed in two ways: singular value decomposition (SVD) followed by global-fit to a sum-of-exponentials model, as well as a model-neutral Maximum Entropy Analysis (MEA). In the first case, we performed a SVD decomposition of the TA data in order to determine the number of unique time-constants to be used in the kinetic modelling. This number of components was used in a global sum-of-exponential-components fit to the data. The global fit routine simultaneously fits the kinetics at each detection wavelength to the chosen number of components, each being defined by an amplitude and a time-constant (“lifetime”), using the constraint of global time-constants. We display the amplitudes emerging from these fits in terms of the “sequential relaxation model”, where the dynamics are analyzed in terms of a compartmental model. Here, the population is assumed to be initially placed in one “compartment”, and transfer dynamics is strictly sequential between the compartments in the model - before return to the ground-state. The time-constants extracted from the global fit correspond to transfer-times between compartments, and we can extract the spectra associated with each “compartment”: the evolution associated decay spectra (EAS).[23] In the limit where the dynamics of the physical system in fact follows strict one-way level-to-level transfer (without e.g. branching or other complications in the relaxation pathway), the EAS corresponds directly to the spectra of the individual states. This is not the case in general, and one must rather consider these as effective spectra associated with certain time-scales. We evaluate the goodness-of-fit by the root-mean-square error and by visual inspection of the residuals. For this purpose, the Glotaran package (by van Stokkum et al [ref23]) was used.

Secondly, a Maxim Entropy Analysis was performed using the software of own design created by the developers of the method as described in reference [24].[24] This renders an unbiased display of the probability density that a certain decay constant is present in the data set. The spectral dependences of the probability are similar in information to the DAS spectra of a global analysis. A positive signal is due to a decrease of excited state absorption, a negative a decrease of ground state bleach or stimulated emission.

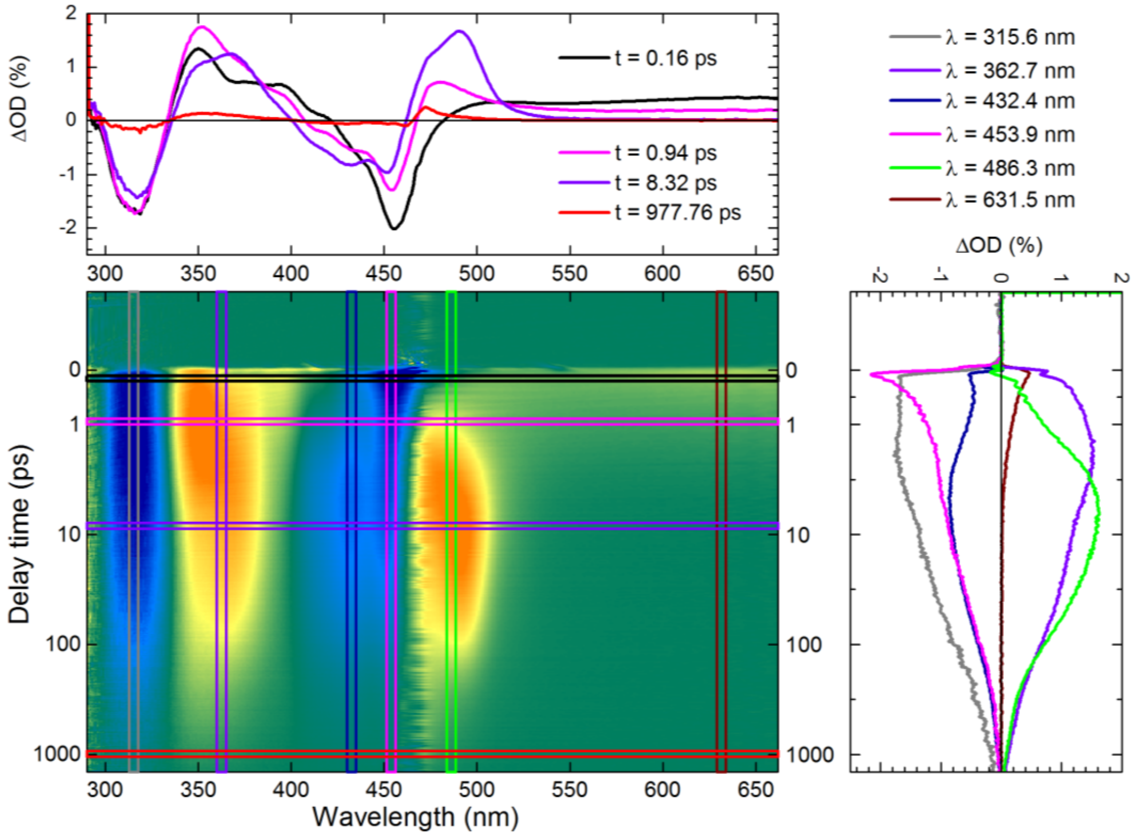

Figure S31. Transient absorption data of a non-degassed 1mM solution of **1** in 1:1 THF/MeCN measured in a 250 μm thick flow cell after excitation with ~70 fs pulses centered at 460 nm having a pulse energy of 200 nJ.

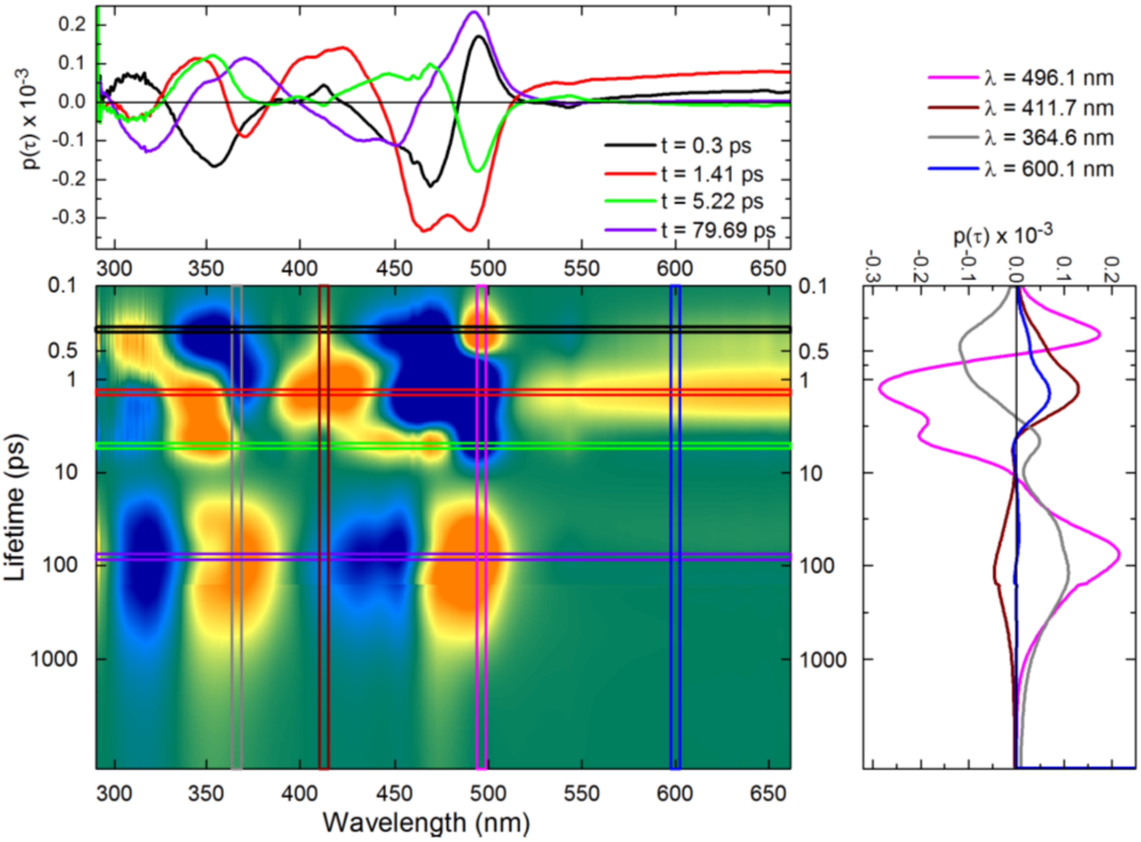

Figure S32. Maximum entropy analysis of the data set in Fig. S31.

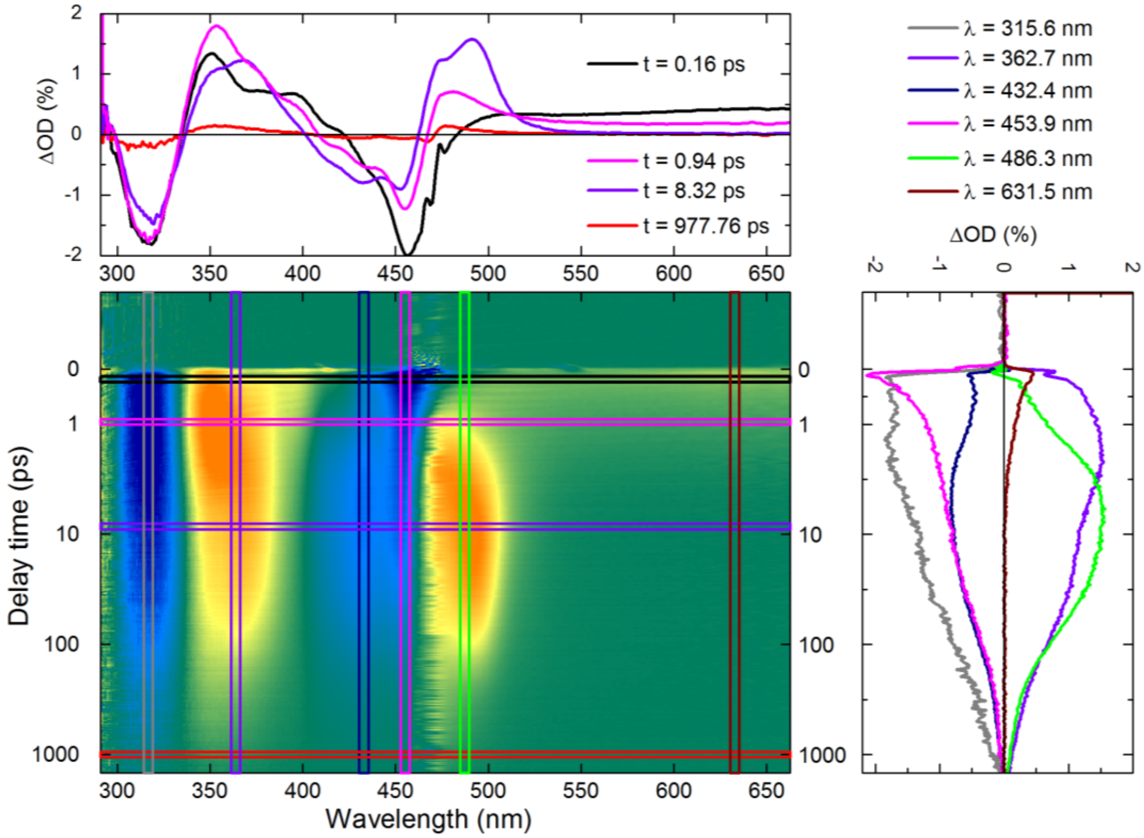

Figure S33. Transient absorption data of a degassed 1 mM solution of **1** in 1:1 THF/MeCN measured in a 250 μm thick flow cell after excitation with ~70 fs pulses centered at 460 nm having a pulse energy of 200 nJ.

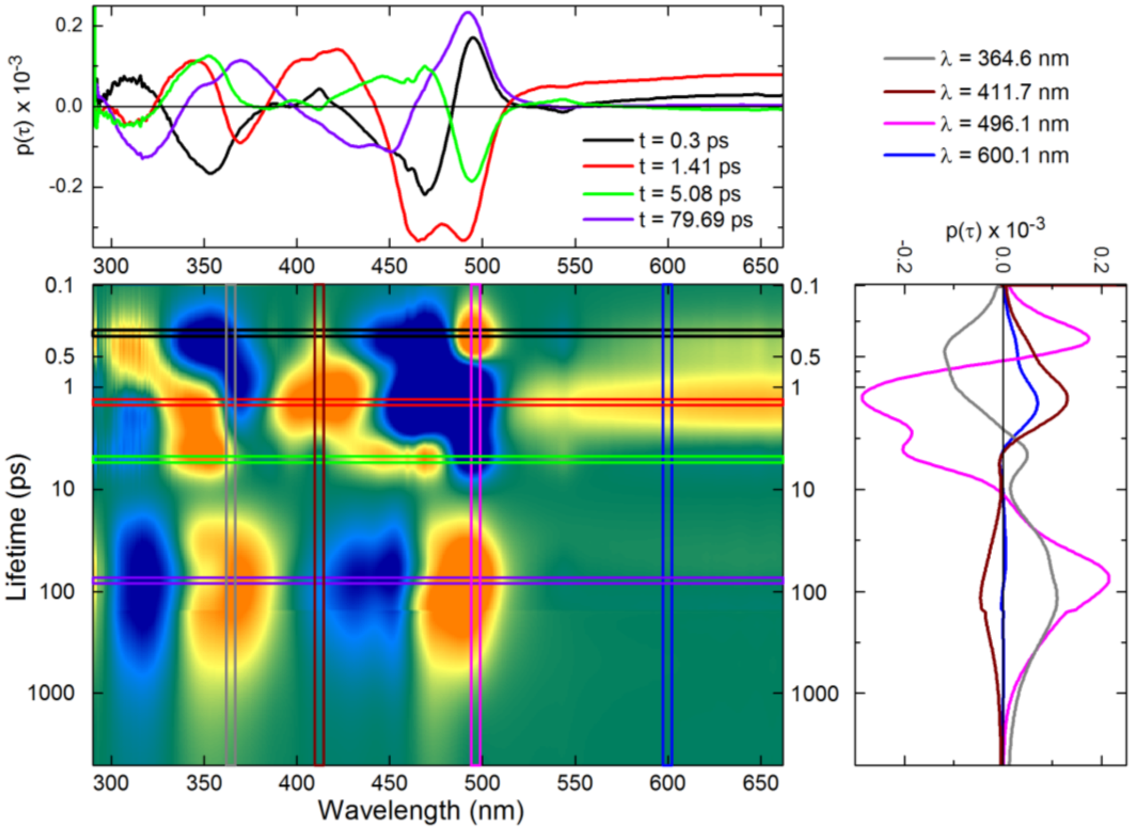

Figure S34. Maximum entropy analysis of the fs/ps data set for **1** in Fig. S33.

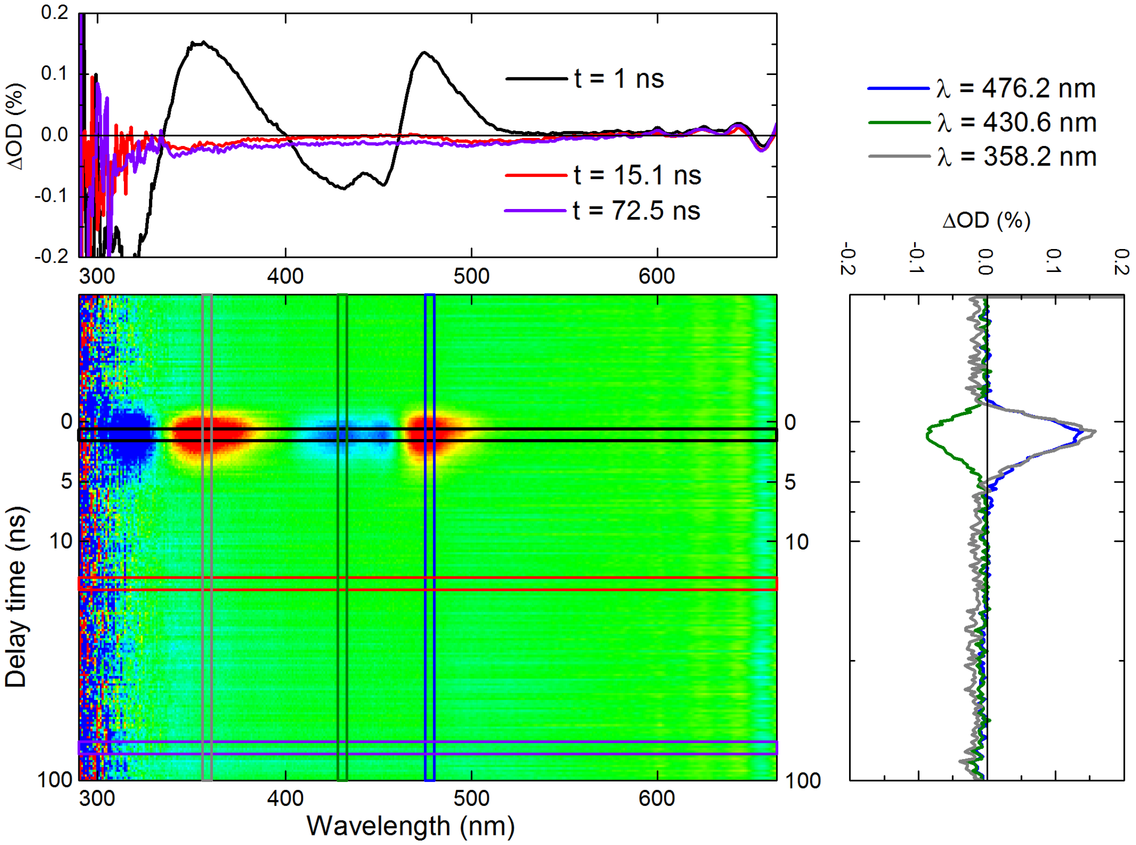

Figure S35. Transient absorption spectra of **1** in degassed 1:1 MeCN:THF; 2.5 ns excitation pulse, 300 nJ pulse energy, 450 nm excitation wavelength.

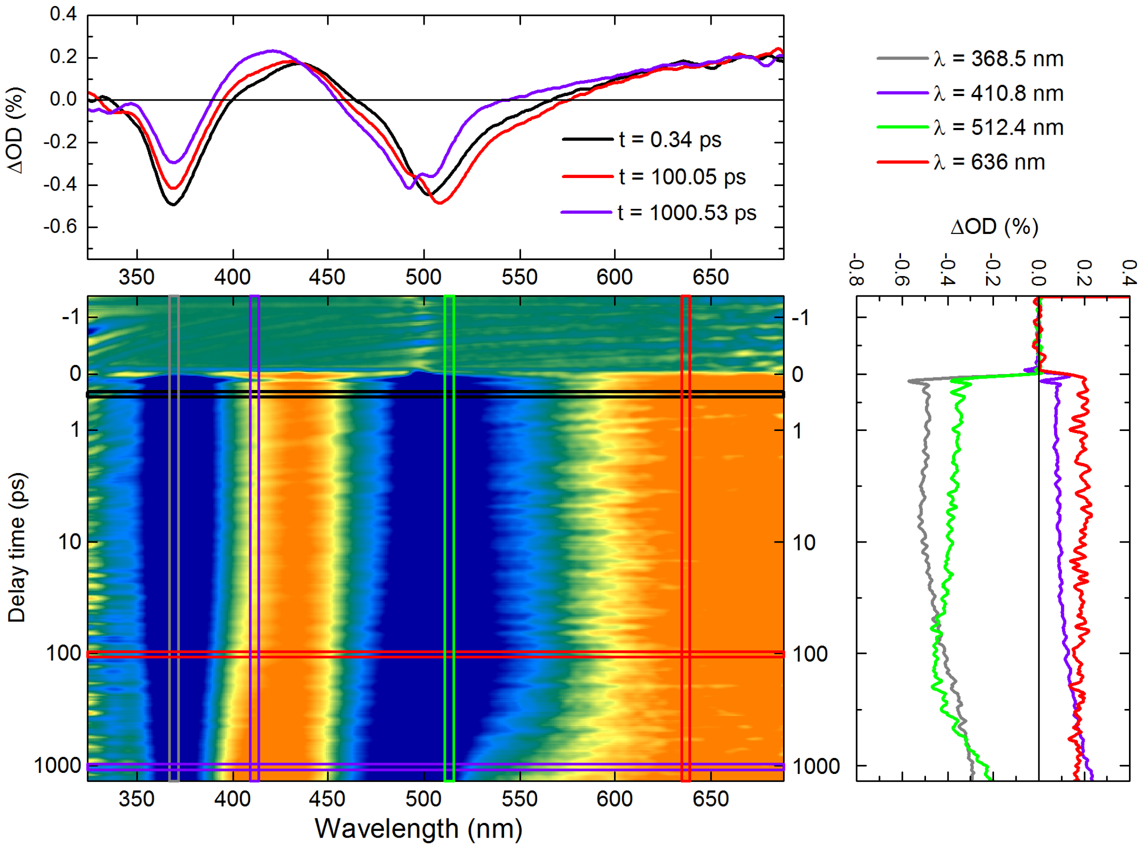

Figure S36. Transient absorption data of a degassed 0.34 mM solution of **2** in 1:1 THF/MeCN measured in a 100 μm thick flow cell after excitation with 49 fs pulses centered at 493 nm having a pulse energy of 175 nJ.

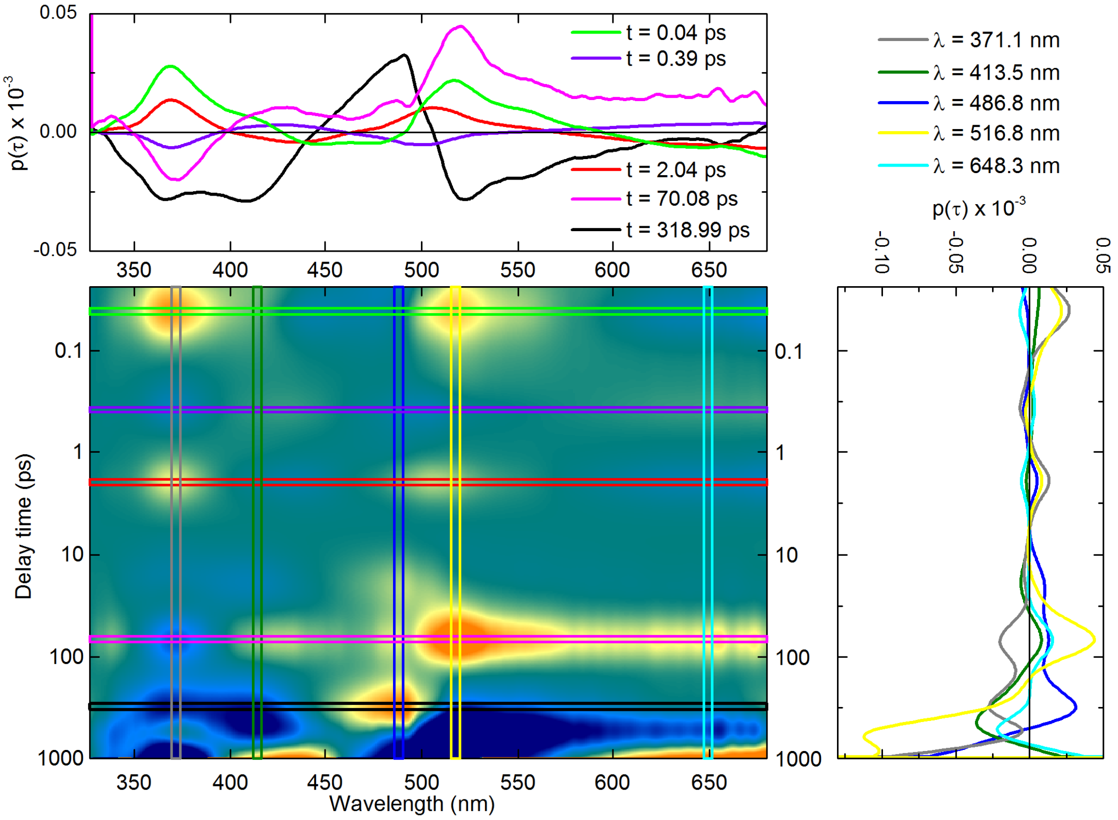

Figure S37. Maximum entropy analysis of the fs/ps data set for **2** in Figure S36.

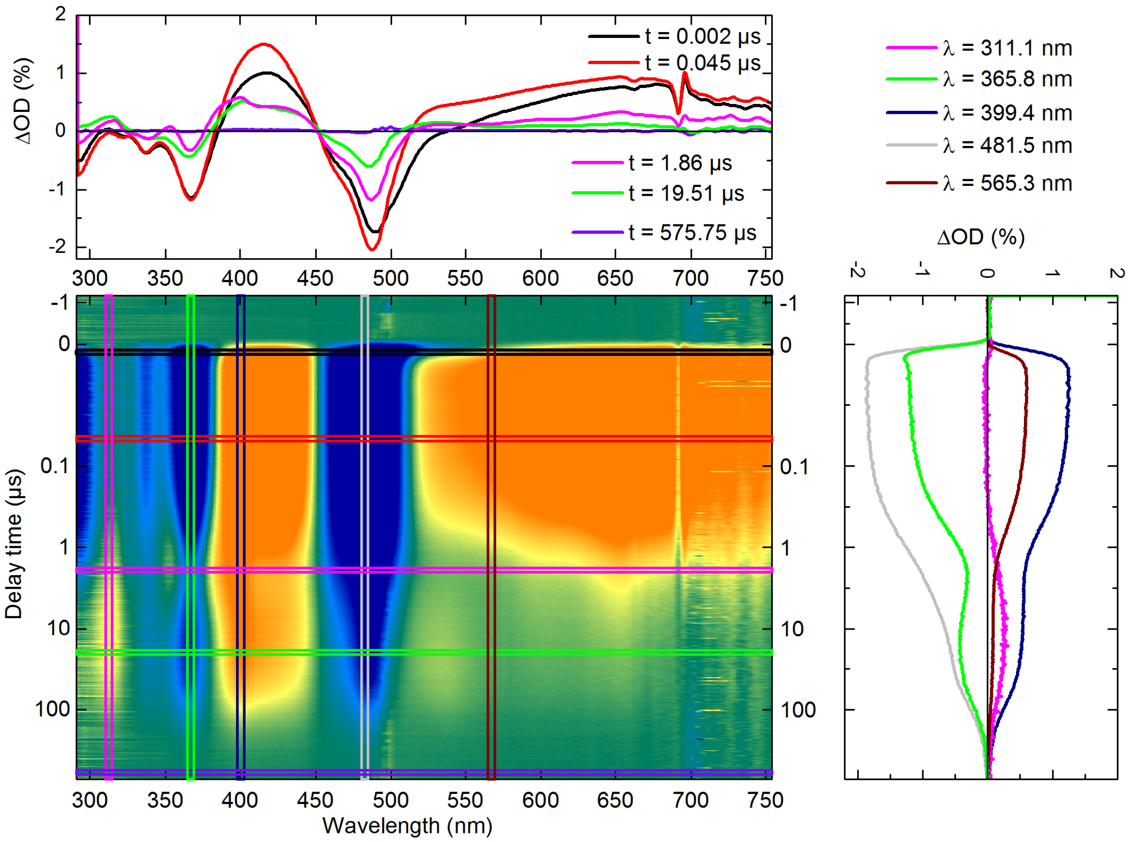

Figure S38. Transient absorption data of a degassed 0.4 mM solution of **2** in 1:1 THF/MeCN measured in a 100 µm thick flow cell after excitation with 2.5 ns pulses centered at 493 nm having a pulse energy of 232 nJ.

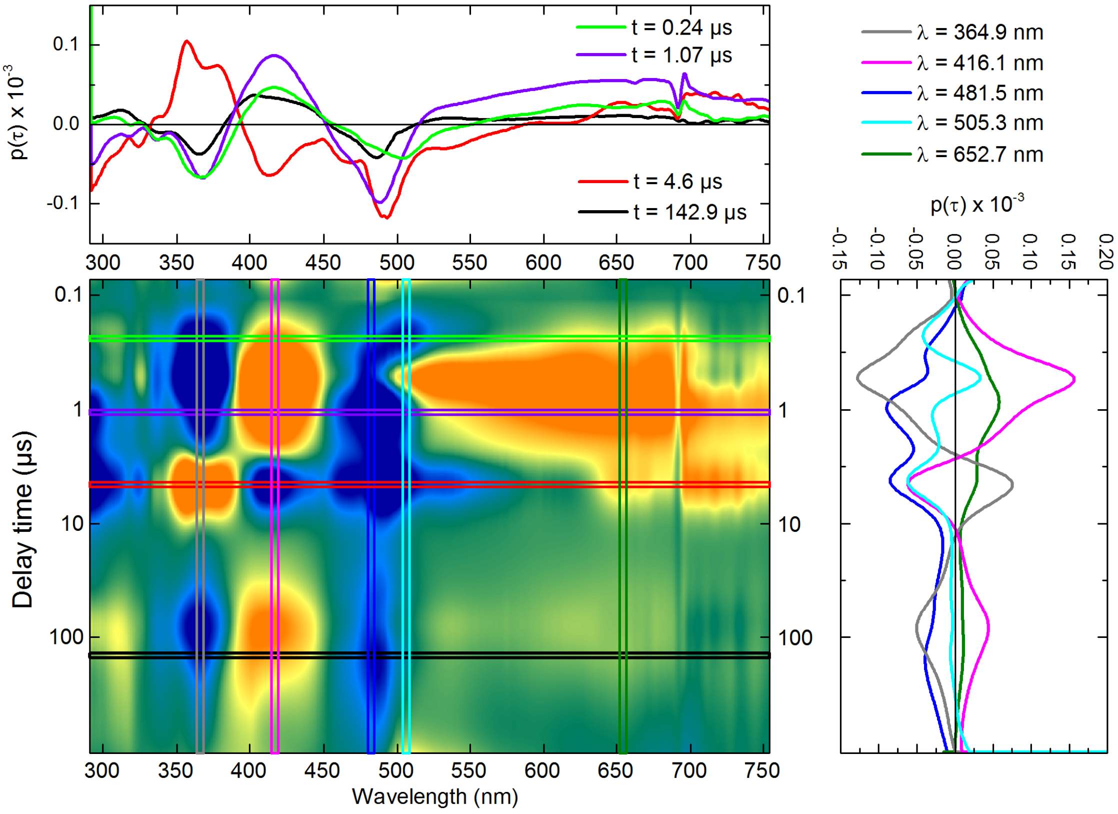

Figure S39. Maximum entropy analysis of the ns/µs data set for **2** in Figure S38.

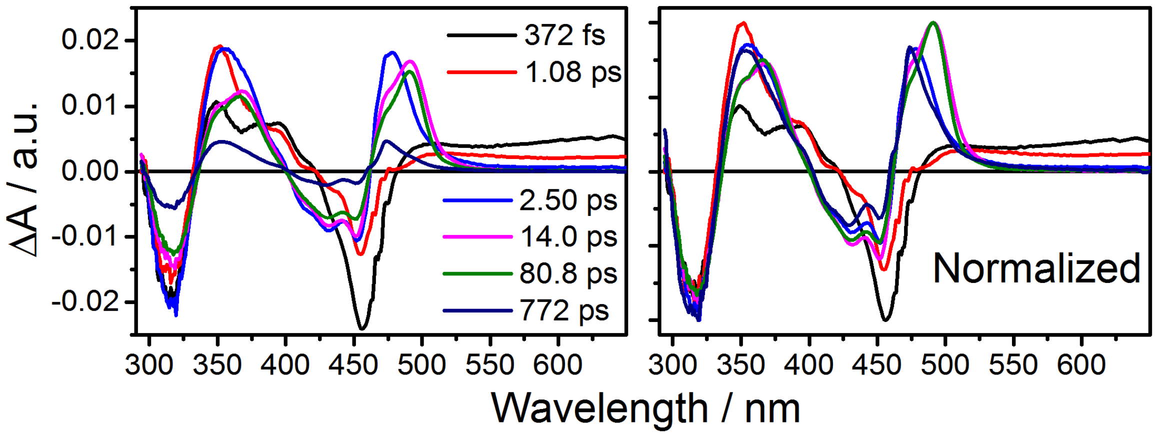

Figure S40. Global analysis of the fs transient absorption data of **1** as shown in Figure 3 of the manuscript and Figure S33 above. Left panel: EAS spectra shown on "absolute scale"; Right panel: normalized spectra.

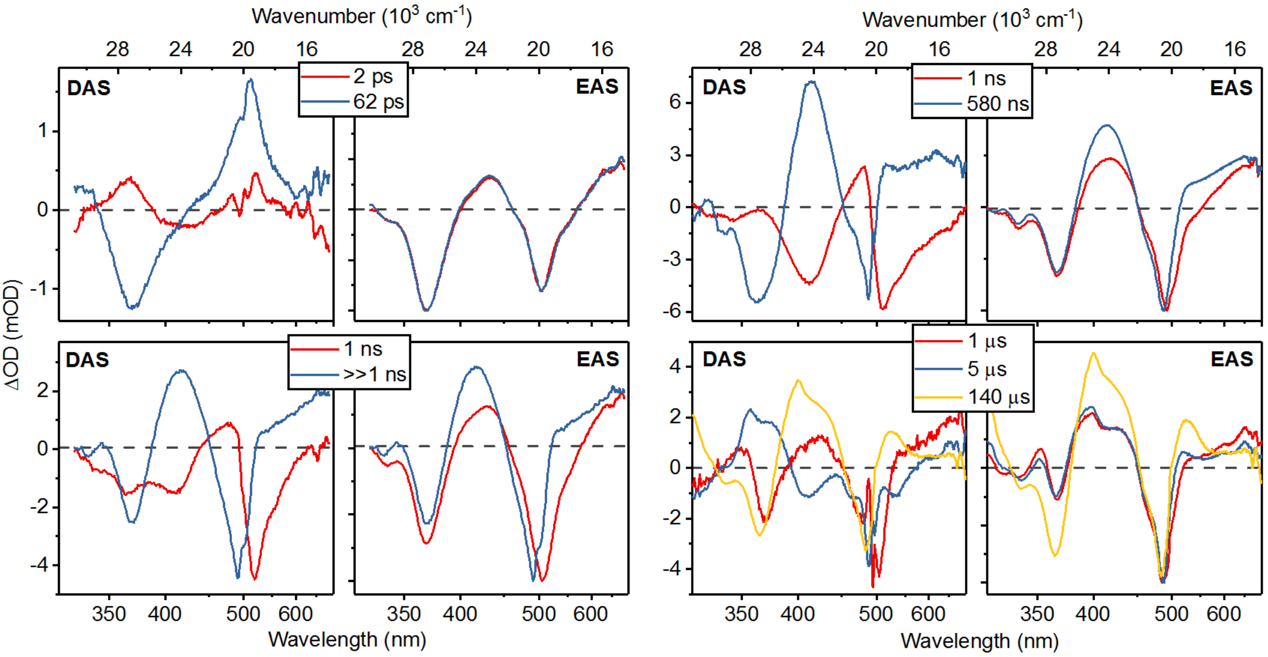

Figure S41a. Decay associated- (DAS) and evolutionary associated- (EAS) decay spectra extracted from a global fit of the relaxation dynamics of **2**. DAS amplitudes are shown on absolute scale, while the EAS are normalized to their maximum for easier comparison of spectral shapes. The data shown in Figure S36 were used for analysis of fast timescales, while the data shown in Figure S38 were used for analysis of slow processes.

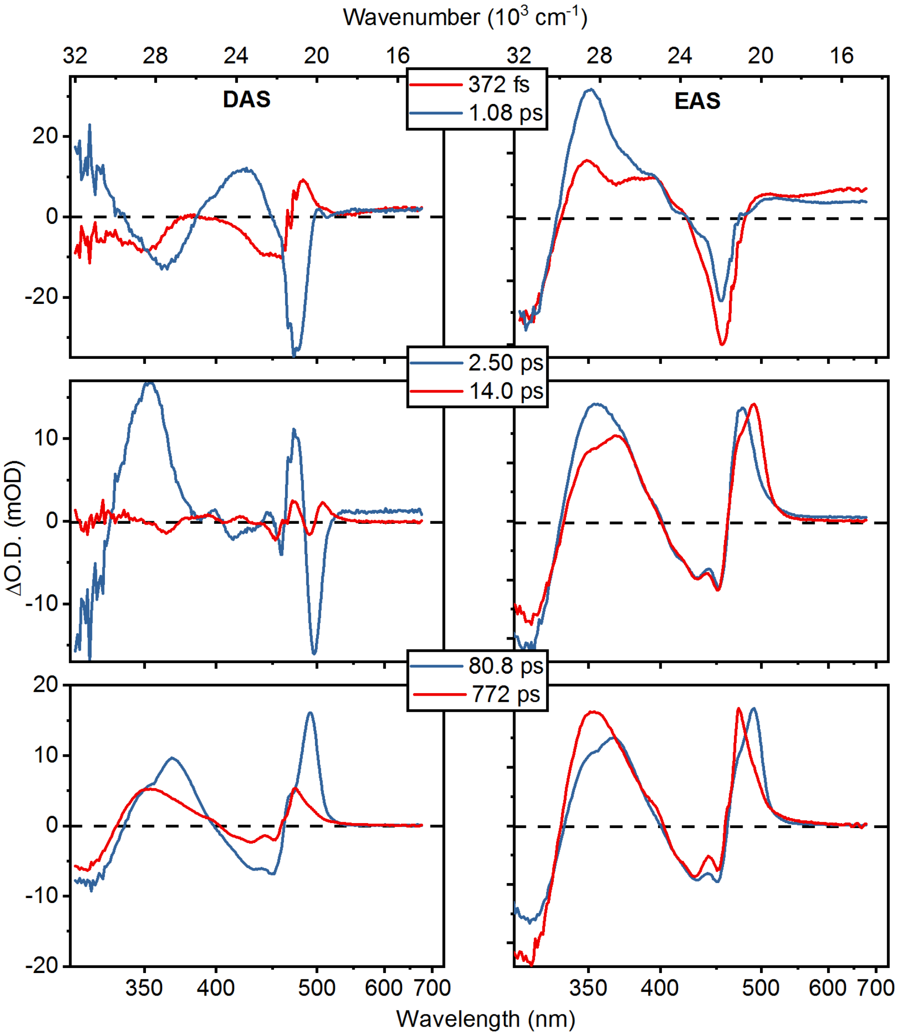

Figure S41b. DAS (left) and EAS (right) extracted from the relaxation dynamics of **1.** DAS shown on absolute scale, while the EAS are normalized to their maximum. The presented data are identical to those in Figure 4 of the main text, but here organized in in order of increasing time constant.

Quantum Chemical Calculations

[Ni^{II}(Mabiq)]$^+$ and [Zn^{II}(Mabiq)]$^+$ were investigated computationally, starting from the molecular structures of **1** and **2**, respectively. The coordinating triflate molecule found in the molecular structure of **2** was removed for the purpose of the DFT calculations. Geometry optimizations were performed employing density functional theory using the dispersion-corrected B3LYP-D3 functional and def2-SVP (C, O, N, H) and def2-TZVP (Zn, Ni) basis sets.[25-27] Electronic energies of the optimized structures were calculated with singlet and triplet configuration using def2-TZVP basis sets for all atoms. Vertical excitation energies were computed at the TDDFT level using both B3LYP, CAM-B3LYP functionals as well as using ADC(2),[28-30] and def2-TZVP basis sets for all atoms.[31] TURBOMOLE v. 6.6-7.2 was used for B3LYP and ADC(2) calculations, while calculations with the CAM-B3LYP functional were performed with Q-Chem v. 5.2.[32, 33] VMD was used for visualization purposes.[34] Spin–orbit coupling (SOC) was estimated at the B3LYP/def2-TZVP level, as implemented in ORCA (v. 4.2.0).[35, 36]

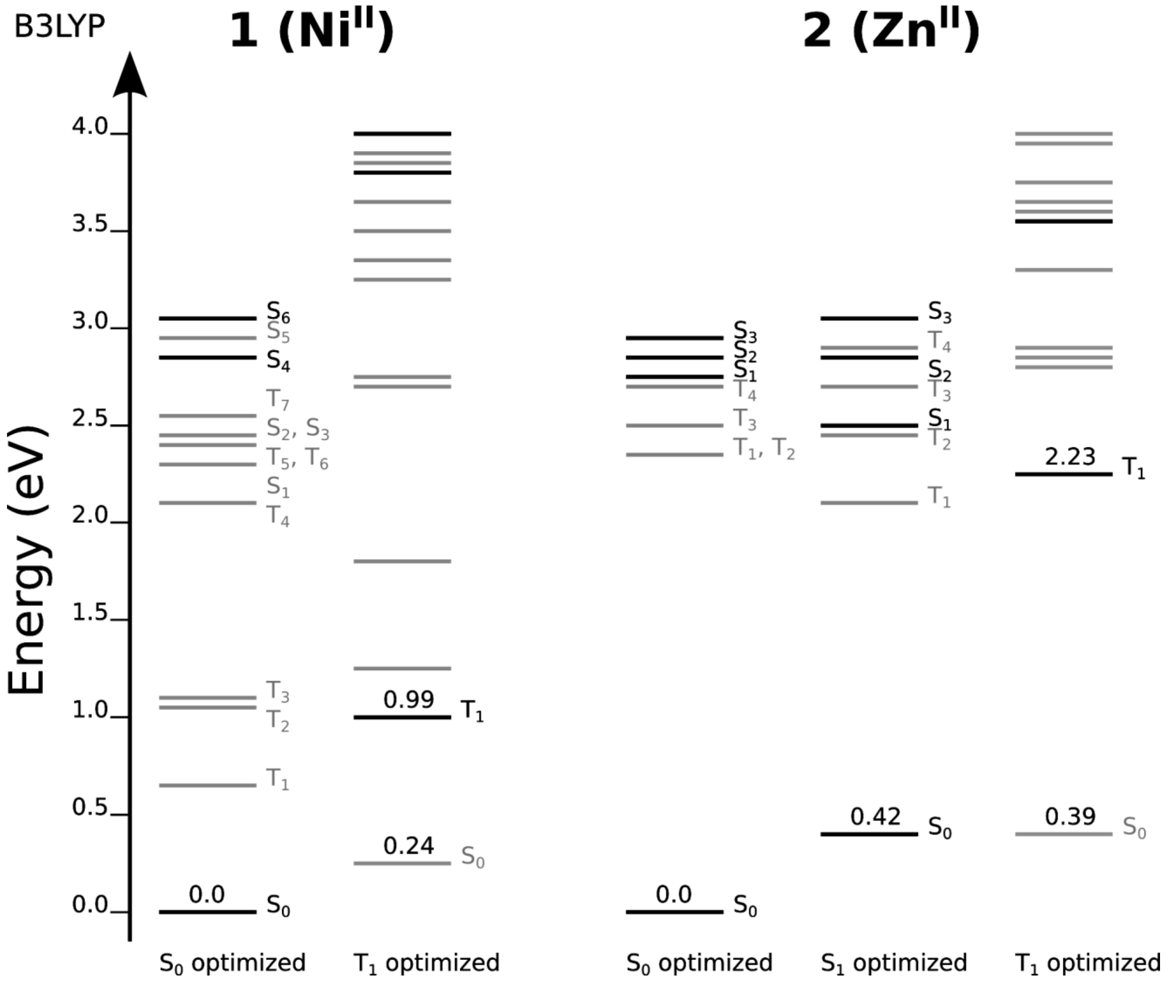

Figure S42. Vertical excitation energies of **1** ([Ni^{II}(Mabiq)]$^+$) and **2** ([Zn^{II}(Mabiq)]$^+$) calculated at the B3LYP level from the optimized geometries of the singlet ground state (S$_0$), the first excited singlet state (S$_1$), and the lowest energy triplet state (T$_1$). Gray lines indicate optically dark excited states.

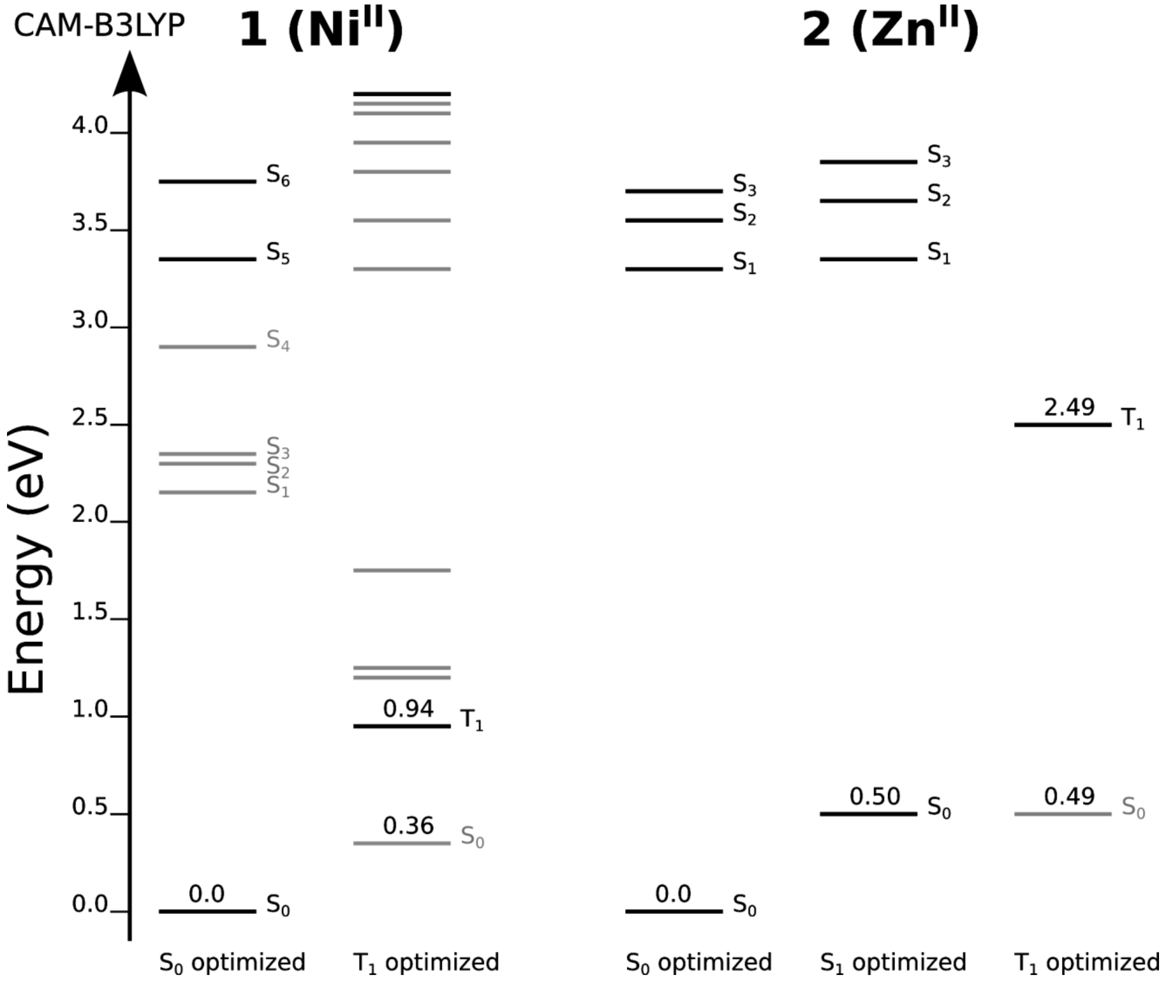

Figure S43. Vertical excitation energies of **1** ([Ni^{II}(Mabiq)]$^+$) and **2** ([Zn^{II}(Mabiq)]$^+$) calculated with the CAM-B3LYP functional from the B3LYP optimized geometries of the singlet ground state (S_0), the first excited singlet state (S_1), and the lowest energy triplet state (T_1). Gray lines indicate optically dark excited singlet states.

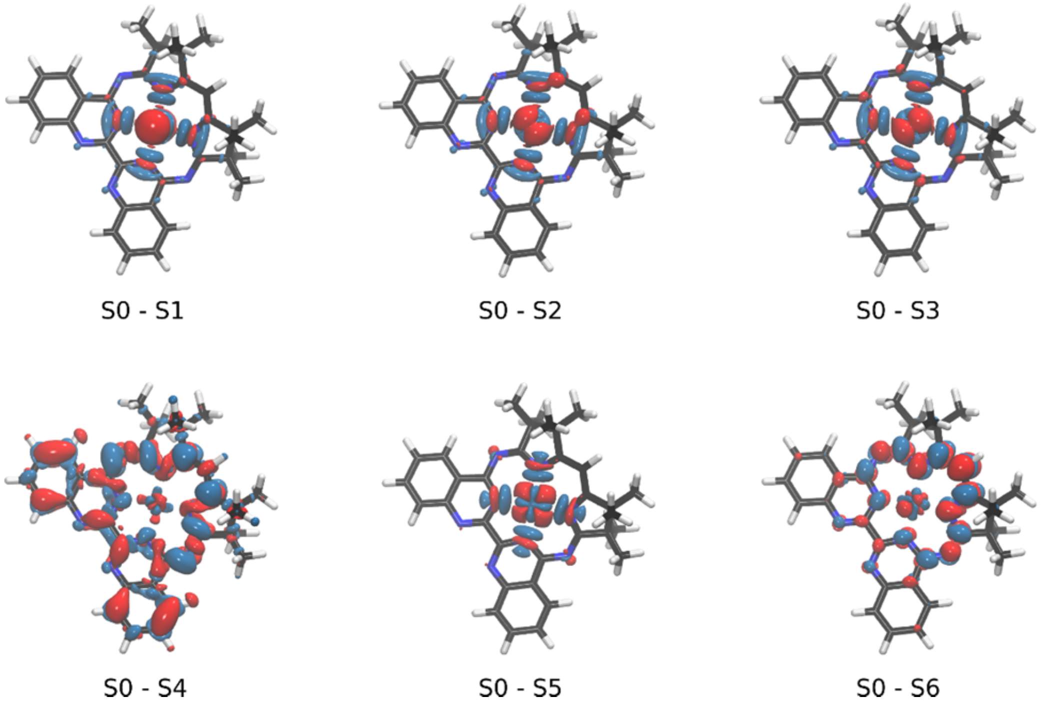

S0 - S1 S0 - S2 S0 - S3

S0 - S4 S0 - S5 S0 - S6

Figure S44. Density difference plots upon photoexcitation from the optimized S_0 ground state to excited singlet states of **1**.

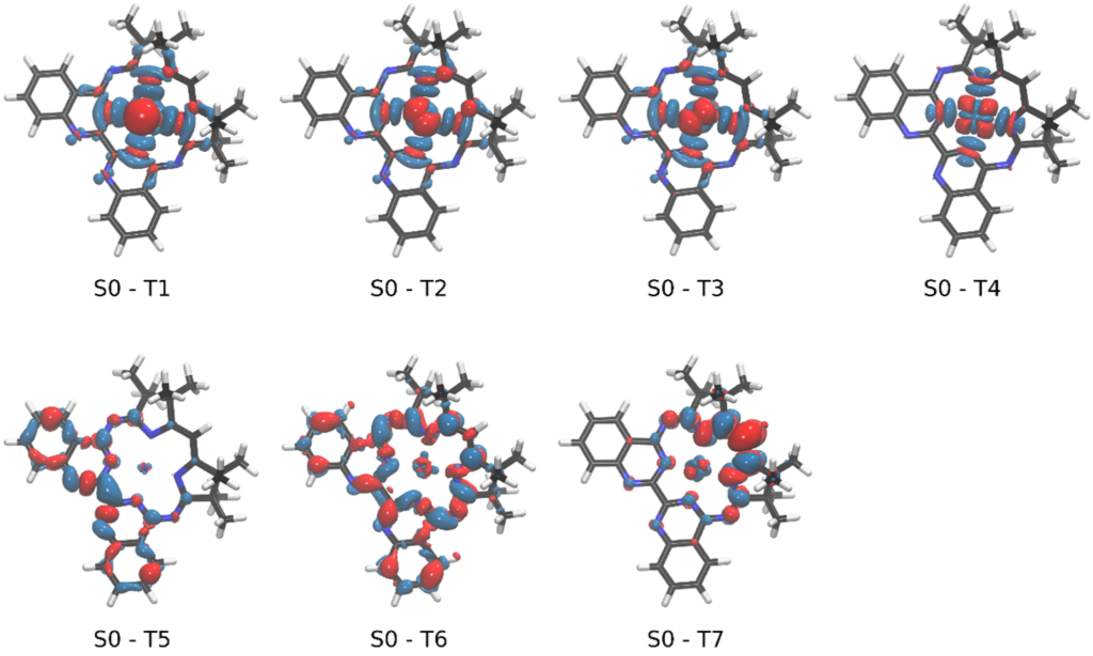

S0 - T1 S0 - T2 S0 - T3 S0 - T4

S0 - T5 S0 - T6 S0 - T7

Figure S45. Density difference plots upon photoexcitation from the optimized S_0 ground state to excited triplet states of **1**.

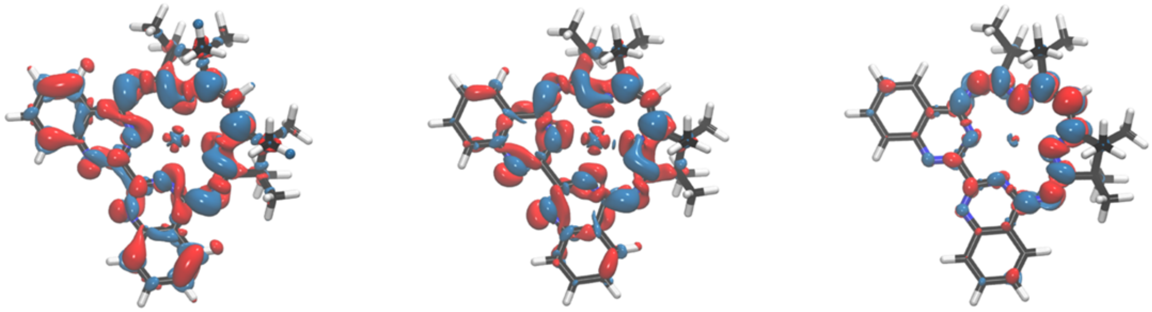

S0 - S1 S0 - S2 S0 - S3

Figure S46. Density difference plots upon photoexcitation from the optimized S_0 ground state to excited singlet states of **2**.

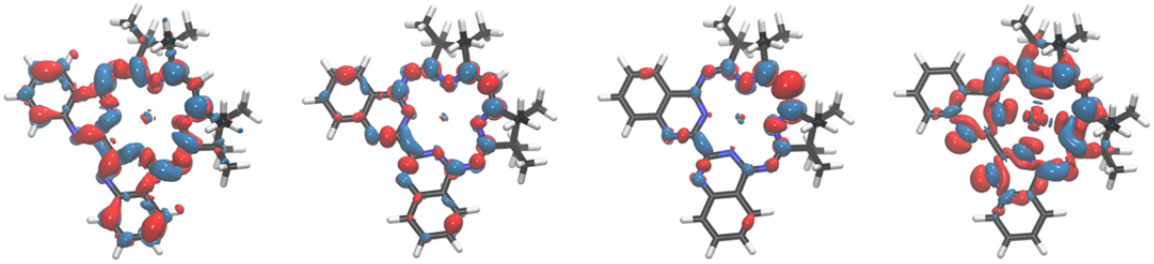

S0 - T1 S0 - T2 S0 - T3 S0 - T4

Figure S47. Density difference plots upon photoexcitation from the optimized S_0 ground state to excited triplet states of **2**.

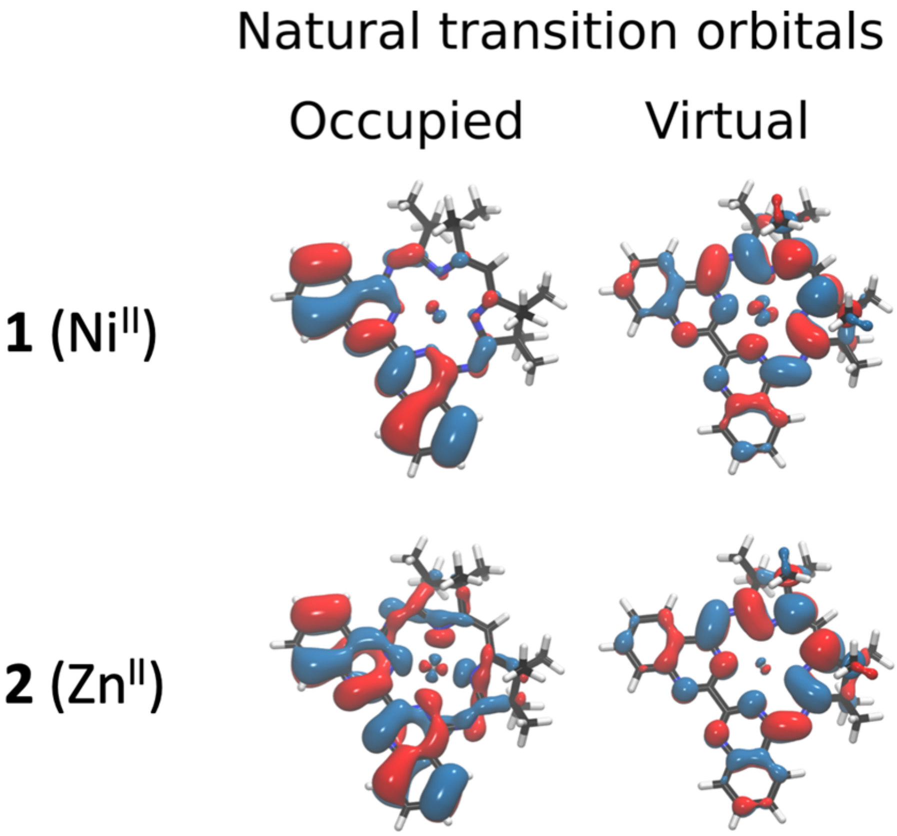

Figure S48. Natural transition orbitals (NTOs) for the excitations from the ground state singlet S_0 to the lowest energy optically bright state of **1** (top; $S_0 \rightarrow S_4$) and **2** (bottom; $S_0 \rightarrow S_1$).

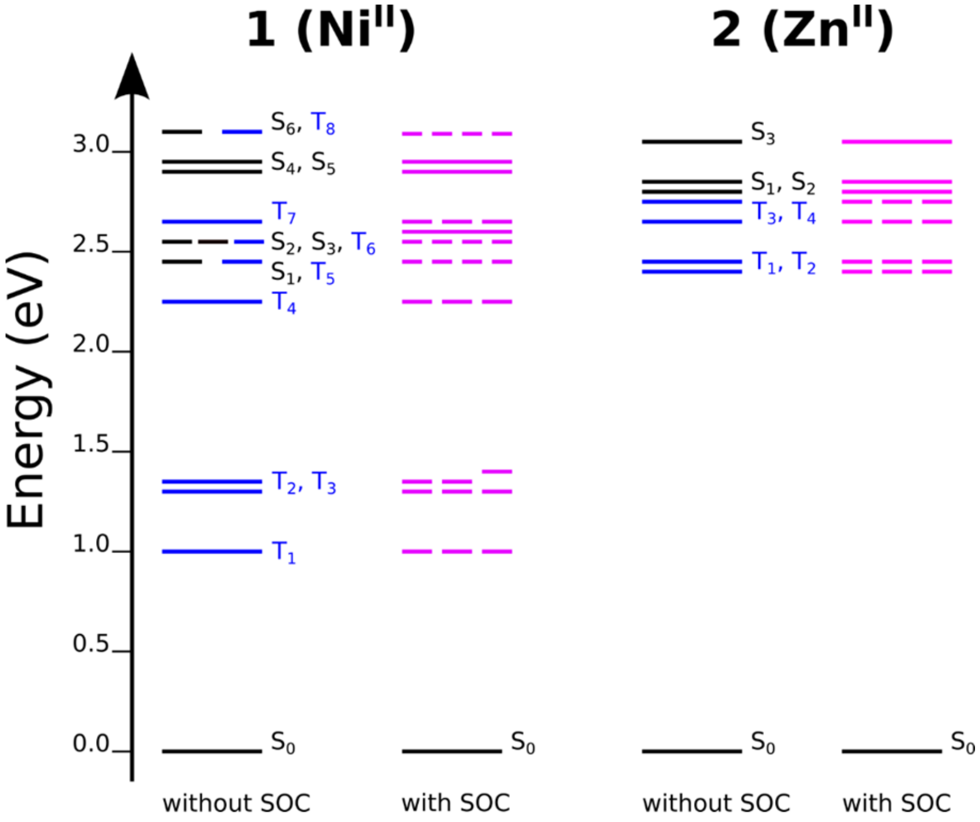

Figure S49. Spin-orbit coupling effects in [Ni-Mabiq]$^+$ and [Zn-Mabiq]$^+$. Singlet and triplet excited states are indicated by black (singlet) and blue (triplet) lines/dashes, while the spin-orbit coupled excited states are indicated by purple lines/dashes.

Table S1. TDDFT excitation energies of **1** (Ni^{II}) and **2** (Zn^{II}) calculated at the B3LYP level from the optimized geometries of the singlet ground state (S_0), the first excited singlet state (S_1), and the lowest energy triplet state (T_1).

Optimized geometry	**Type of excitations**		**Excitation energy (eV)**	**Oscillator strength**
[Ni^{II}(Mabiq)]$^+$ S_0	Singlet excitations from S_0	$S_0 \rightarrow S_1$	2.28	0.00
		$S_0 \rightarrow S_2$	2.42	0.00
		$S_0 \rightarrow S_3$	2.46	0.00
		$S_0 \rightarrow S_4$	**2.85**	0.10
		$S_0 \rightarrow S_5$	2.95	0.00
		$S_0 \rightarrow S_6$	3.03	0.11
	Triplet excitations from S_0	$S_0 \rightarrow T_1$	0.67	0.00
		$S_0 \rightarrow T_2$	1.05	0.00
		$S_0 \rightarrow T_3$	1.11	0.00
		$S_0 \rightarrow T_4$	2.08	0.00
		$S_0 \rightarrow T_5$	2.37	0.00
		$S_0 \rightarrow T_6$	2.38	0.00
		$S_0 \rightarrow T_7$	2.56	0.00
[Ni^{II}(Mabiq)]$^+$ T_1	Excitations from T_1	*transition number*		
		1	0.24	0.00
		2	0.28	0.00
		3	0.80	0.00
		4	1.70	0.00
		5	1.75	0.00
		6	2.24	0.00
		7	2.36	0.00
		8	2.36	0.00
		9	2.38	0.00
		10	2.50	0.00
		11	2.51	0.00
		12	2.66	0.00
		13	2.66	0.00
		14	2.81	0.00
		15	2.82	0.10
		16	2.86	0.00
		17	2.89	0.00
		18	2.99	0.13

Table S1 (contd). TDDFT excitation energies of **1** (Ni^{II}) and **2** (Zn^{II}) calculated at the B3LYP level from the optimized geometries of the singlet ground state (S_0), the first excited singlet state (S_1), and the lowest energy triplet state (T_1).

$[Zn^{II}(Mabiq)]^+$ S_0	Singlet excitations from S_0	$S_0 \rightarrow S_1$	**2.77**	0.08
		$S_0 \rightarrow S_2$	2.86	0.02
		$S_0 \rightarrow S_3$	2.97	0.13
	Triplet excitations from S_0	$S_0 \rightarrow T_1$	2.33	0.00
		$S_0 \rightarrow T_2$	2.34	0.00
		$S_0 \rightarrow T_3$	2.50	0.00
		$S_0 \rightarrow T_4$	2.72	0.00
$[Zn^{II}(Mabiq)]^+$ S_1		*transition number*		
	Singlet excitations from S_0	1	2.06	0.09
		2	2.45	0.03
		3	2.64	0.03
	Triplet excitations from S_0	1	1.69	0.00
		2	2.05	0.00
		3	2.28	0.00
		4	2.46	0.00
$[Zn^{II}(Mabiq)]^+$ T_1		*transition number*		
	Excitations from T_1	1	0.55	0.01
		2	0.62	0.00
		3	0.67	0.02
		4	1.09	0.04
		5	1.32	0.08
		6	1.36	0.03
		7	1.41	0.00
		8	1.50	0.00
		9	1.74	0.02
		10	1.78	0.01

Table S2. Characters of transitions from TDDFT/B3LYP calculations of **1** (Ni^{II}) and **2** (Zn^{II}).

Excitations		**Character**
Singlet excitations from $[Ni^{II}(Mabiq)]^+$ S_0	$S_0 \rightarrow S_1$	d-d ($z^2 \rightarrow x^2-y^2$)
	$S_0 \rightarrow S_2$	d-d ($xz \rightarrow x^2-y^2$)
	$S_0 \rightarrow S_3$	d-d ($yz \rightarrow x^2-y^2$)
	$S_0 \rightarrow S_4$	ligand π-π*
	$S_0 \rightarrow S_5$	d-d ($xy \rightarrow x^2-y^2$)
	$S_0 \rightarrow S_6$	mixed
Triplet excitations from $[Ni^{II}(Mabiq)]^+$ S_0	$S_0 \rightarrow T_1$	d-d ($z^2 \rightarrow x^2-y^2$)
	$S_0 \rightarrow T_2$	d-d ($xz \rightarrow x^2-y^2$)
	$S_0 \rightarrow T_3$	d-d ($yz \rightarrow x^2-y^2$)
	$S_0 \rightarrow T_4$	d-d ($xy \rightarrow x^2-y^2$)
	$S_0 \rightarrow T_5$	ligand π-π*
	$S_0 \rightarrow T_6$	ligand π-π*
	$S_0 \rightarrow T_7$	mixed
Singlet excitations from $[Zn^{II}(Mabiq)]^+$ S_0	$S_0 \rightarrow S_1$	ligand π-π*
	$S_0 \rightarrow S_2$	ligand π-π*
	$S_0 \rightarrow S_3$	ligand π-π*
Triplet excitations from $[Zn^{II}(Mabiq)]^+$ S_0	$S_0 \rightarrow T_1$	ligand π-π*
	$S_0 \rightarrow T_2$	ligand π-π*
	$S_0 \rightarrow T_3$	ligand π-π*
	$S_0 \rightarrow T_4$	ligand π-π*

Table S3. TDDFT excitation energies of **1** (Ni^{II}) and **2** (Zn^{II}) calculated with the CAM-B3LYP functional at the B3LYP optimized geometries of the singlet ground state (S_0), first excited singlet state (S_1), and lowest energy triplet state (T_1).

Optimized geometry	**Type of excitations**	**Transition Number**	**Excitation energy (eV)**	**Oscillator strength**
$[Ni^{II}(Mabiq)]^+$ S_0	Singlet excitations from S_0	1	2.13	0.00
		2	2.32	0.00
		3	2.37	0.00
		4	2.92	0.00
		5	3.34	0.17
		6	3.75	0.37
$[Ni^{II}(Mabiq)]^+$ T_1	Excitations from T_1	1	0.26	0.00
		2	0.30	0.00
		3	0.79	0.00
		4	2.36	0.00
		5	2.59	0.00
		6	2.62	0.00
		7	2.63	0.00
		8	2.86	0.00
		9	2.99	0.00
		10	3.14	0.00
		11	3.23	0.00
		12	3.28	0.19
$[Zn^{II}(Mabiq)]^+$ S_0	Singlet excitations from S_0	1	3.28	0.22
		2	3.54	0.05
		3	3.70	0.33
$[Zn^{II}(Mabiq)]^+$ S_1	Singlet excitations from S_0	1	2.83	0.18
		2	3.13	0.23
		3	3.37	0.03

Table S4. Excitation energies of **1** (Ni^{II}) and **2** (Zn^{II}) calculated with the ADC(2)/TZVP level of the singlet ground state (S_0).

Optimized geometry	**Type of excitations**	**Transition Number**	**Excitation energy (eV)**	**Oscillator strength**
$[Ni^{II}(Mabiq)]^+$ S_0	Singlet excitations from S_0	1	2.30	0.00
		2	2.31	0.01
		3	2.38	0.00
		4	2.65	0.02
		5	**2.72**	0.19
		6	2.97	0.21
$[Zn^{II}(Mabiq)]^+$ S_0	Singlet excitations from S_0	1	2.63	0.004
		2	**2.70**	0.24
		3	3.05	0.24
$[Zn^{II}(Mabiq)]^+$ S_1	Singlet excitations from S_0	1	1.93	0.08
		2	2.26	0.07
		3	2.46	0.14

Table S5. Difference in atomic charges between the excited and ground states of the [Ni-Mabiq]$^+$ complex derived from a Mulliken population analysis at the TDDFT/B3LYP/def2-TZVP level. The charges of S_0, S_4, and S_6 were calculated at the optimized singlet (S_0) geometry. The charges of T_1, E_1, E_2, E_3, and E_4 were calculated at the optimized lowest energy triplet (T_1) geometry. E_1-E_4 denote the first four excitations from T_1 at the optimized T_1 geometry, *i.e.* the four lowest dashed lines in Fig. 5a.

	S_4-S_0	S_6-S_0	T_1-S_0	E_1-S_0	E_2-S_0	E_3-S_0	E_4-S_0
Ni^{2+}	-0.00	0.01	**0.30**	**0.27**	**0.28**	**0.27**	**0.15**
Coordinating N1-N4	-0.03	0.04	**-0.32**	**-0.37**	**-0.37**	**-0.35**	**-0.41**
Aromatic ring 1	**0.16**	0.01	0.01	0.02	0.04	0.03	**0.19**
Aromatic ring 2	**0.16**	0.01	0.02	0.03	0.04	0.03	**0.19**
Non-aromatic ring 1	**-0.11**	-0.08	0.04	0.06	0.05	0.06	0.01
Non-aromatic ring 2	**-0.11**	-0.08	0.03	0.05	0.05	0.06	0.01
N5	-0.03	0.01	-0.01	-0.01	-0.01	-0.01	-0.04
N6	-0.03	0.01	-0.01	-0.01	-0.01	-0.01	-0.04
CH	0.01	0.06	-0.05	-0.05	-0.06	-0.06	-0.07

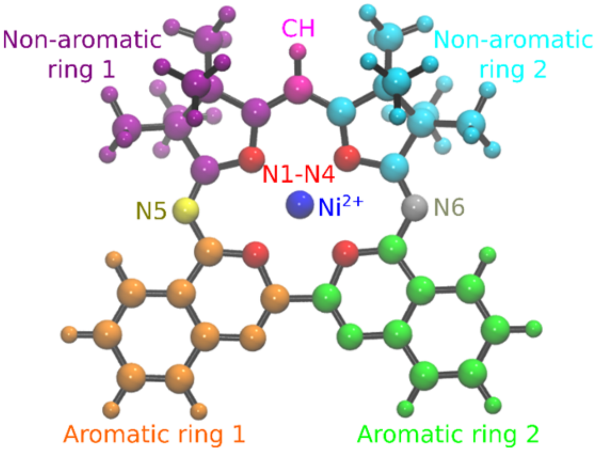

Table S6. Coordinates of the optimized geometry of the singlet ground state (S_0) of $[Zn^{II}(Mabiq)]^+$.

Zn	1.2995720	18.8785283	1.9634064
N	0.0373717	17.5031123	2.6095959
C	0.0708885	16.9230485	3.8256637
N	2.3882622	18.8289104	3.6111737
C	1.0496793	17.1800171	4.7988803
H	0.9485460	16.6458136	5.7430710
N	2.4633428	20.3219245	1.1577122
C	2.1246528	18.0776525	4.6984696
N	0.2841776	19.0921401	0.2284667
C	3.0986402	18.4084305	5.8266728
C	4.2788341	19.0880189	5.0197673
C	3.5522959	19.5526296	3.7605953
N	4.0439500	20.4404251	2.9534618
C	3.5446076	20.8584674	1.7470998
C	4.2237389	21.9214150	1.0557155
C	5.3720166	22.5700766	1.5702054
H	5.7650372	22.2481434	2.5348832
C	5.9657618	23.5882688	0.8476477
H	6.8517419	24.0921712	1.2415670
C	5.4354401	23.9864762	-0.4053989
H	5.9200160	24.7935545	-0.9606958
C	4.3173618	23.3665878	-0.9311121
H	3.8919409	23.6548414	-1.8939918
C	3.6853214	22.3198499	-0.2138243
N	2.5820539	21.7214537	-0.7520256
C	2.0233809	20.7669421	-0.0656419
C	0.7939371	20.0682482	-0.5931583
N	0.2872347	20.4086659	-1.7428199
C	-0.8302980	19.7433026	-2.1588524
C	-1.4105215	20.0882722	-3.4054531
H	-0.9360497	20.8802009	-3.9875233
C	-2.5413194	19.4270866	-3.8469220
H	-2.9862329	19.6954215	-4.8085122
C	-3.1340198	18.4011197	-3.0685407
H	-4.0266349	17.8916657	-3.4396866
C	-2.5910632	18.0420782	-1.8488414
H	-3.0309447	17.2549226	-1.2359110
C	-1.4347387	18.7055547	-1.3726821
C	-0.8107393	18.3938010	-0.1146493
N	-1.3528604	17.3959587	0.6533260
C	-0.9829677	16.9993384	1.8311441
C	-1.5991787	15.7882769	2.5260266
C	-1.1486207	16.0264473	4.0245147
C	3.5126237	17.1958829	6.6699503
H	2.6723861	16.8398150	7.2854977
H	4.3200092	17.4804059	7.3622708
H	3.8646231	16.3534174	6.0589859
C	2.3706532	19.4303172	6.7385190
H	2.0785162	20.3383221	6.1888539
H	3.0209668	19.7261415	7.5744162
H	1.4593555	18.9803725	7.1606742
C	5.3202993	18.0446977	4.5407749
H	6.0143611	18.5198364	3.8319010
H	4.8468657	17.1888500	4.0343675
H	5.9052292	17.6632503	5.3902001
C	5.0058346	20.2229691	5.7451088
H	5.8212446	20.6032046	5.1135875
H	5.4444981	19.8558264	6.6860851
H	4.3453140	21.0700957	5.9739919
C	-0.9005766	14.5507595	1.9071343
H	-1.2975252	13.6230072	2.3440355
H	0.1895681	14.5683749	2.0637570
H	-1.0895675	14.5282850	0.8237543
C	-3.1090290	15.6734646	2.3020841
H	-3.6485660	16.5892476	2.5787429
H	-3.5191891	14.8346888	2.8859292
H	-3.3116325	15.4810446	1.2390201
C	-0.8605769	14.7465311	4.8193743
H	-0.0016881	14.1860102	4.4257831
H	-1.7417975	14.0869459	4.7976171
H	-0.6583672	14.9776349	5.8763958
C	-2.1856449	16.8785286	4.8021774
H	-1.7792460	17.1688038	5.7828596
H	-3.1038160	16.2983509	4.9740858
H	-2.4537145	17.7979634	4.2592487

Table S7. Coordinates of the optimized geometry of the first excited singlet (S_1) of $[Zn^{II}(Mabiq)]^+$.

Zn	1.2382775	18.9082093	2.0290316
N	0.0213439	17.4896504	2.6299414
C	0.0601578	16.9045405	3.8591079
N	2.2887635	18.9867752	3.7037400
C	1.0505983	17.1842357	4.8319605
H	0.9834289	16.6017530	5.7525096
N	2.5277002	20.2490985	1.1346132
C	2.0708622	18.1159248	4.7820783
N	0.2771142	19.1151109	0.2753170
C	3.1051406	18.4165243	5.8585780
C	4.2717623	19.0319582	4.9739377
C	3.4735483	19.5807152	3.7974029
N	3.9901772	20.5239526	2.9918966
C	3.5536002	20.8681389	1.7927376
C	4.1809293	21.9865263	1.0903765
C	5.2729184	22.6870642	1.6065238
H	5.6929706	22.3699698	2.5629465
C	5.8333222	23.7640154	0.8866305
H	6.6823570	24.3070528	1.3082015
C	5.3233977	24.1270898	-0.3711247
H	5.7731490	24.9545572	-0.9240346
C	4.2522557	23.4296742	-0.9122097
H	3.8254898	23.6825219	-1.8847825
C	3.6483109	22.3470166	-0.1871760
N	2.5948843	21.7127719	-0.7390488
C	2.0583307	20.7173033	-0.0463691
C	0.8245267	20.0374798	-0.5765344
N	0.3787290	20.3508777	-1.7574491
C	-0.7422419	19.6837402	-2.1878970
C	-1.2790060	20.0016675	-3.4578043
H	-0.7794566	20.7745520	-4.0448258
C	-2.4078661	19.3406523	-3.9233134
H	-2.8183140	19.5912508	-4.9045865
C	-3.0256746	18.3445803	-3.1411127
H	-3.9099034	17.8273704	-3.5210741
C	-2.5128775	18.0115488	-1.8906482
H	-2.9729529	17.2395167	-1.2726105
C	-1.3739681	18.6751954	-1.3970431
C	-0.8039053	18.3802734	-0.0898105
N	-1.3617223	17.4166229	0.6623983
C	-0.9898792	17.0118160	1.8622518
C	-1.6256006	15.8055416	2.5501781
C	-1.1762033	16.0332738	4.0536691
C	3.5199890	17.1974961	6.6885422
H	2.6998972	16.8815928	7.3517738
H	4.3758522	17.4495721	7.3343975
H	3.7967785	16.3363876	6.0649589
C	2.5031447	19.4867939	6.8050876
H	2.2202273	20.4025684	6.2632561
H	3.2160573	19.7597173	7.5973188
H	1.5977581	19.0870906	7.2861332
C	5.1878542	17.9292839	4.3849226
H	5.8504894	18.3618644	3.6200154
H	4.6054333	17.1182546	3.9202601
H	5.8187963	17.4936418	5.1733133
C	5.1344854	20.0888517	5.6679644
H	5.9482128	20.4092956	5.0018668
H	5.5867190	19.6670843	6.5792701
H	4.5618885	20.9837736	5.9465834
C	-0.9445739	14.5603667	1.9284843
H	-1.3581633	13.6344889	2.3549711
H	0.1441295	14.5619795	2.0955990
H	-1.1246056	14.5486423	0.8431418
C	-3.1366254	15.7119559	2.3232570
H	-3.6633286	16.6346737	2.6018145
H	-3.5608175	14.8775265	2.9038258
H	-3.3405619	15.5266391	1.2590360
C	-0.9175379	14.7440306	4.8438989
H	-0.0730106	14.1656331	4.4449273
H	-1.8133084	14.1034190	4.8280558
H	-0.7025133	14.9696618	5.9000458
C	-2.2090474	16.8939262	4.8277198
H	-1.8028302	17.1731204	5.8119478
H	-3.1416990	16.3337055	4.9920701
H	-2.4540405	17.8212451	4.2868470

Table S8. Coordinates of the optimized geometry of the lowest triplet state (T_1) of $[Zn^{II}(Mabiq)]^+$.

Zn	1.2875760	18.8818406	2.0167465
N	0.0095404	17.5005682	2.6297393
C	0.0737875	16.8993983	3.8477892
N	2.3852837	18.8520878	3.6439356
C	1.0675737	17.1632706	4.8150291
H	0.9750849	16.6081999	5.7496518
N	2.4496660	20.3080167	1.1854734
C	2.1301864	18.0609530	4.7386898
N	0.2981675	19.0846886	0.2358613
C	3.1109049	18.4085151	5.8562663
C	4.2796744	19.0918393	5.0316463
C	3.5341724	19.5514163	3.7810923
N	4.0394563	20.4556837	2.9622223
C	3.5413435	20.8476085	1.7746037
C	4.2096931	21.9130883	1.0479014
C	5.3527097	22.5705577	1.5398690
H	5.7571544	22.2607686	2.5041794
C	5.9388138	23.5898501	0.7979076
H	6.8260042	24.0990989	1.1823179
C	5.4008205	23.9748378	-0.4511920
H	5.8758728	24.7782343	-1.0191687
C	4.2802585	23.3401835	-0.9581882
H	3.8431928	23.6141327	-1.9201864
C	3.6605170	22.2965226	-0.2211256
N	2.5587549	21.6899105	-0.7486955
C	2.0107501	20.7381889	-0.0368847
C	0.7950428	20.0340135	-0.5518743
N	0.2948071	20.4011527	-1.7534217
C	-0.8090962	19.7513992	-2.1698709
C	-1.3699805	20.1189342	-3.4330063
H	-0.8691751	20.9121063	-3.9917482
C	-2.5105902	19.4830233	-3.9120524
H	-2.9348993	19.7706060	-4.8764589
C	-3.1129606	18.4705603	-3.1528286
H	-4.0076488	17.9676928	-3.5282963
C	-2.5766910	18.0847257	-1.9006750
H	-3.0440365	17.2924783	-1.3129704
C	-1.4421126	18.7079036	-1.3996154
C	-0.8356969	18.3617954	-0.1063149
N	-1.3662472	17.4244228	0.6484626
C	-0.9892122	17.0038265	1.8656468
C	-1.6044927	15.7819049	2.5358802
C	-1.1529552	16.0068113	4.0399602
C	3.5480952	17.2074762	6.7033347
H	2.7145421	16.8421556	7.3230052
H	4.3548148	17.5037523	7.3920475
H	3.9064365	16.3673061	6.0930155
C	2.3949251	19.4332181	6.7735374
H	2.0833776	20.3326122	6.2201128
H	3.0528053	19.7459161	7.5977727
H	1.4944053	18.9778044	7.2126490
C	5.3199390	18.0534482	4.5397756
H	5.9982272	18.5266128	3.8140580
H	4.8410472	17.1909797	4.0502943
H	5.9237897	17.6817779	5.3806088
C	5.0117243	20.2300781	5.7475597
H	5.8227221	20.6098898	5.1099189
H	5.4566361	19.8666214	6.6872490
H	4.3515515	21.0768352	5.9789368
C	-0.9085948	14.5486847	1.9057324
H	-1.3087212	13.6151062	2.3282659
H	0.1803445	14.5635618	2.0702622
H	-1.0903097	14.5363989	0.8203668
C	-3.1156077	15.6662613	2.3161038
H	-3.6559368	16.5786670	2.6025493
H	-3.5235232	14.8225100	2.8946036
H	-3.3235237	15.4802886	1.2524539
C	-0.8792539	14.7167232	4.8218170
H	-0.0277189	14.1505617	4.4203116
H	-1.7675487	14.0660138	4.8019069
H	-0.6673454	14.9383622	5.8792633
C	-2.1895448	16.8556460	4.8203809
H	-1.7817457	17.1349535	5.8038575
H	-3.1160047	16.2863611	4.9872606
H	-2.4459928	17.7829055	4.2846986

Table S9. Coordinates of the optimized geometry of the singlet ground state (S_0) of [Ni^{II}(Mabiq)]$^+$.

Ni	5.4375394	7.2474667	9.1796782
N	6.3495389	8.7668673	8.4460648
N	6.2458066	10.2349112	6.5635108
N	7.9536302	9.1174015	10.1701416
N	6.4342243	7.3607648	10.7873195
N	4.4475643	5.7557371	9.7997953
N	3.2042123	5.2662372	7.8022946
N	4.4854249	7.2524279	7.5148567
N	4.2314250	8.5901059	5.5509766
C	5.8505303	9.1940400	7.2297195
C	7.2497913	10.9902679	7.0874577
C	7.6993171	12.1400238	6.3929371
H	7.2158513	12.3908948	5.4473147
C	8.7240889	12.9013308	6.9235278
H	9.0734903	13.7892901	6.3906850
C	9.3325852	12.5434761	8.1529179
H	10.1425396	13.1592945	8.5510324
C	8.9123362	11.4248506	8.8491211
H	9.3699889	11.1347678	9.7949065
C	7.8610961	10.6330339	8.3269690
C	7.3594191	9.4631746	8.9987725
C	7.5363485	8.1815981	10.9522296
C	8.2919089	7.8124994	12.2183377
C	9.3792419	6.7948254	11.7880246
H	8.9454708	5.8919992	11.3301817
H	9.9829145	6.4878708	12.6543949
H	10.0499232	7.2631428	11.0525388
C	8.9625767	9.0137840	12.8875744
H	9.7757156	9.3910506	12.2518382
H	9.3947829	8.7147827	13.8552090
H	8.2645137	9.8445449	13.0566914
C	7.1476639	7.1277626	13.0478816
C	7.6171203	6.0100767	13.9874531
H	8.0225989	5.1439732	13.4466922
H	6.7929914	5.6569414	14.6258525
H	8.4003004	6.3950383	14.6585645
C	6.3317183	8.1647677	13.8629079
H	6.9356617	8.5544527	14.6951117
H	5.4340262	7.6906255	14.2878610
H	6.0062787	9.0139329	13.2425526
C	4.4618479	5.2228718	11.0434545
C	5.2920787	5.6493969	12.0704602
H	5.2099486	5.1564540	13.0367219
C	6.2391203	6.6534425	11.9239104
C	3.4164273	4.1292636	11.2009614
C	3.8395768	2.9856535	12.1308089
H	3.1133661	2.1614199	12.0579794
H	3.8492020	3.3124165	13.1818055
H	4.8353622	2.5891395	11.8895400
C	2.1520718	4.8134749	11.7833643
H	1.7791659	5.6171371	11.1299693
H	2.3783001	5.2524280	12.7669437
H	1.3483881	4.0751603	11.9180921
C	3.2121257	3.7146226	9.7003325
C	1.8049200	3.2389789	9.3338587
H	1.0484284	4.0243473	9.4645402
H	1.5245902	2.3736324	9.9545852
H	1.7774735	2.9271609	8.2804618
C	4.2448700	2.6491893	9.2517030
H	4.2008740	2.5329176	8.1587326
H	4.0161530	1.6754895	9.7086848
H	5.2746225	2.9276411	9.5255392
C	3.6064619	5.0037612	8.9984785
C	3.5571933	6.3722365	7.0976820
C	2.8961211	6.5871218	5.8373295
C	1.9042450	5.7113336	5.3334599
H	1.6341975	4.8309428	5.9165386
C	1.3022343	5.9905728	4.1200874
H	0.5356235	5.3191140	3.7261331
C	1.6700296	7.1410420	3.3778165
H	1.1805054	7.3411842	2.4213818
C	2.6395029	8.0070793	3.8484890
H	2.9439440	8.8974882	3.2959045
C	3.2707356	7.7434495	5.0888627
C	4.7835586	8.3246875	6.6948198

Table S10. Coordinates of the optimized geometry of the lowest triplet state (T_1) of $[\mathrm{Ni}^{\mathrm{II}}(\mathrm{Mabiq})]^{+}$.

Ni	5.4499145	7.2322353	9.1788937
N	6.3864433	8.8110865	8.3998022
N	6.3401379	10.1965491	6.4704298
N	7.8979383	9.1969726	10.2119326
N	6.4819358	7.3594849	10.8411700
N	4.4184778	5.6906265	9.8144962
N	3.1136176	5.3237327	7.8295770
N	4.4674358	7.2567316	7.4438783
N	4.3054184	8.5406982	5.4514625
C	5.9167998	9.1773275	7.1579714
C	7.3256633	10.9642293	7.0189237
C	7.8072803	12.0865086	6.2996460
H	7.3665164	12.2964220	5.3236500
C	8.8053422	12.8745538	6.8412731
H	9.1750979	13.7398946	6.2854946
C	9.3593118	12.5743734	8.1110707
H	10.1485819	13.2112466	8.5175117
C	8.9107774	11.4849150	8.8345914
H	9.3258996	11.2368165	9.8117553
C	7.8869716	10.6644686	8.3032010
C	7.3624255	9.5168319	8.9947656
C	7.5206331	8.2504906	11.0121743
C	8.2773674	7.9190136	12.2937185
C	9.4710359	7.0308164	11.8596319
H	9.1403146	6.1052170	11.3627138
H	10.0850808	6.7554710	12.7293439
H	10.1050547	7.5891779	11.1552524
C	8.8135572	9.1606002	13.0108843
H	9.5872056	9.6397221	12.3945195
H	9.2687898	8.8786813	13.9731631
H	8.0330698	9.9100354	13.1992492
C	7.1901146	7.0917082	13.0858900
C	7.7537463	5.9719880	13.9697779
H	8.2379192	5.1753300	13.3887524
H	6.9594345	5.5127309	14.5778069
H	8.4951220	6.3864982	14.6701793
C	6.2935196	8.0135926	13.9528087
H	6.8679015	8.4185539	14.7985284
H	5.4453304	7.4433644	14.3608718
H	5.8887933	8.8576573	13.3736308
C	4.4995908	5.1334401	11.0399735
C	5.3895598	5.5476607	12.0388237
H	5.3442598	5.0184810	12.9898014
C	6.3110087	6.5977623	11.9408358
C	3.4342706	4.0558417	11.2184946
C	3.8947825	2.8532239	12.0516959
H	3.1368381	2.0559629	12.0074489
H	4.0093737	3.1286619	13.1112262
H	4.8508771	2.4379104	11.7051310
C	2.2433460	4.7401326	11.9387428
H	1.8495983	5.5928891	11.3648483
H	2.5592435	5.1110640	12.9255117
H	1.4264865	4.0203386	12.0929443
C	3.0886080	3.7238013	9.7137113
C	1.6292147	3.3526209	9.4386736
H	0.9341110	4.1709633	9.6697974
H	1.3416001	2.4702511	10.0315758
H	1.5034801	3.1051822	8.3751984
C	4.0085316	2.6139644	9.1442537
H	3.8683441	2.5462810	8.0553739
H	3.7557582	1.6380866	9.5836349
H	5.0731175	2.8166308	9.3404287
C	3.5176255	5.0123648	9.0205146
C	3.5077944	6.3927208	7.0731201
C	2.8710790	6.5931648	5.7982953
C	1.8461409	5.7500466	5.3060961
H	1.5233964	4.9070208	5.9174968
C	1.2799991	6.0100305	4.0717653
H	0.4878920	5.3626535	3.6880764
C	1.7190419	7.1110000	3.2942575
H	1.2588960	7.2979365	2.3207529
C	2.7204127	7.9467399	3.7517996
H	3.0763474	8.7992864	3.1709443
C	3.3182205	7.7065254	5.0142749
C	4.8305993	8.2952898	6.6154161

Details, NMR and Absorption Spectra of Photoredox Catalysis Reactions

General Procedure for Aerobic Photooxidative Aza-Henry Reaction

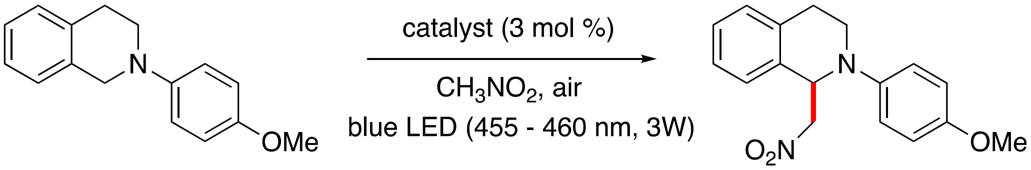

In a typical procedure, the catalyst (3 mol%) and methoxyphenyl)-1,2,3,4-tetrahydroisoquinoline (12 mg, 0.05 mmol) were weighed into an oven-dried 12 mL snap cap vial equipped with a magnetic stirring bar. Nitromethane (2 mL) was added vial, which was then capped. The vial was placed into the photoreactor and an air-filled balloon was attached to it. The reaction mixture was irradiated with blue LEDs (455 – 460 nm), with a final reaction temperature of 25 °C. After the reaction time, the solvent was evaporated in vacuo and the yield was determined by ^{1}H NMR using mesitylene as an internal standard.

The crude product was dissolved in 2 mL each of DCM and ether, and the resulting suspension was filtered through a plug of silica and washed with ether. The solvent was removed in vacuo and the product, 2-(4-methoxyphenyl)-1-(nitromethyl)-1,2,3,4-tetrahydroisoquinoline was obtained as a yellow oil (11.6 mg, 78% isolated yield using **1** as the catalyst).

^{1}H NMR (400 MHz, $CDCl_3$) δ 7.26 – 7.11 (m, 4H), 6.95 – 6.89 (m, 2H), 6.85 – 6.78 (m, 2H), 5.39 (dd, *J* = 8.6, 5.8 Hz, 1H), 4.83 (dd, *J* = 11.9, 8.6 Hz, 1H), 4.56 (dd, *J* = 11.9, 5.8 Hz, 1H), 3.75 (s, 3H), 3.62 – 3.53 (m, 2H), 3.07 – 2.95 (m, 1H), 2.70 (dt, *J* = 16.5, 4.1 Hz, 1H). ^{13}C NMR (101 MHz, $CDCl_3$) δ 154.2, 143.2, 135.6, 133.1, 129.6, 128.1, 127.1, 126.8, 119.0, 114.9, 79.1, 59.1, 55.7, 43.3, 26.0.

General Procedure for Oxidative Amine Coupling

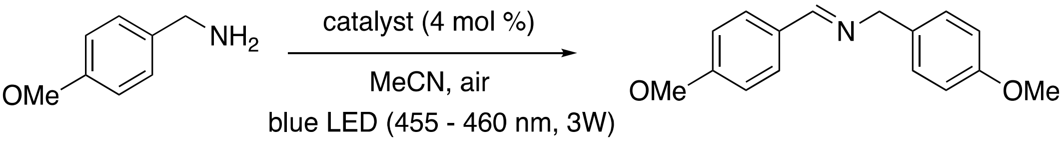

The catalyst (4 mol%) was weighed into an oven-dried 12 mL snap cap vial equipped with a magnetic stirring bar. 4-Methoxybenzylamine (0.05 mmol, 6 µL) and dry MeCN (2 mL) were added into the vial, which was then capped. The vial was placed on the photoreactor and an air-filled balloon was attached to it. The reaction mixture was irradiated with blue LEDs (455 – 460 nm), with a final reaction temperature of 32 – 35 °C. After the reaction time, the solvent was evaporated in vacuo and the product yield was determined by ^{1}H NMR using mesitylene as an internal standard.

N-(4-methoxybenzyl)-1-(4-methoxyphenyl)methanimine: ^{1}H NMR ($CDCl_3$, 400 MHz): δ 8.28 (s, 1H), 7.68 (d, *J* = 8.6 Hz, 2H), 7.21 (d, *J* = 8.9 Hz, 2H), 6.90 (dd, *J* = 16.8, 8.4 Hz, 4H), 4.69 (s, 2H), 3.76 (d, *J* = 5.4, 6H) ppm. ESI MS found for $[M+H]^+$ *m/z* = 256.09.

Synthesis of 2-(4-methoxyphenyl)-1,2,3,4-tetrahydroisoquinoline

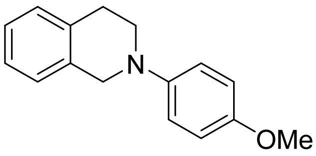

The title compound was synthesized according to literature procedure[37] with slight modifications. Copper iodide (20 mol%, 514 mg), potassium phosphate tribasic (27.00 mmol, 5.73 g, 2 equiv.) and 4-iodoanisole (20.25 mmol, 4.74 g, 1.5 equiv.) were weighed into an oven-dried 100 mL Schlenk flask equipped with a magnetic stirring bar. The flask was evacuated and 1,2,3,4-tetrahydroisoquinoline (13.50 mmol, 1.70 mL, 1 equiv.), ethylene glycol (27.00 mmol, 1.51 mL, 2 equiv.) and isopropanol (50 mL) were added under argon. The reaction solution was then purged with argon for 10 minutes after which it was stirred under reflux for 24 hours at 90 °C. After the reaction time, the mixture was allowed to cool to room temperature and 30 mL each of diethyl ether and water were added. The aqueous phase was extracted with 3 x 30 mL diethyl ether and the combined organic phase was washed with brine and dried with magnesium sulphate. The solvent was removed in vacuo and the crude was purified by silica gel flash column chromatography (hexanes: ethyl acetate = 10:1) to provide the product as a white powder (1.62 g, 50% yield).

^{1}H NMR (400 MHz, $CDCl_3$) δ 7.23 – 7.11 (m, 4H), 7.04 – 6.96 (m, 2H), 6.93 – 6.84 (m, 2H), 4.32 (s, 2H), 3.80 (s, 3H), 3.47 (t, *J* = 5.9 Hz, 2H), 3.01 (t, *J* = 5.9 Hz, 2H). ^{13}C NMR (101 MHz, $CDCl_3$) δ 153.6, 145.5, 134.7 (2C), 128.8, 126.6, 126.4, 126.0, 118.2, 114.7, 55.8, 52.8, 48.6, 29.2.

Photoreactor setup

The photoreactor setup for the photocatalytic reactions consists of a magnetic stirrer and a metal cooling block with an LED panel placed in-between. The cooling block is connected to a water inlet and outlet for temperature-controlled experiments. The LED panel contains 6 high power LED lights (Avonec, 3W, 455 – 460 nm) directly under the vial position of the cooling block, which allows irradiation from the bottom of the samples.

Scheme S1. Photocatalytic cycle for the indole cyclization reaction, as previously reported.[38]

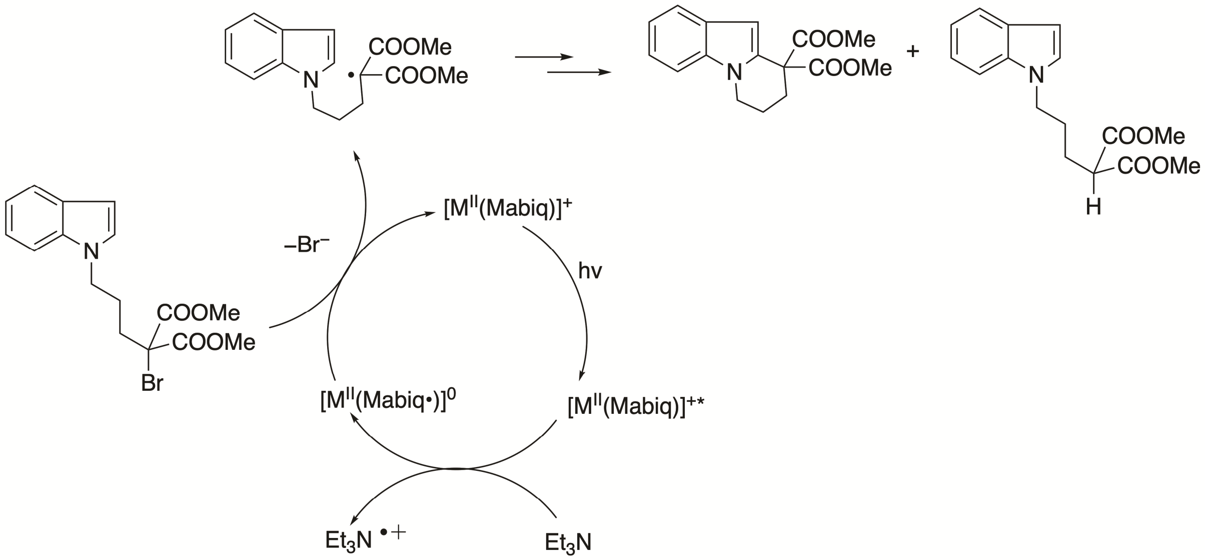

Scheme S2. Photocatalytic cycle for the Aza-Henry reaction, based on the mechanism proposed by Condie et al.[39] [O] = oxidant = nitromethane (CH_3NO_2) or O_2.

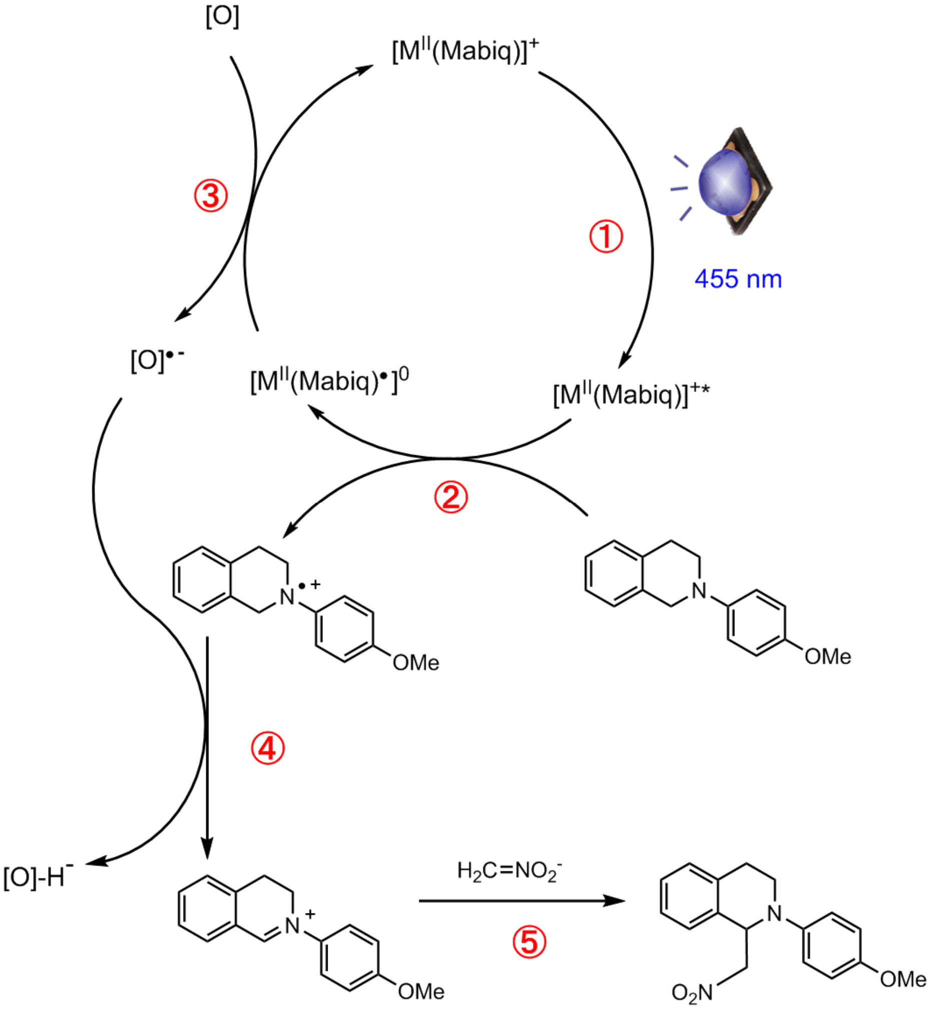

Scheme S3. Energy transfer (red) and electron transfer (blue) mechanisms proposed for the photocatalyzed oxidative coupling of 4-methoxybenzylamine, as adapted from Johnson et al.[37]

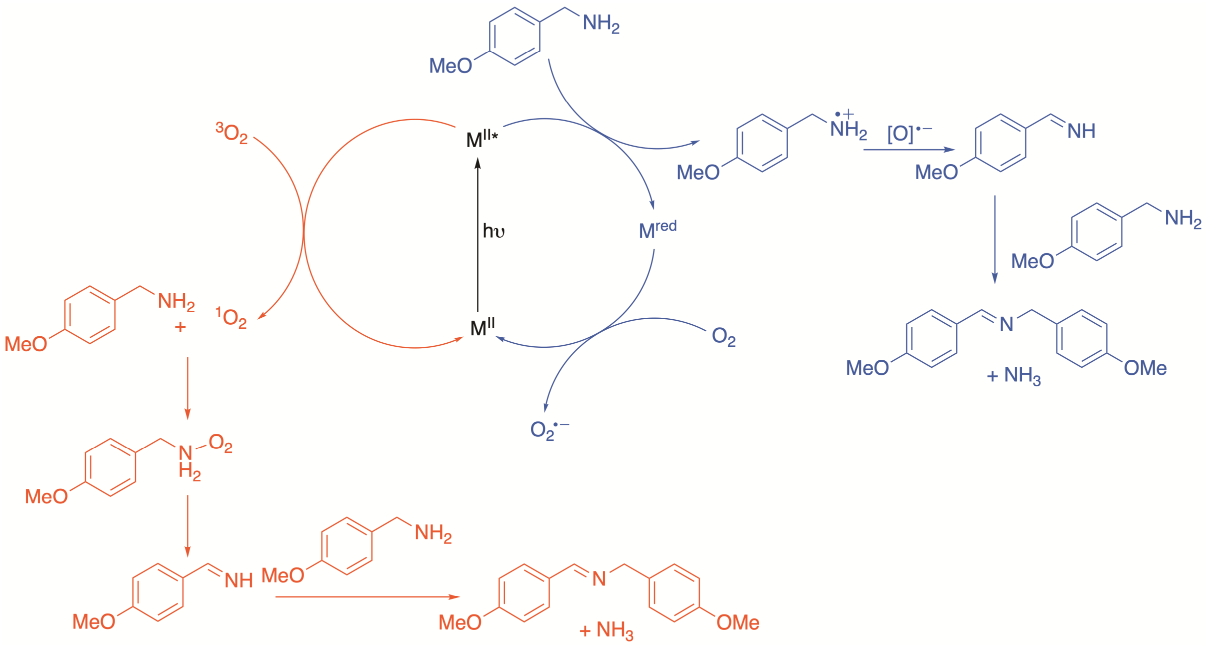

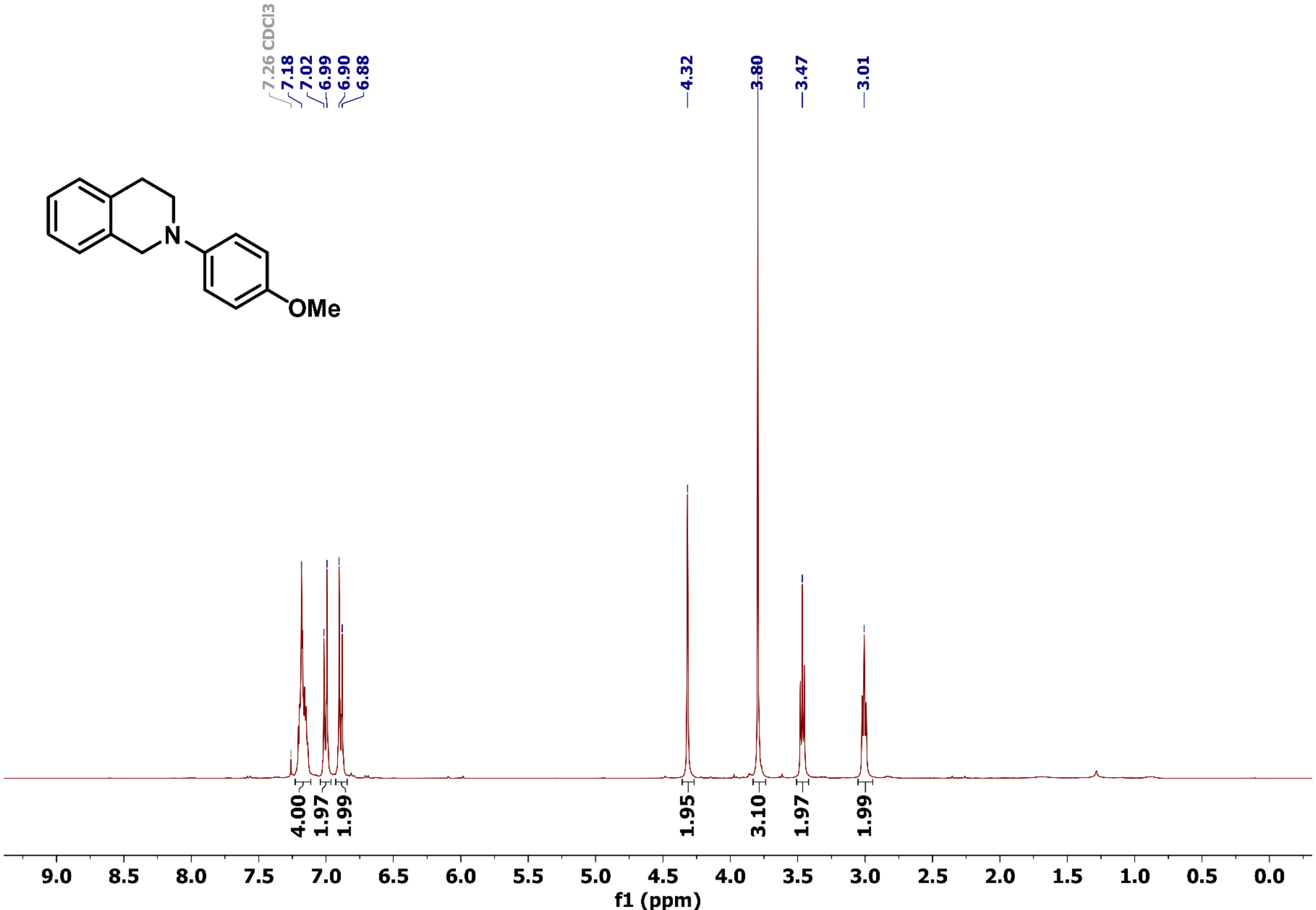

Figure S50. ^{1}H NMR of 2-(4-methoxyphenyl)-1,2,3,4-tetrahydroisoquinoline.

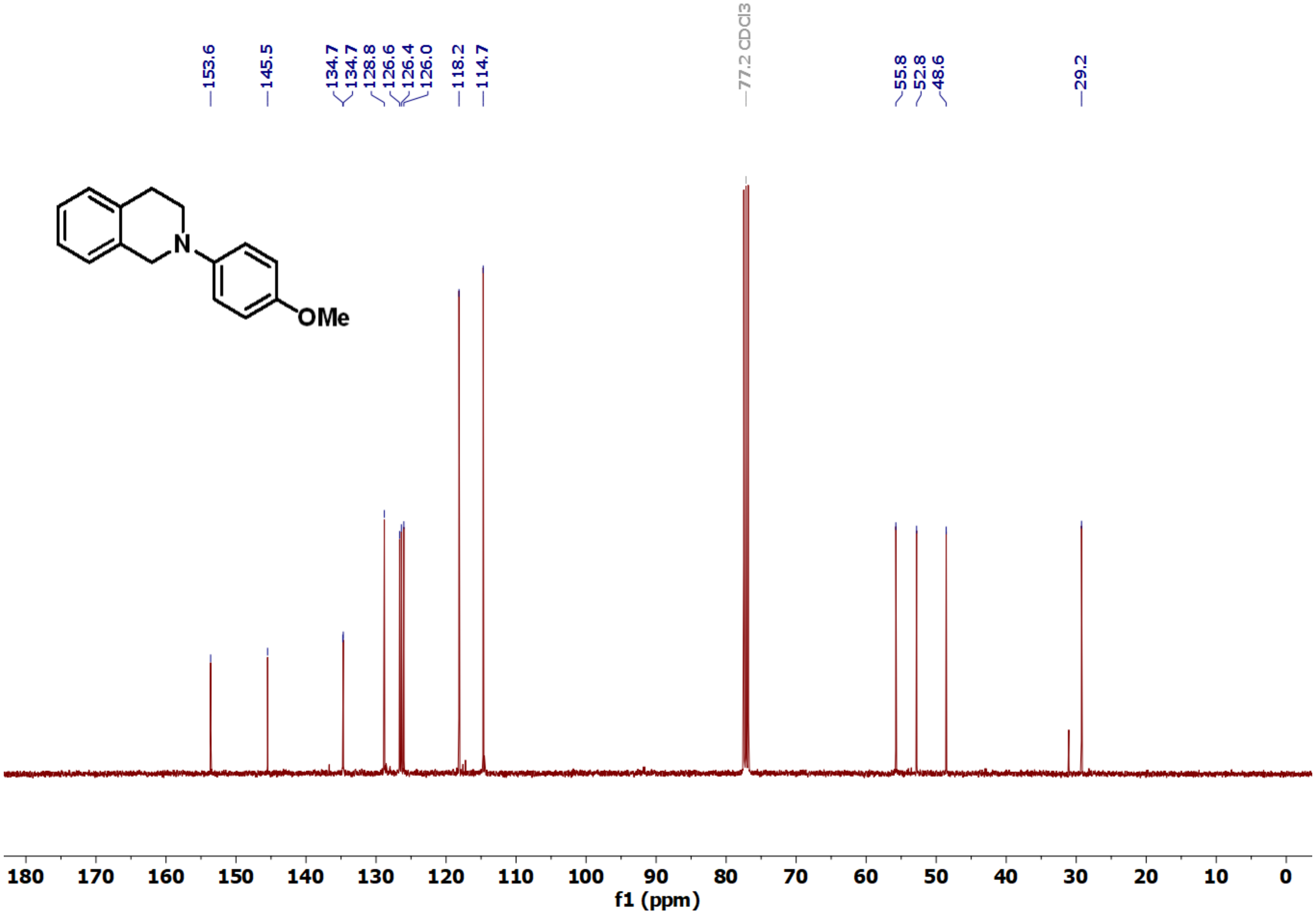

Figure S51. ^{13}C NMR of 2-(4-methoxyphenyl)-1,2,3,4-tetrahydroisoquinoline.

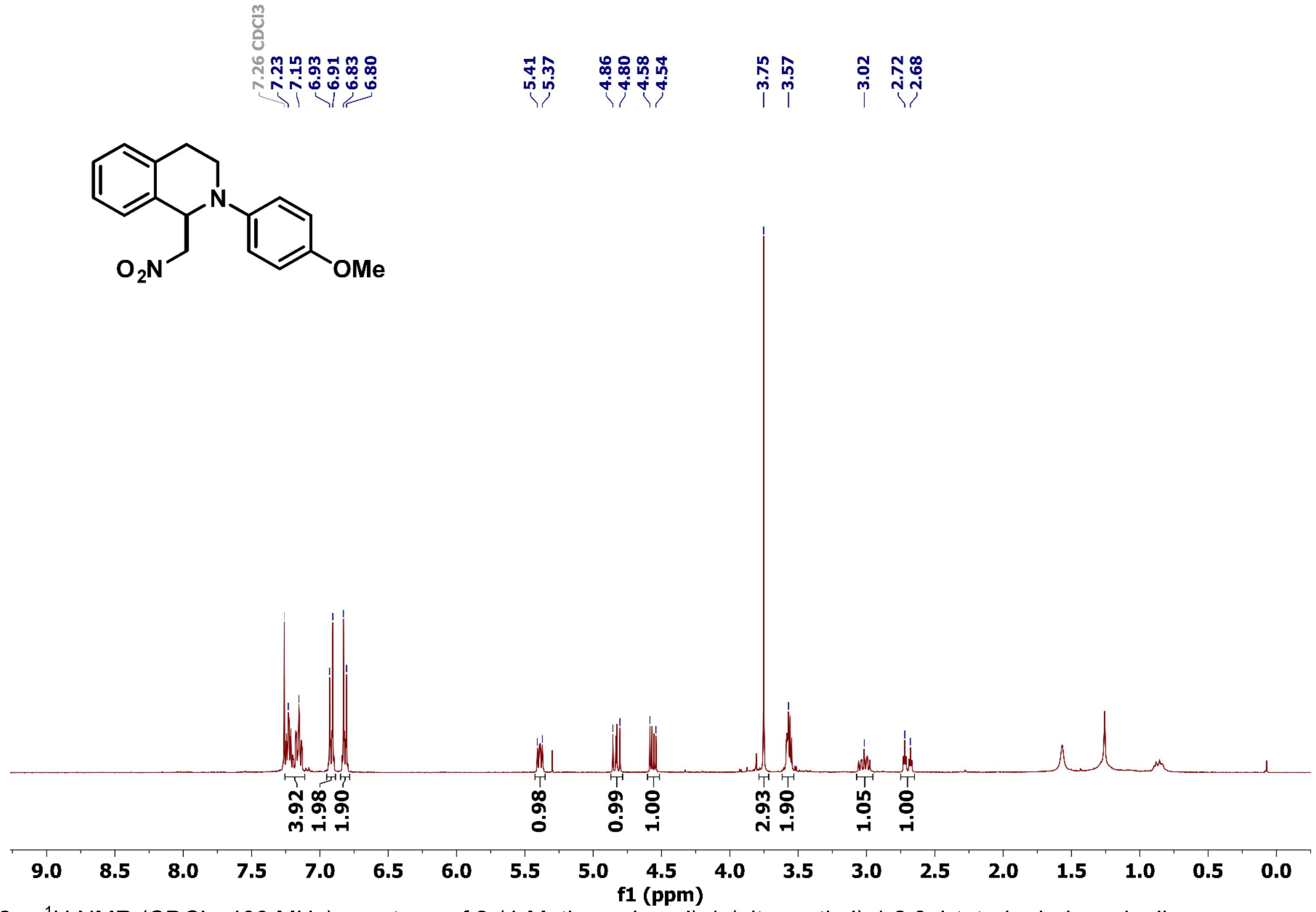

Figure S52. ^1H NMR ($CDCl_3$, 400 MHz) spectrum of 2-(4-Methoxyphenyl)-1-(nitromethyl)-1,2,3,4-tetrahydroisoquinoline.

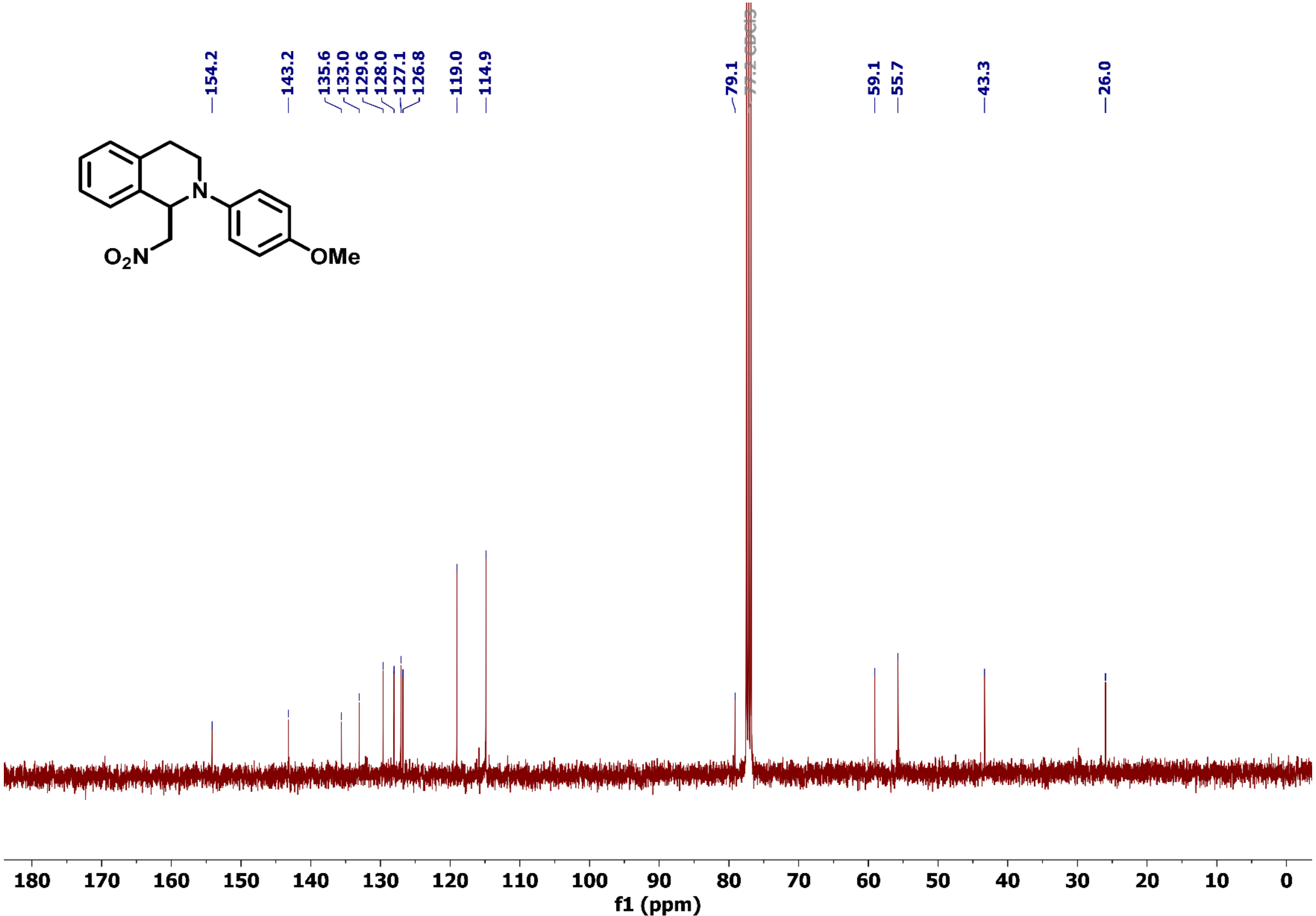

Figure S53. ^{13}C NMR ($CDCl_3$) of 2-(4-Methoxyphenyl)-1-(nitromethyl)-1,2,3,4-tetrahydroisoquinoline.

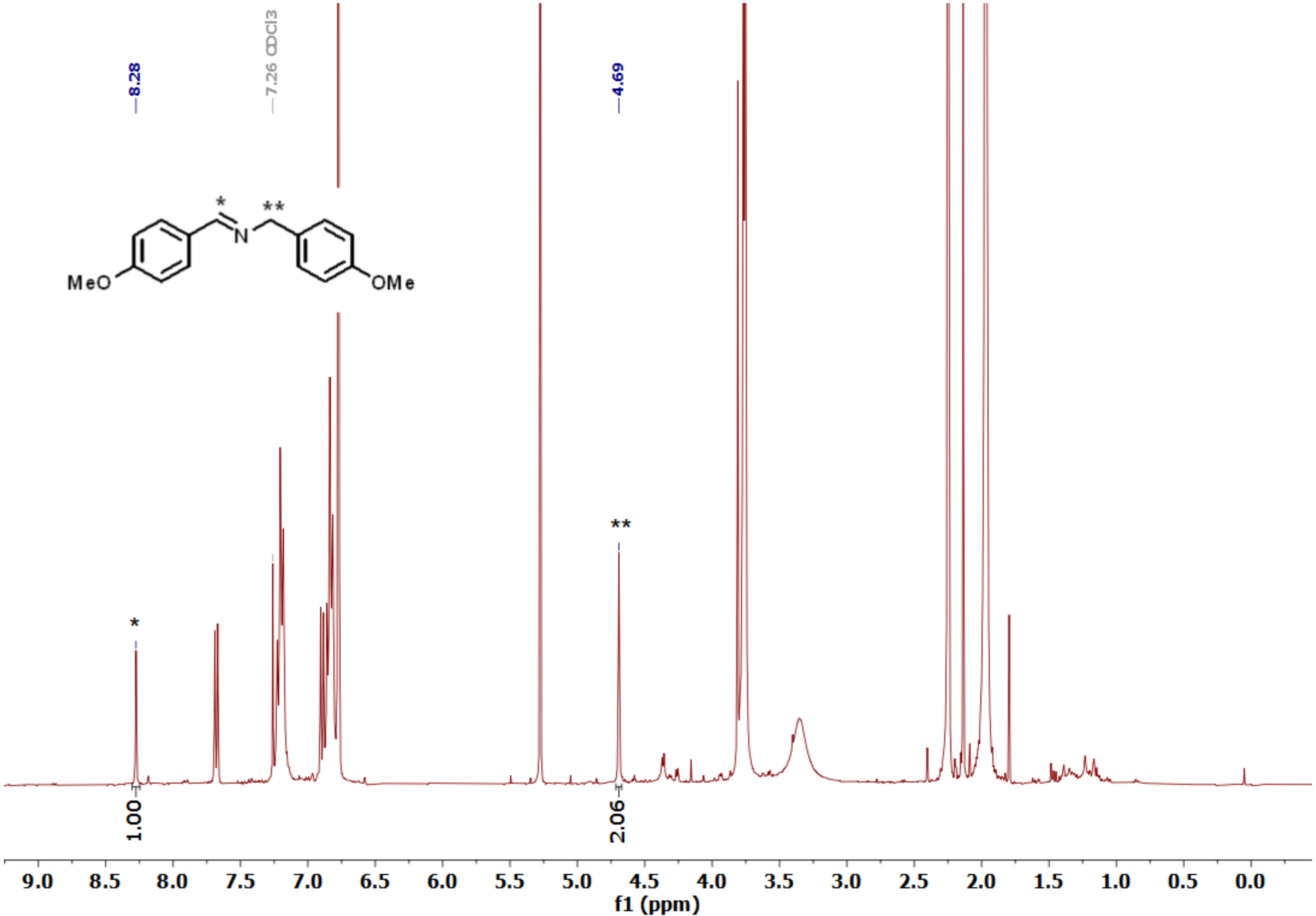

Figure S54. ^{1}H NMR spectrum of crude reaction mixture for photoredox amine coupling (product peaks used for determination of product yields are marked by asterisks).

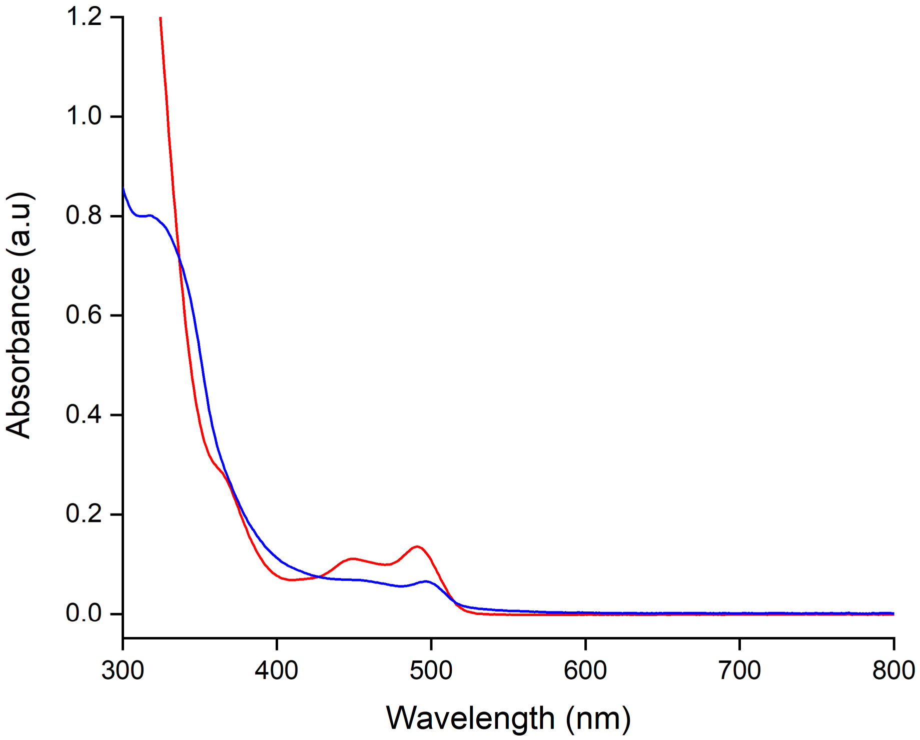

Figure S55. UV-Vis spectra of reaction mixture containing **2** (3 mol%, 1.26 mg, 0.0015 mmol, 0.0015 M) and THIQ (0.05 mmol, 11.97 mg, 0.05 M) in $MeNO_2$ (1 mL). Red trace: before irradiation. Blue trace: After 30 minutes of irradiation with blue LED (455 – 460 nm, 3 W). The spectra were taken by dissolving 10 μL aliquots of reaction mixture in 2 mL of MeCN.

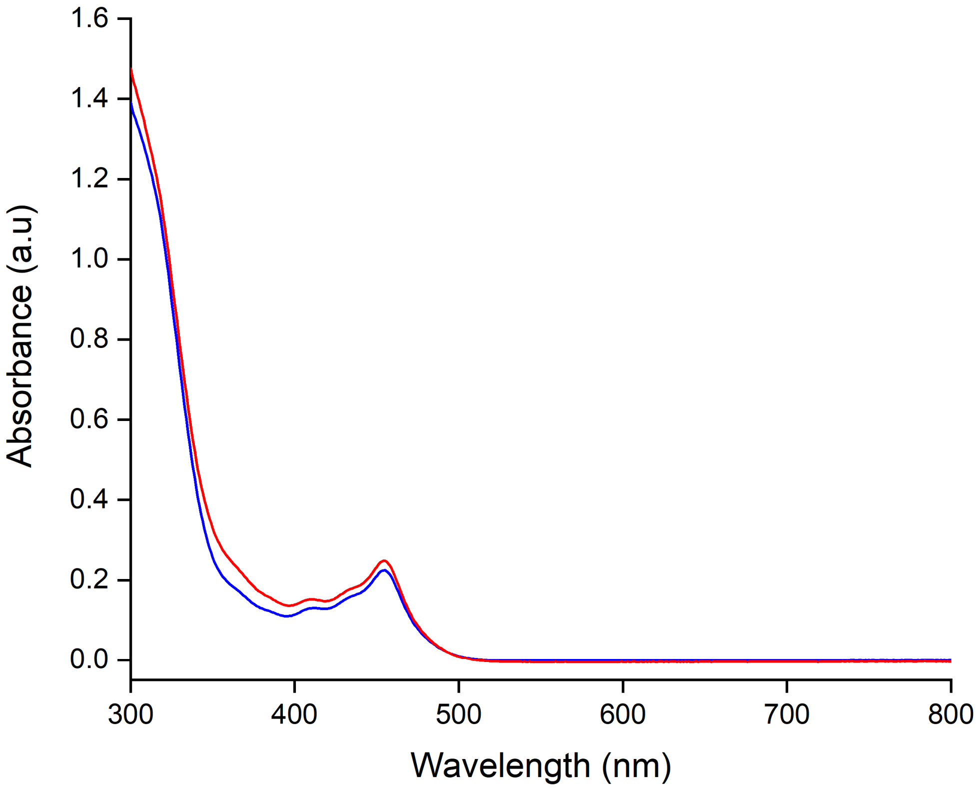

Figure S56. UV-Vis spectra of reaction mixture containing **1** (3 mol%, 1.12 mg, 0.0015 mmol, 0.0015 M) and THIQ (0.05 mmol, 11.97 mg, 0.05 M) in $MeNO_2$ (1 mL). Red trace: before irradiation. Blue trace: After 5 hours of irradiation with blue LED (455 – 460 nm, 3 W). Spectra were taken by dissolving 10 μL aliquots of the reaction mixture in 2 mL of MeCN.

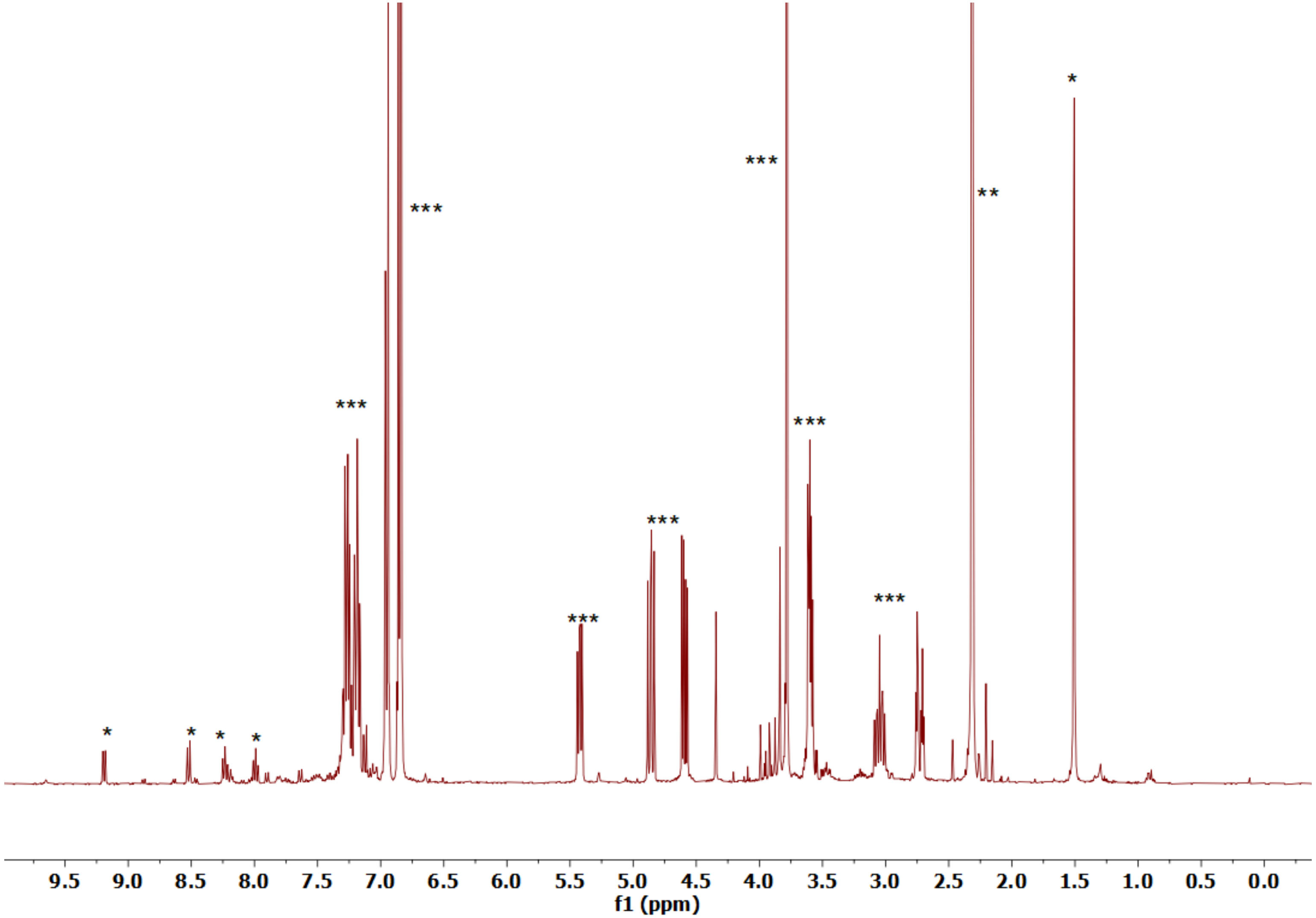

Figure S57. ^{1}H NMR ($CDCl_3$) of the crude Aza-Henry reaction mixture with **1** as the catalyst, after 5 h irradiation. *Peaks = catalyst H, **Peaks = mesitylene H (internal standard); ***Peaks = product H.

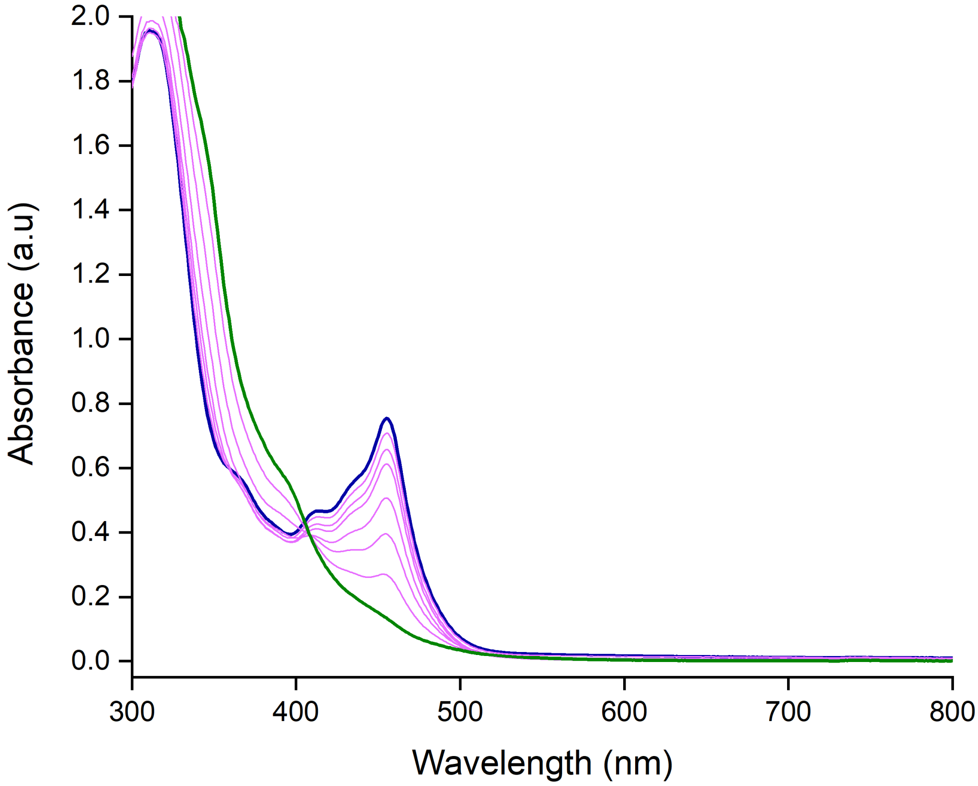

Figure S58. UV-Vis spectral evolution of **1** (20 μM) and THIQ (660 μM, 33 equiv.) in MeCN under inert atmosphere. Blue trace: before irradiation; green trace: after 18 hours of irradiation, with blue LED (455 nm, 130 mW).

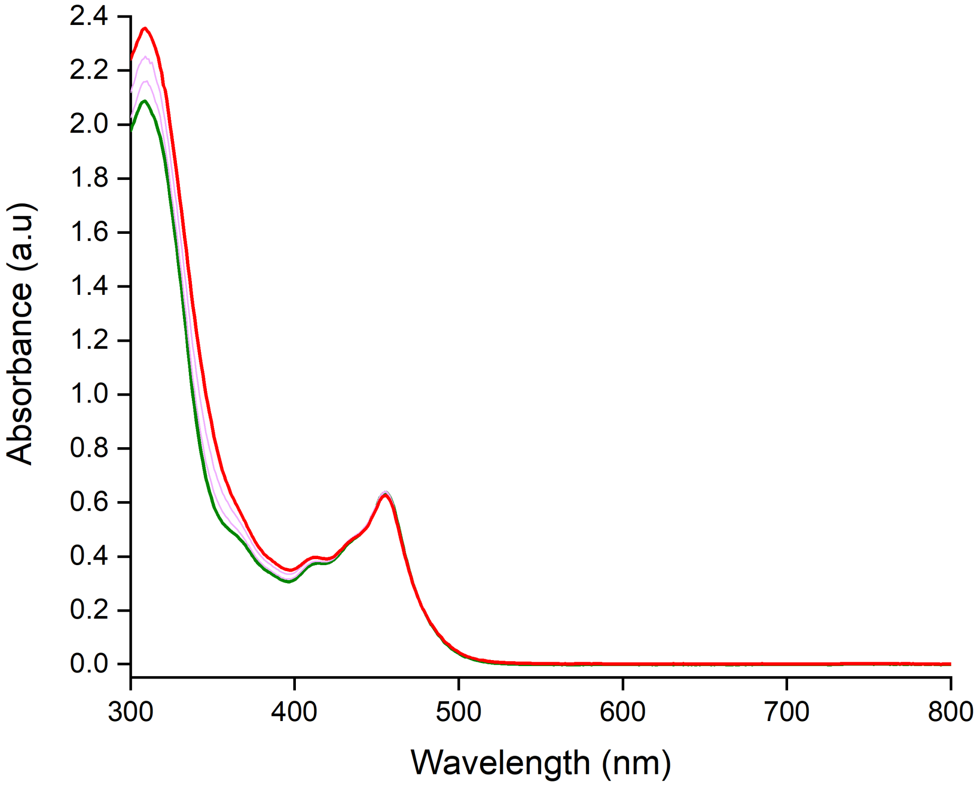

Figure S59. UV-Vis spectral evolution of **1** (20 μM) and THIQ (660 μM, 33 equiv.) in MeCN (2 mL) under air. Green trace: before irradiation; red trace: after 4 hours of irradiation, with blue LED (455 nm, 130 mW).

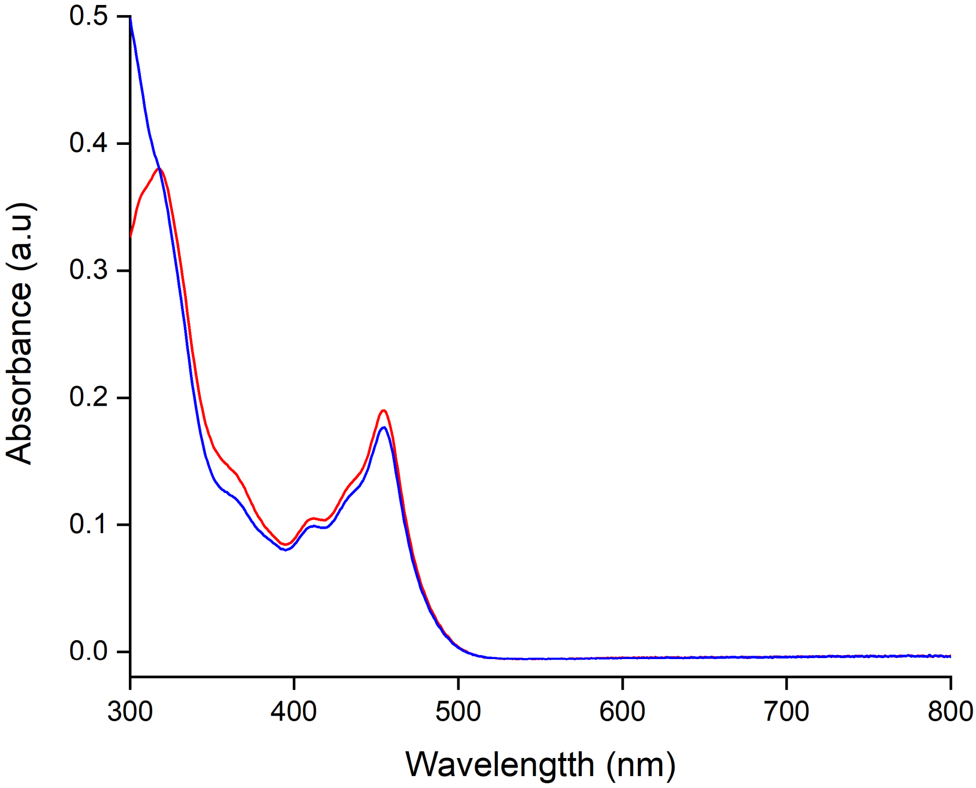

Figure S60. UV-Vis spectra of the oxidative methoxybenzylamine coupling reaction mixture, as catalyzed by **1**. Substrate (0.05 mmol, 7 µL, 0.025 M), MeCN (2 mL), Ni(Mabiq)OTf (4 mol%, 1.5 mg, 0.002 mmol, 0.001 M). Red trace: before irradiation; Blue trace: after 17 h of irradiation with blue LED (3 W, 455 – 460 nm). Spectra were taken by dissolving 10 µL aliquots of the reaction mixture dissolved in 2 mL MeCN.

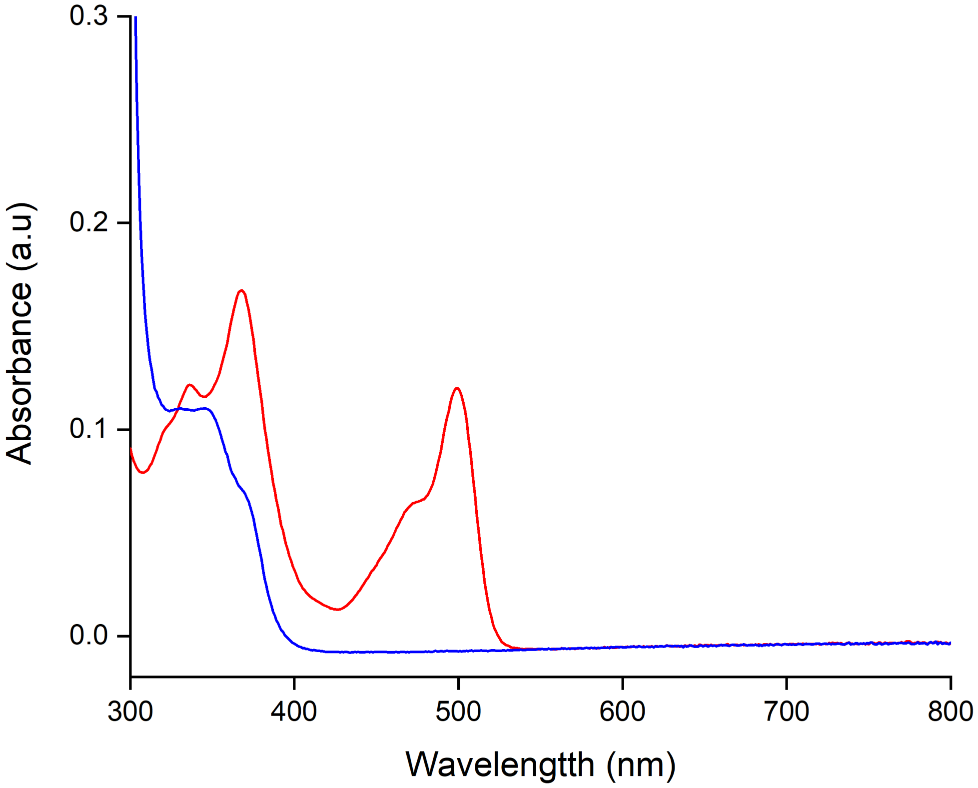

Figure S61. UV-Vis spectra of the oxidative methoxybenzylamine coupling reaction mixture, as catalyzed by **2**. Substrate (0.05 mmol, 7 µL, 0.025 M), MeCN (2 mL), Ni(Mabiq)OTf (4 mol%, 1.5 mg, 0.002 mmol, 0.001 M). Red trace**:** before irradiation; Blue trace**:** after 30 mins of irradiation with blue LED (3 W, 455 – 460 nm). Spectra were taken by dissolving 10 µL aliquots of the reaction mixture dissolved in 2 mL MeCN.

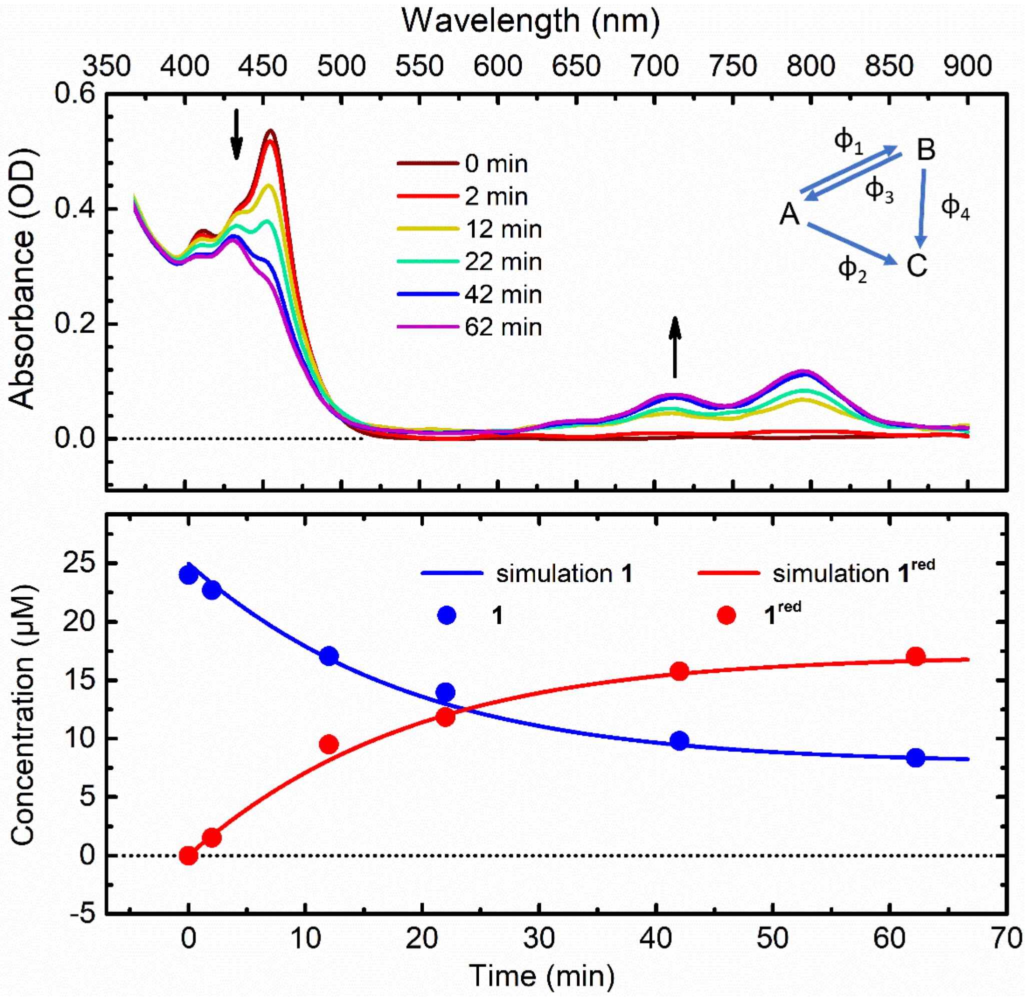

Figure S62. Top: UV-Vis spectral evolution of **1** (20 μM) and 4-methoxybenzylamine (500 μM, 25 equiv.) in MeCN under inert atmosphere and illumination power of 568 mW using 455 nm LED. Bottom: Time evolution of concentrations of **1** and **1**^{red} with reaction quantum yields of $\phi_1 = 1.7 \times 10^{-5}$, $\phi_2 = 0$, $\phi_3 = 1.7 \times 10^{-5}$ and $\phi_4 = 0$.

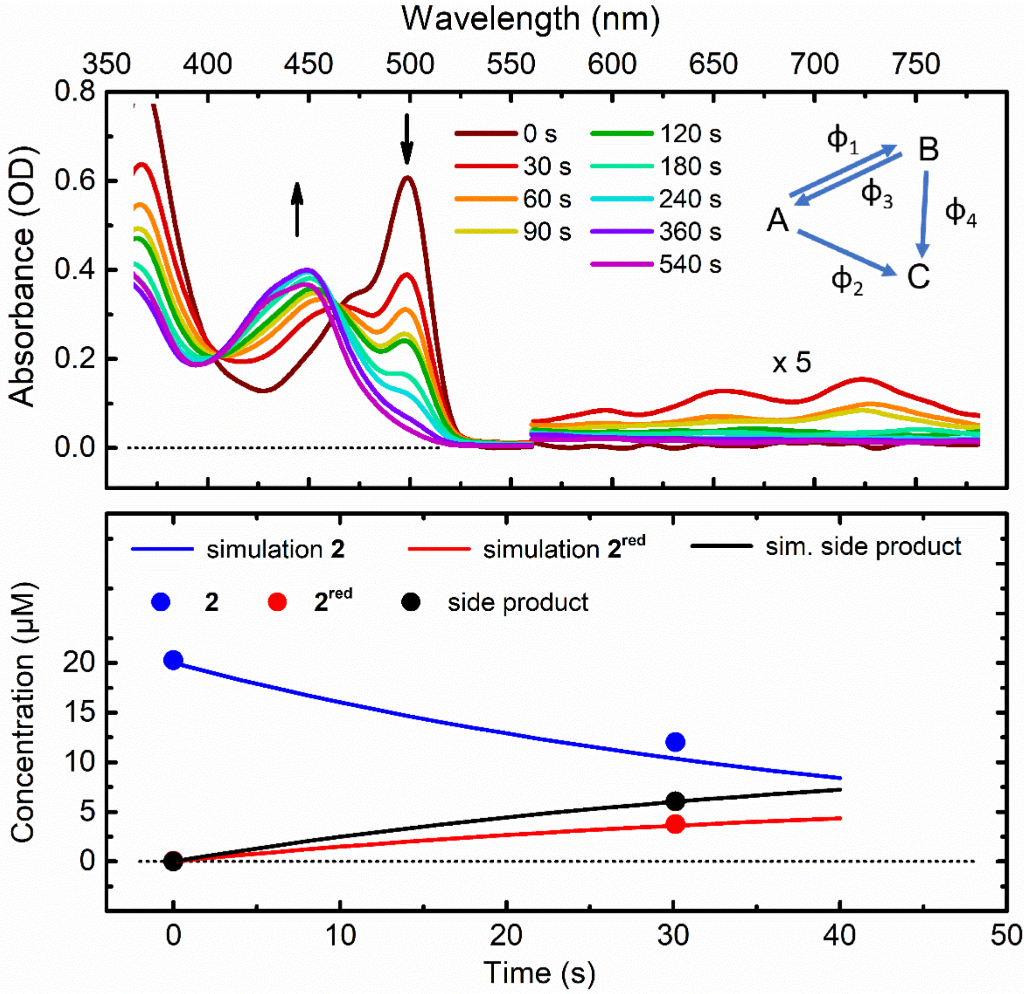

Figure S63. UV-Vis spectral evolution of **2** (20 µM) and 4-methoxybenzylamine (500 µM, 25 equiv.) in MeCN under inert atmosphere and illumination power of 2.4 mW. using 455 nm LED. (bottom) Time evolution of concentrations of **2** and $\mathbf{2}^{\mathbf{red}}$ with reaction quantum yields of $\phi_1 = 0.12$, $\phi_2 = 0.2$, $\phi_3 = 0$ and $\phi_4 = 0$.

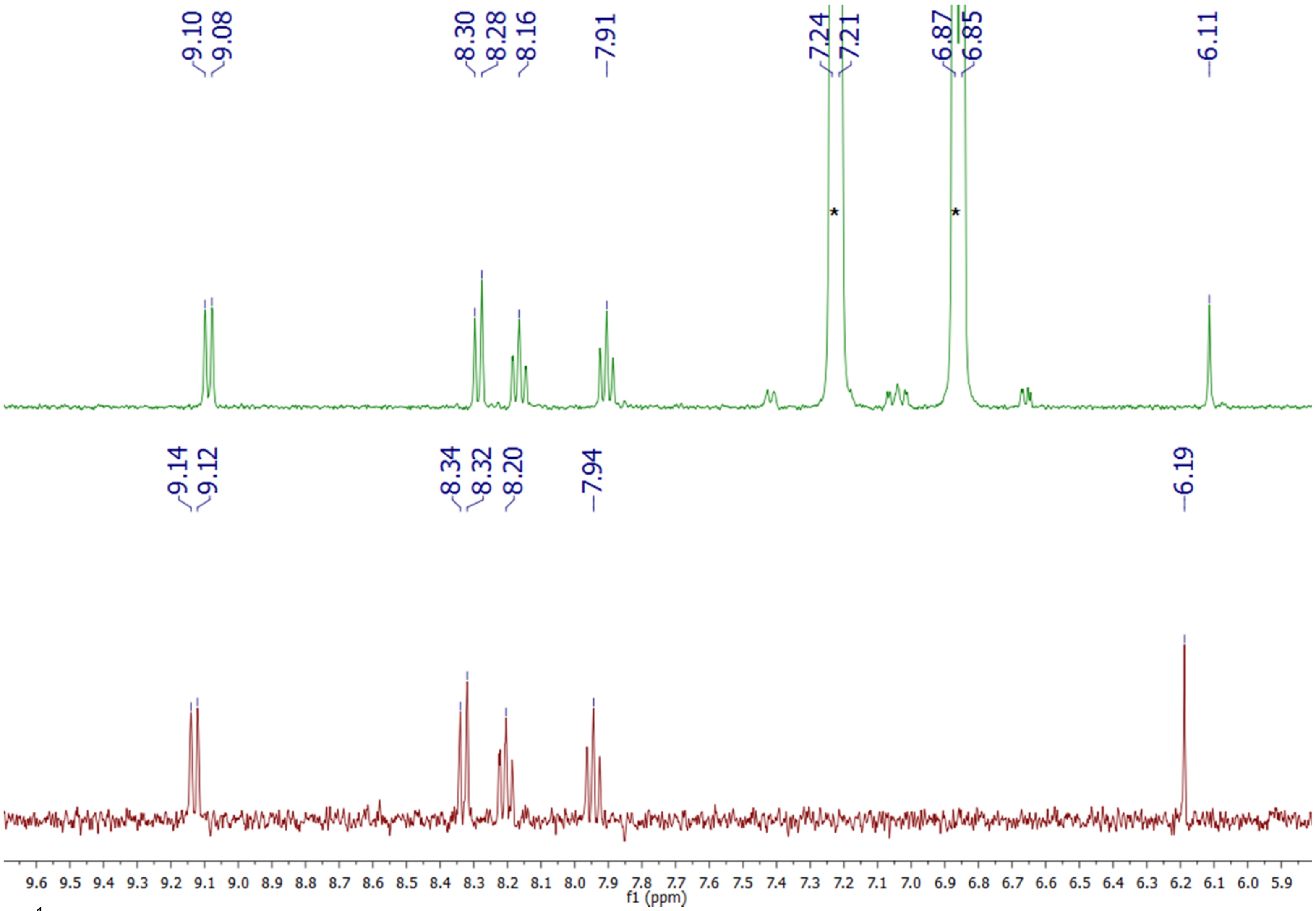

Figure S64. ^{1}H-NMR spectra (aromatic region) of 2 (bottom, red), and of 2 (1.1 mM) with 24 equivalents of 4-methoxybenzylamine added (26.4 mM, top, green), in CD_3CN. The asterisks in the top figure correspond to the 4-methoxybenzylamine signals.

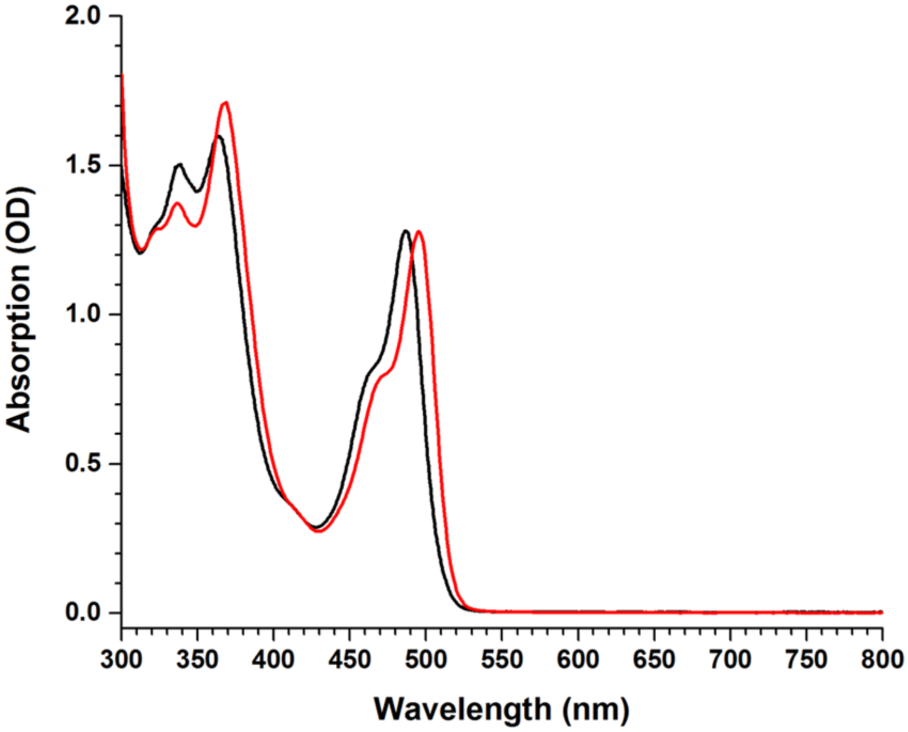

Figure S65. Absorption spectrum of **2** in the absence (black trace) and presence (red trace) of 4-methoxybenzylamine (100 eq); in 1:1 THF:MeCN, under Ar.

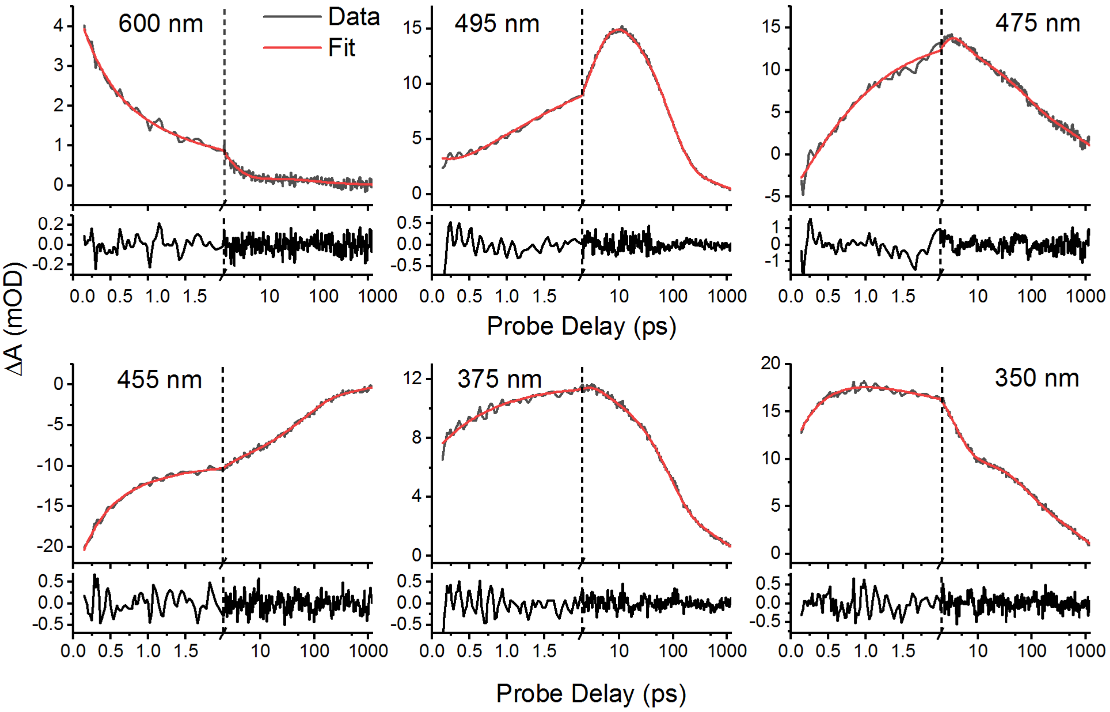

Figure S66. Kinetic traces at selected probe wavelengths in the TA measurements of **1**. Corresponding fit-traces extracted from the global kinetic fit to the data shown as red lines. Fit residuals shown in separate panels below each kinetic trace.

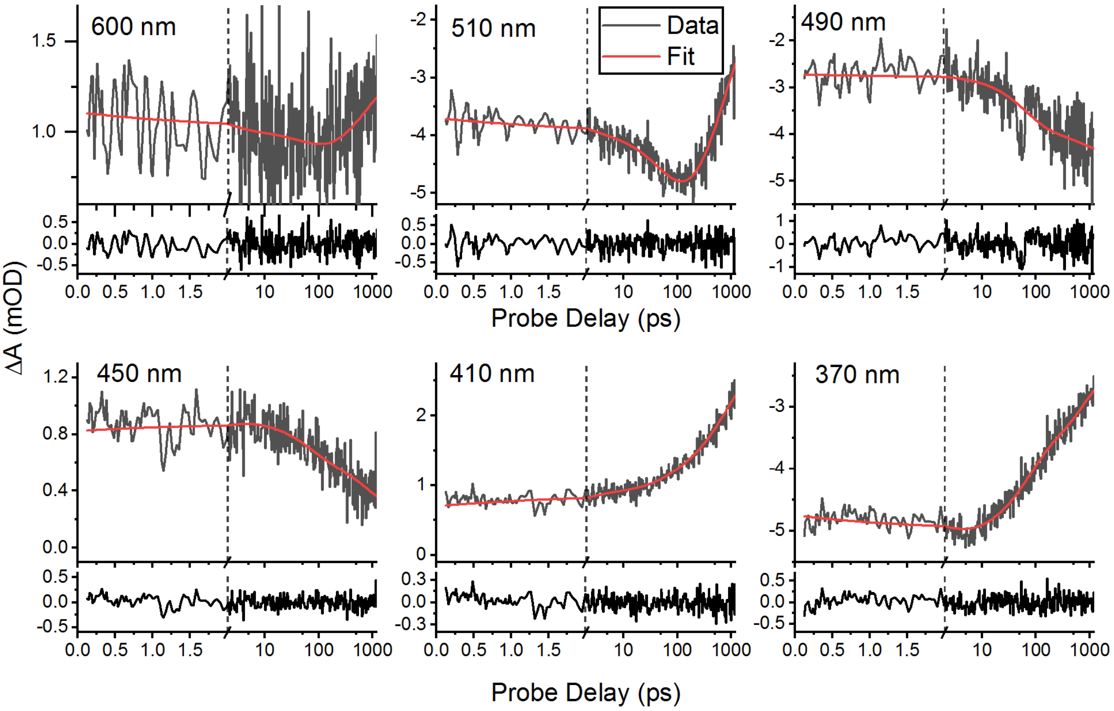

Figure S67. Kinetic traces at selected probe wavelengths in the TA measurements of **2**. Corresponding fit-traces extracted from the global kinetic fit to the data shown as red lines. Fit residuals shown in separate panels below each kinetic trace.

Table S11. Lifetime components with statistical standard deviations obtained from the global fits with the model described in the main text.

1 (Ni^{II})	Assignment
0.372 (±5·10^{-3}) ps	solvation dynamics
1.08 (±0.01) ps	^{1}Ni^{II}* → MC/CT
2.50 (±0.03) ps	MC/CT → MC
14.2 (±0.4) ps	spectral narrowing, e.g., vibrational relaxation
80.8 (±0.4) ps	combined MC → GS and MC → MC/CT
772 (±5) ps	MC/CT → Ground State (GS)

2 (Zn^{II})	
2.08 (±0.06) ps	solvation dynamics
62 (±1) ps	geometric relaxation
1.1 ns*	SE loss / ^{1}Zn^{II}* → ^{3}Zn^{II}
580 (±7) ns	relaxation within ^{3}Zn^{II} manifold
1.13 (±0.03) µs	decay of ligand-centered ^{3}Zn^{II} state
5.04 (±0.06) µs	ligand dissociation (tentative)
140 (±0.5) µs	ligand re-association (tentative)

* Time constant determined from fluorescence decay. The same constant as determined from the fs-ps TA measurements is 770 ps with a large error, since this is close to the full scanning range. For the ns-µs experiment a value of 1.5 ns is obtained, shorter than the 2.7 ns excitation pulse.

References

1. E. Müller, G. Bernardinelli and A. von Zelewsky, *Inorg. Chem.*, 1988, **27**, 4645-4651.
2. U. Megerle, R. Lechner, B. König and E. Riedle, *Photochem. Photobiol. Sci.*, 2010, **9**, 1400-1406.
3. H. Volfova, Q. Hu and E. Riedle, *EPA Newsletter*, 2019, 51-69.
4. *APEX suite of crystallographic software, APEX3*, Version 2015-5.2; Bruker AXS Inc.: Madison, Wisconsin, USA 2015.
5. *SAINT*, Version 8.34A; Bruker, AXS Inc.: Madison, Wisconsin, USA 2014.
6. *SADABS*, Version 2014/5; Bruker AXS, Inc.: Madison, Wisconsin, USA 2014.
7. G. M. Sheldrick, *Acta Crystallogr., Sect. A: Found. Adv.*, 2015, **71**, 3-8.
8. G. M. Sheldrick, *Acta Crystallogr., Sect. C: Struct. Chem.*, 2015, **71**, 3-8.
9. C. B. Hübschle, G. M. Sheldrick and B. Dittrich, *J. Appl. Crystallogr.*, 2011, **44**, 1281-1284.
10. in *International Tables for Crystallography, Vol. C*, ed. A. J. Wilson, Kluwer Academic Publishers, Dordrecht, The Netherlands, 1992, pp. Tables 6.1.1.4 (pp. 500-502); 504.502.506.508 (pp. 219-222); 504.502.504.502 (pp. 193-199).
11. A. L. Spek, *Acta Crystallogr., Sect. D: Biol. Crystallogr.*, 2009, **65**, 148-155.
12. C. F. Macrae, I. J. Bruno, J. A. Chisholm, P. R. Edgington, P. McCabe, E. Pidcock, L. Rodriguez-Monge, R. Taylor, J. van de Streek and P. A. Wood, *J. Appl. Crystallogr.*, 2008, **41**, 466-470.
13. Z.-C. Yang, M. Wang, A. M. Yong, S. Y. Wong, X.-H. Zhang, H. Tan, A. Y. Chang, X. Li and J. Wange, *Chem. Commun.*, 2011, **47**, 11615-11617.
14. J. Michl, E. W. Thulstrup and J. H. Eggers, *J. Phys. Chem.*, 1970, **74**, 3868-3878.
15. J. Michl, E. W. Thulstrup and J. H. Eggers, *J. Phys. Chem.*, 1970, **74**, 3878-3884.
16. J. Michl and E. W. Thulstrup, *Acc. Chem. Res.*, 1987, **20**, 192-199.
17. E. V. Puttock, P. Banerjee, M. Kaspar, L. Drennen, D. S. Yufit, E. Bill, S. Sproules and C. R. Hess, *Inorg. Chem.*, 2015, **54**, 5864-5873.
18. P. Irmler and R. F. Winter, *Dalton Trans.*, 2016, **45**, 10420-10434.
19. U. Megerle, I. Pugliesi, C. Schriever, C. F. Sailer and E. Riedle, *Appl. Phys. B*, 2009, **96**, 215-231.
20. E. Riedle, M. Bradler, M. Wenninger, C. F. Sailer and I. Pugliesi, *Faraday Discuss.*, 2013, **163**, 139-158.
21. T. Wilhelm, J. Piel and E. Riedle, *Opt. Lett.*, 1997, **22**, 1494-1496.
22. E. Riedle, M. Beutter, S. Lochbrunner, J. Piel, S. Schenkl, S. Spörlein and W. Zinth, *Appl. Phys. B*, 2000, **71**, 457-465.
23. I. H. M. van Stokkum, D. S. Larsen and R. van Grondelle, *BBA Bioenergetics*, 2004, **1657**, 82-104.
24. R.-J. Kutta, T. Langenbacher, U. Kensy and B. Dick, *Appl. Phys. B*, 2013, **111**, 203-216.
25. A. D. Becke, *J. Chem. Phys.*, 1993, **98**, 5648-5652.
26. C. Lee, W. Yang and R. G. Parr, *Phys. Rev. B*, 1988, **37**, 785-789.
27. S. Grimme, J. Antony, S. Ehrlich and H. Krieg, *J. Chem. Phys.*, 2010, **132**, 154104.
28. J. Schirmer, *Phys. Rev. A*, 1982, **26**, 2395-2416.
29. C. Hättig, *Adv. Quant. Chem.*, 2005, **50**, 37-60.
30. A. B. Trofomov and J. Schirmer, *J. Phys. B: At. Mol. Opt. Phys.*, 1995, **28**, 2299-2324.
31. T. Yanay, D. P. Tew and N. C. Handy, *Chem. Phys. Lett.*, 2004, **393**, 51-57.

32. R. Ahlrichs, M. Bär, H. M., H. Horn and C. Kölmel, *Chem. Phys. Lett.*, 1989, **162**, 165-169.
33. Y. Shao and e. al., *Mol. Phys.*, 2015, **113**, 184-215.
34. W. Humphrey, A. Dalke and K. Schulten, *J. Mol. Graph.*, 1996, **14**, 33-38.
35. F. Neese, The ORCA program system. *WIREs Comput. Mol. Sci.*, 2012, **2**, 73-78.
36. F. Neese, Software update: the ORCA program system, version 4.0., *WIREs Comput. Mol. Sci.*, 2017, **8**, e1327.
37. J. A. Johnson, J. Luo, X. Zhang, Y.-S. Chen, M. D. Morton, E. Echevería, F. E. Torres and J. Zhang, *ACS Catal.*, 2015, **5**, 5283-5291.
38. M. Grübel, I. Bosque, P. J. Altmann, T. Bach and C. R. Hess, *Chem. Sci.*, 2018, **9**, 3313-3317.
39. A. G. Condie, J. C. González-Gómez and C. R. Stephenson, *J. Am. Chem. Soc.*, 2010, **132**, 1464-1465.